Impact and Departure Dynamics of Droplets and Bubbles

Hyunggon Park

Dissertation submitted to the Faculty of the
Virginia Polytechnic Institute and State University
in partial fulfillment of the requirements for the degree of

Doctor of Philosophy
in
Engineering Mechanics

Jonathan B. Boreyko, Co-chair
David G. Schmale III, Co-chair
Sunghwan Jung
Jake J. Socha
Saad A. Ragab

May 11, 2022
Blacksburg, Virginia

Keywords: droplets, bubbles, impact, departure

Impact and Departure Dynamics of Droplets and Bubbles

Hyunggon Park

(ABSTRACT)

Droplets and bubbles are important for understanding natural phenomena such as falling raindrops, airborne disease transmission, and plant respiration systems, and also for engineering contexts such as semiconductor fabrication, nuclear power plants, and electronics cooling. However, still, more understanding is needed of these complex dynamics problems. This dissertation will talk about the droplet impact and bubble departure dynamics that are happening on various surfaces.

In Chapter 2 and 3, we will explore how the raindrops can transmit the plant pathogens. When the raindrop impacts the infected wheat leaf, the micron-sized dry spore can liberate from the surface in two different ways: dry dispersal and wet dispersal. The dry spore can liberate from the surface by the inertia of the drop, after that, the air vortex generated by the drop impact can carry the dry spores above the laminar boundary layer, with the potential for long-distance transport. For the wet dispersal, spore-laden droplets can be generated after raindrop impact, but how these spore-laden droplets can make neighboring plant diseases is still a mystery. We have shown that the splashed droplets can stick to the adjacent healthy leaf depending on the inertia of the impacting droplet, anisotropic leaf orientation, and whether it is treated with fungicide or not.

In Chapter 4, We design a micropillar aluminum substrate that preferentially grows frost on top of the pillars. When deposited droplets impact the frost-tipped pillars, the dynamic pressure causes the water to wick within the frost faster than it can impale the gaps between the pillars. Upon freezing, this safely suspends the resulting ice sheet in the air-trapping Cassie state, without any surface coatings required.

For the last part (Chapter 5), we investigated the bubble coalescence dynamics that can depart the bubble with a micrometer size. We made the micro-structured

surfaces tailored to nucleation sites to enable the coalescence-induced departure of micro-bubbles. A scaling model reveals two different modes of bubble departure following the coalescence-induced depinning: capillary-inertial jumping for micrometric bubbles and a buoyant-inertial departure for millimetric ones. Eventually, this small bubble departure can delay film boiling which can be the barrier to the boiling heat transfer.

Impact and Departure Dynamics of Droplets and Bubbles

Hyunggon Park

(GENERAL AUDIENCE ABSTRACT)

Dynamic interaction of droplets and bubbles with different surfaces is ubiquitous: an impacting rain droplet on a plant leaf is responsible for transmitting thousands of plant pathogens, or decreasing the departure size of bubbles on the surface of heat exchangers would increase their efficiency. It is now well-understood that the departure of condensed droplets on water repellent surfaces exhibits superior heat transfer compared to all other modes of condensation and also enables self-cleaning, delayed frosting, and anti-fogging surface technology.

In Chapters 2 and 3, we are studying the dynamic interaction of raindrops and wheat leaves. By depositing water droplets on diseased leaves, we found out a raindrop can transmit wheat pathogens. This simple but important phenomenon would adversely affect the quality of our wheat which is the most widely grown crop in the world, contributing to a large amount of portion the global food supply.

Chapter 4 sheds light on another example of the dynamic interaction of raindrops and an icy surface. We designed a pillared aluminum substrate that preferentially grows condensation frosting on top of the pillars. With this passive anti-frosting technology, we are able to trap water droplets and ice in the suspending water droplets in the air-trapping Cassie state without using a fragile nanotextured structure or a complex re-entrant structure. Upon freezing, this safely suspends the resulting ice sheet in the air-trapping Cassie state, without any surface coatings required. Under a cold and humid environment, Cassie water freezes into Cassie ice which is advantageous for its low surface adhesion.

In Chapter 5, we show that rationally micro-structured surfaces tailor nucleation sites to enable the coalescence-induced departure of micro-bubbles. With this technique, we are able to remove surface bubbles at smaller sizes that would result in enhancing the critical heat flux of nucleate boiling. We have used a blend of ex-

periments and scaling to understand the underlying physics of this phase-change problem.

Dedicated to my dear family ...

Acknowledgements

I would like to express my gratitude to my great advisor Prof. Jonathan Boreyko. Thanks Jonathan for accepting me to join NIFI. Indeed, I learned a lot from you, not including the beauty of scaling analysis and how to write scientifically but also how to be optimistic when we are dealing with our messy lives; you are the most positive-minded person that I have ever seen! You have definitely changed the way that I perceive my life. Thank you for all of your support during my Ph.D. while you have a busy life as a professor or a father of five children. Thanks for suggesting to me interesting books and music as well. I miss you a lot and will be in touch forever.

I would like to also thank other committee members: Prof. David Schmale, Sungwhan (Sunny) Jung, Saad Ragab, and Jake Socha. Prof. Schmale, I still remember the day when we first met; it was during my first visit to VT in 2017 and I talked to you. Thanks for assigning me to a very beautiful wheat spore project. I really enjoyed your group's meetings at the Latham Hall which broadened my research scope. I am also grateful to Prof. Sungwhan Jung, who introduced me to this amazing interfacial fluid mechanics world. Thanks to you, I have fallen in love with the beautiful research topic that kept me motivated. I have learned a lot while I was working at your lab which subsequently made me a 'camera man' at the NIFI lab. Special thanks go to Prof. Ragab for the knowledge that he taught during

his fluid class. Your class paved the path for my knowledge of fluid mechanics. Finally, I want to thank Prof. Socha who taught me a very important lesson about communications skills, The way I present my research has changed after your class.

NIFI lab is the most valuable thing that I experienced at Virginia Tech. I have enjoyed every single second of working with my very diverse lab mates. With the help of my lab mates, I was able to settle down and adjust to the lab. Farzad, you are one of the best lab mates that I have ever met! You are an amazing researcher; I have learned a lot from you since day one when I asked you about the intermediate dynamic class. Also thanks for supporting me, and your suggestions are always great! Ranit, I had a lot of fun with you chatting about research and life in general. I got to know a lot of different cultures due to you. Weiwei, you have been calling me "Oppa" and know much more about k-pop than I do. I've enjoyed the time spent with you in the NIFI lab. Pranav, we joined the same year and I can still remember the time we meet at the visiting weekend. I appreciate your helping me to settle down in this lab. Kevin, the discussion with you was always productive. Viverjta, we joined the NIFI lab in the same year and I still miss the time we worked together at the lab. Nick, we didn't get to hang out as much but you are a nice guy. Yash, I will miss the walks we took for emotional support. Ndidi, thanks for being nice to me all the time, I will miss being called "Sunbae". Thanks to all undergraduate students and various people that I meet during my graduate study.

Thanks, as well, to my previous lab members before joining Virginia Tech, who helped start my graduate career, Prof. Mitul Luhar, and Fluid-Structure Interactions Lab members Christoph, Mark, Andrew Shilpa, and Chanye. I could not have even started this journey without their help.

Finally, my Ph.D. work would not have been completed without the help of my family. Thanks to my parents and my brother for all their unconditional support and trust. They trusted me all along this long journey.

Contents

List of Figures

List of Tables

1

Introduction

1.1 Background information and motivation

The dynamic interaction of droplets and bubbles with different surfaces has attracted researchers' attention for decades as it results in physical phenomena including splashing, impact, wicking, and coalescence. The beauty of this interaction was illustrated about 30 years ago when high-speed cameras were invented. The resulting interaction of droplets with solid surfaces includes deposit, bounce, and splash. Coalescence and jumping of vapor bubbles is another example of the interaction that we see when we are making tea or coffee. Many studies regarding drop impacting on the solid surfaces have been studied for various applications such as plant pathogen science [6–8], crime scene application [9], rapid spray cooling of hot surfaces [10, 11], and even inkjet printing application [12]. To date, suspending water droplets in the air-trapping Cassie state has always required using a structured surface that is superhydrophobic. For a chilled superhydrophobic surface, this water can freeze into Cassie ice which is advantageous for its low surface adhesion. Although the jumping droplet condensation has been widely understudied, during the past 15 years, the jumping of vapor bubbles on surfaces is still a mystery. As

seen in the various examples above, droplets and bubble are ubiquitous, and understanding the dynamics of the droplets and bubbles are really important. Here, we are highlighting different physical phenomenon: bouncing droplets and bubbles, wicking, bubble nucleation, and coalescence of bubbles.

1.1.1 Bouncing droplets and bubbles

When the droplets and bubbles are interacting with the surfaces, there are two chance of scenarios. The first one is sticking on the surface and the other scenario is departing from the surface. The driving force is needed to overcome the adhesion force of the droplets and bubbles on the surface. The orthogonal energy which is required to overcome the adhesion energy of droplets and bubbles on the surface is called work of adhesion [22–24],

$$E_{\mathrm{ad}} = \gamma_{\mathrm{liquid}} S_{\mathrm{contract}} (1 - \cos\theta_{\mathrm{liquid}}) \tag{1.1}$$

where γ_{liquid} is the surface tension of the liquid, S_{contract} is the contact area of the liquid and the surface, and θ_{liquid} is the contact angle of the liquid.

Or, the lateral energy which is required to overcome the pinning force of the liquids (bubbles and droplets) is called the pinning energy [22],

$$E_{\mathrm{p}} \approx \pi R^2 \gamma (\cos\theta_{\mathrm{R}} - \cos\theta_{\mathrm{A}}). \tag{1.2}$$

where R is radius of the droplets and bubble contact with the surface, γ is the surface tension of the liquid, and θ_{R} and θ_{R} is the advancing and receding contact angle of liquid.

Both energies are needed to overcome the adhesion of the liquid and solid surface and the investigation of the interaction between the liquid (droplets and bubbles) and various solid surfaces is still a mystery.

1.1.2 Wicking

For the general porous structures, when the liquid is touching the structures, it is trying to with inside the structure with the capillarity. The liquid's capillary motion can be analyzed as the competition between the surface tension of the liquid and the viscous dissipation of the liquid inside the porous structures. This relation is generally represented

$$L(t) = \sqrt{\frac{\gamma R_{\text{eff}} \cos\theta}{2\eta}} t^{1/2}, \tag{1.3}$$

where L is the displacement of the liquid front over time, γ is the surface tension of liquid and and η is viscosity of the liquid, R_{eff} is the effective pore radius of frost, and θ is the intrinsic contact angle the liquid with the surface. But if the the solid surface is frost which has the porous structure inside and touched with the liquid, it showed the different phenomenon which is called ice wicking [25].

1.1.3 Bubble nucleation and drop coalescence.

The nucleation, growth, and departure of vapor bubbles is studied for boiling. When the surface is heated up in liquid bath, the vapor bubbles start to nucleate from the surface and grow until the buoyancy can over come the surface tension of the the bubble [13]. Understanding this bubble nucleation in boiling is really important for various industrial applications, such as steam power plant [14], electronics cooling [15–17], HVAC system [18] and water desalination output [19, 20].

For droplets on nonwetting surfaces, the merged droplet can jump from the surface upon coalescence [2]. This interesting propulsion is caused by excessive surface energy released upon coalescence events.

$$\gamma R^2 \sim \frac{1}{2}\rho R^3 v^2$$
$$v \sim \sqrt{\frac{\gamma}{\rho R}}. \tag{1.4}$$

The follow up study has shown that the jumping droplet condensation on superhydrophobic nanostructured surfaces can increase heat transfer rate up to 30 % with the jumping droplet condensation [3]. However, although the jumping droplet condensation has been widely understudied, during the past 15 years, jumping vapor bubbles on surfaces is still a mystery.

The purpose of this dissertation is to understand the underlying physics of impact and departure dynamics of drops and bubbles. The first part of this dissertation (Chapter 2 and 3) is focused on the drop impact on the natural wheat leaf surface. More specifically, we investigated how impacting raindrops can transmit the disease. From the second part of the dissertation (Chapter 4 and 5), we will talk about the interfacial fluid dynamics of drops and bubbles on engineered surfaces for some potential industrial applications. Specifically, we tried four different topics of dynamics of drops and bubbles here which are not under-explored so far. Each topic is experimentally observed and theoretically examined to verify the experimental result. Here, we are briefly explaining different chapters of this dissertation.

1.1.4 Vortex-induced dispersal of a plant pathogen by raindrop impact

Understanding the disease transmission in plant pathology is one of the most important parts of animal and plant health. Rainfall is one of the main causes of the spreading of pathogen spores. However, previous work just focused on the splashed droplet (wet state dispersal) after rain drop impact and this gives a limited understanding of the dispersal of spores. In Chapter 2, we demonstrated the spreading of dry spores from diseased wheat leaf surfaces after rain splashing. High-speed images

can capture the liberation of dry spores which is following the single drop impact on the diseased leaf surface. We showed the air vortex that is generated after raindrop impact can carry the dry spores out of the laminar boundary layer and give more potential to long-distance transport of pathogen dispersal through the atmosphere.

1.1.5 Dynamics of splashed droplets impacting wheat leaves treated with a fungicide

Rain is one of the main causes of the dispersal of many plant pathogens. Fluid mechanics for the spreading of plant-pathogen during rainfall is still understudied. Previous studies have only focused on how pathogens (Puccinia triticina) are liberated from the leaf surface in dry state. However, in Chapter 3, we show that splashed droplets either bounce or stick, depending on the orientation of the leaf and whether the surface of the leaf has been treated with a fungicide. A scaling model revealed that bouncing was enabled when the droplet's kinetic energy exceeded its pinning energy to the surface. Our findngs indicate that, ironically, the application of fungicide to protect a wheat plant may also facilitate pathogen spread and infection by making leaves sticky to spore-laden droplets.

1.1.6 Using frost to promote Cassie ice on hydrophilic pillars

The accretion of ice and frost on various infrastructures causes mechanical damage, losses in energy efficiency. It is obvious that preventing ice and frost from forming in the first place is even better than reducing a surface's ice adhesion strength. For this reason, the past decade has seen a flurry of efforts to leverage micro/nanostructured superhydrophobic surfaces to achieve anti-icing, also commonly known as icephobicity. The suspended Cassie state of supercooled water on a superhydrophobic surface enables cooperative anti-icing mechanisms: a delay in heterogeneous ice nucleation [26,27] and greatly enhanced droplet mobility [22], such that droplets can slide [28], bounce [26, 29], or jump [2, 30] from the surface before freezing can oc-

cur. Another emerging idea is to pattern or impregnate a surface with a hygroscopic (low saturation pressure) material [31, 32]. For example, depositing salts or glycols onto a surface can keep the intermediate surface areas dry, as all nearby moisture is attracted to these diffusive "magnets." However, these hygroscopic materials become diluted with water very quickly (typically within minutes), upon which time the dry zones collapse [33–36]. In Chapter 4, we showed the new concept which is the first-ever to trap water droplets and ice in the Cassie state on an uncoated and uniformly hydrophilic surface structure. We design a pillared aluminum substrate that preferentially grows frost on top of the pillars. When deposited droplets impact the frost-tipped pillars, the dynamic pressure causes the water to wick within the porous frost faster than it can impale the gaps between the pillars. Upon freezing, this safely suspends the resulting ice sheet in the air-trapping Cassie state, without any surface coatings required.

1.1.7 Coalescence-induced jumping bubbles during pool boiling

Phase-change heat transfer, in particular nucleating boiling, is becoming increasingly important for applications such as quenching metal alloys and electronics cooling. Surfaces with micro/nano-structures have shown a significant enhancement of the critical heat flux by enhancing the wickability of the liquid phase to delay film boiling. However, an alternative strategy, of removing surface bubbles at smaller sizes, has been largely ignored.

In Chapter 5, we engineer micro-structures onto a quasi-one-dimensional metallic substrate (1 mm wide and 10 cm long), where the micro-structures promote the controlled nucleation and early coalescence of bubbles and the 1D form factor facilitates clear side-view high-speed imaging of the bubble dynamics. When the substrate is submerged in water and heated, coalescing vapor bubbles detach from the substrate at sizes in an order of magnitude smaller than usual ($100\,\mu$m rather than

1 mm). A scaling model reveals two different modes of coalescence-induced departure: capillary-inertial jumping at smaller sizes and a buoyant-inertial departure at larger sizes.

1.2 Practical applications

Understanding the dry spore dispersal with the help of vortex caused by raindrop impact can elucidate the underlying mechanism of long distance disease transmission. Also, investigation of wet spore dispersal gives us the better understanding how the rain drop can spread disease after splashing. In other words, understanding both dry and wet dispersal can potentially increase wheat production and give the direction of how to use fungicide properly. With the effect of wicking, the impacting droplet on frost tipped pillar can make Cassie ice which can potentially reduce the ice adhesion without requiring any nano structures and surface chemical coating. Also, understanding the bubble dynamics during pool boiling can delay the film boiling which is the thermal barrier of heat transfer and eventually increase heat transfer efficiency in various industrial applications.

2

Vortex-induced dispersal of a plant pathogen by raindrop impact

The content of this chapter was previously published as journal manuscripts in [37], and reproduced here with minor modifications. In this chapter, experimentally and theoretically, we are trying to understand how dry spore can transmit disease after raindrop impact.

2.1 Introduction

Plant disease spreading threatens our food safety and security [38, 39]. Some plant pathogens can be widely spread by rainfall [7, 40], in which splashing droplets can carry pathogenic spores within and among susceptible host plants [7]. Small splashing droplets with a diameter of $< 100\,\mu$m can be carried via wind currents [41, 42]. However, most satellite droplets from drop impacts are larger than 100 μm [7], which are too heavy to follow wind flows over long distances; typically less than a few tens of centimeters [40, 43].

Previous studies showed that dry plant pathogens such as rusts can be trans-

ported kilometer distances in the atmosphere [44] and even cross continents [45–48]. In 1963, Hirst and Stedman [44] showed an increase in the concentration of dry rust spores in the atmosphere followed by raindrop impacts. Other bioaerosols have been observed to increase shortly after rainfall [49] and then stay up in the air for several hours [50]. Once airborne, these small dry spores can avoid the scavenging of raindrops by following air streamlines around the falling raindrops, while large particles are scavenged by raindrops [51,52]. Such light dry spores are a major entity of long-distance pathogen spreading. However, the liberation mechanism of dry spores from an infected plant is not well understood.

In this present work, we observed the liberation of dry spores following simulated raindrop impacts on wheat leaves infected with the rust fungus, *Puccinia triticina*. In addition, glass particles similar to the rust spores in size were used for a parametric study and to visualize dry spreading mechanisms at a greater level of detail. We describe and explain how an air vortex is formed after a drop impacts the leaf surface and carries dry spores away from the plant surface. Consequently, dry spores dispersed by the air vortex induced by drop impact have the potential to traverse the laminar boundary layer and travel over longer distances [53]. The mechanism of the air-vortex dispersal could explain abrupt increases in dry spores in the atmosphere immediately after rainfall events and also long-range disease spreading.

2.2 Results

2.2.1 Types of spore dispersal

We observed and analyzed the dispersal motion of urediniospores of *P. triticina* when a raindrop hits an infected leaf containing uredinia (figure. 2.1(a)). Figure 2.1(b) shows that a falling drop is powerful enough to liberate spores. Here, we identified two types of spore dispersal. The first is a wet splash dispersal of spores that has been studied previously. When a droplet impacts a surface, the contact

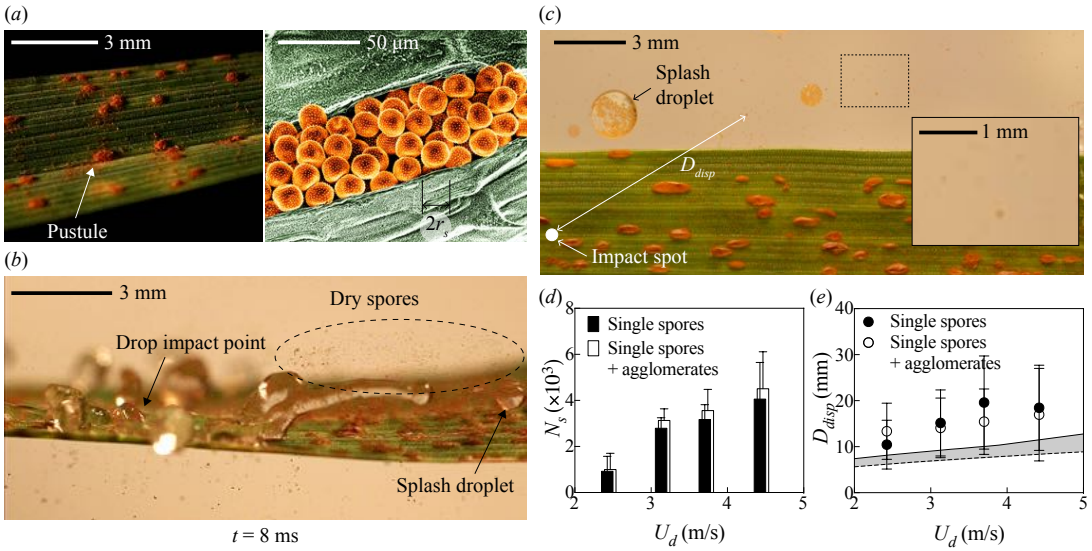

FIGURE 2.1: (a) Rust-infected wheat leaf surface on the left panel and scanning electron microscopy (SEM) image of a uredinium (rust pustule containing urediniospores) on the right panel. Here, the pustule of spores is seen on the epidermis of the wheat leaf. (b) Dispersal of thousands of dry spores by drop impact when $[R_d, U_d]$=[1.6 mm, 2.4 m/s], where R_d, U_d are the radius and velocity of the impacting drop, respectively. (c) Visualization of dispersal patterns at $[R_d, U_d]$=[1.8 mm, 2.8 m/s], where the inset shows dry spores discharged by drop impact. (d) The number N_s and (e) dispersal distance D_{disp} of dry spores versus impact velocity U_d for a drop of 1.8 mm in radius. The gray area in (e) corresponds to the calculated distance of dispersed spores without an air vortex. The filled bars and circles are for single spores only, whereas the open bars and circles are for all spores including spore agglomerates (more than one spore).

line of the spreading edge of the drop becomes unstable and forms several daughter splash droplets due to the high inertia of the drop and the hydrophobic property of a leaf substrate [54]. As shown on the right side of figure. 2.1(b), splashing droplets fly out along with spores inside. Spores inside a splash droplet are shown in figure. 2.1(c) and Supplementary Information Appendix A. Although the number of spores inside a splash droplet is more than that of dry-dispersed spores [40], the splash droplets are too heavy to follow the surrounding air current, limiting the range of dispersal.

The second is a dry spore-dispersal, i.e. not wetted by a raindrop. The dry-spore

dispersal is attributed to either the vibration of a wheat leaf (see figure. 2.1(b)) or the direct impact of the drop (see the zoomed inset of figure. 2.1(c)). Most spores are liberated from the upper surface, especially due to drop impact (the right-top side of figure. 2.1(b)). On the other hand, spores on the lower surface can be thrown by a rapidly decelerating leaf, but the number of ejected spores from the lower surface is less than that from the upper surface.

2.2.2 Measurement of the number of ejected spores

We measured the number of dispersed dry spores, N_s, after a drop impact. We first attached a rust-infected wheat leaf on a petri dish. Then, a drop was released onto the wheat leaf at different heights to vary the impact speed. Hence, we measured the number of dry-dispersed spores using a Nikon D500 camera with a pixel resolution of 6016×4000; the area of most spores was measured to be about 5 pixel^2 (see Appendix A in detail). Figure 2.1(c) show not only wet dispersed spores, but also thousands of dry spores. Figure 2.1(d) shows that the number of dispersed dry spores, N_s, is on the order of 10^3 and increases with the impact velocity, U_d. Such an increase of N_s with respect to U_d can be attributed to not only higher impulse-momentum [40], but also to an increase in the drop-contact area as the drop spreads [55].

2.2.3 Ejection mechanism

Spores are detached by the spreading motion of a drop as it exerts dynamic force on the spores. The dynamic force to drag and scavenge spores, $C_D \rho_d U_c^2 r_s^2$ ($\sim$ 10 nN), exceeds the interparticle force of *P. Triticina* spores, 0.7 nN (see Appendix B). Here, C_D, ρ_d, U_c, and r_s are the drag coefficient, the liquid density, the speed of the liquid contact line (on the order of 1 m/s), the radius of a spore (≈ 10 μm). The detached spores stay on the advancing meniscus, and then collide with dry spores on the way. By assuming elastic collision between spores on the meniscus and dry spores, the

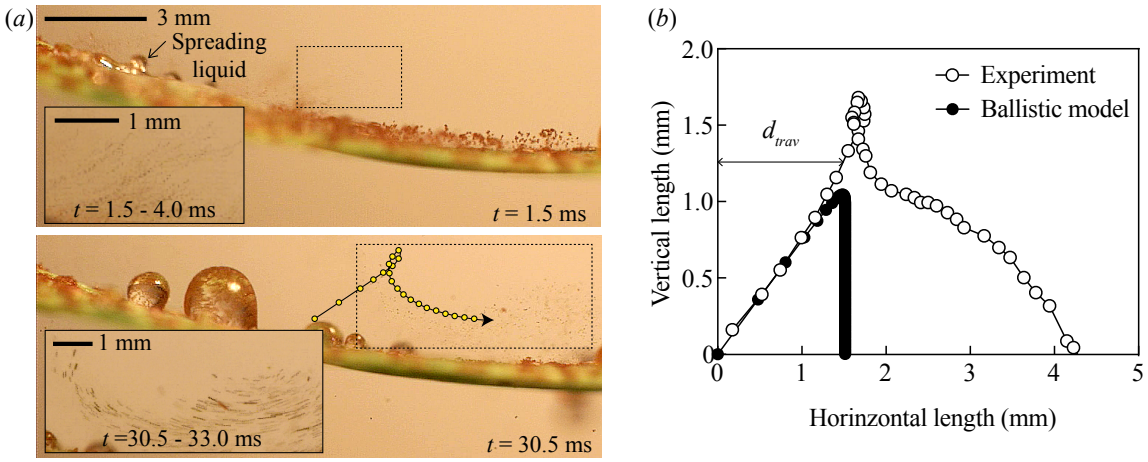

FIGURE 2.2: (a) Visualization of spores of *P. triticina* motions moving around a wheat leaf when a raindrop of $[R_d, U_d]$=[1.6 mm, 2.4 m/s] impacts the leaf surface. Dry wheat spores escape from the leaf, showing swirling trajectories during their dispersal (a solid curve with circles is obtained by tracing one spore). Each inset shows overlapping multiple images to visualize the trajectories of dry-spore dispersal (see Movies S1 and S2). (b) Comparison of spore trajectories obtained from an experiment and from a ballistic model.

ejection velocity of dry spores, V_e, would be proportional to the impact velocity of a falling drop, U_d. A detailed theoretical model and experimental validation of spore ejection are presented in Appendix A.

2.2.4 Spore-traveling distance and trajectory

For spores moving through quiescent air, the Reynolds number, $Re_s = \rho_a V_s(2r_s)/\mu_a \lesssim 1$, is small, where ρ_a and μ_a are the density and dynamic viscosity of air ($\rho_a = 1.2$ kg/m^3, $\mu_a = 1.82 \times 10^{-5}$ Pa·s) and V_s is the instantaneous speed of a spore. Here, the instantaneous speed decreases over time due to the air drag after reaching its maximum speed at the moment of ejection ($V_e \sim 1$ m/s). Thus, the trajectory of spores can be predicted by balancing inertial force $\rho_s(4/3)\pi r_s^3(d\vec{V}_s/dt)$, Stokes drag $6\pi\mu_a\vec{V}_s r_s$, and gravity, where ρ_s is the spore density. By integrating these forces with the initial condition as $V_s(t = 0) = V_e$, a spore-travel distance d_{trav} can be written

as the following;

$$d_{\text{trav}} = \frac{2\rho_s r_s^2 V_e \cos\alpha_e}{9\mu_a}\left[1 - e^{-9\mu_a t_r/(2\rho_s r_s^2)}\right], \tag{2.1}$$

where α_e and t_r correspond to the ejection angle and residence time of a spore in air, respectively. For ejected spores with $V_e = 1$ m/s, the relaxation timescale, $\tau_s = (2/9)\rho_s r_s^2/\mu_a$, is about 10^{-3} s, whereas the residence timescale, t_r, becomes only 10^{-2} s. Therefore, the travel distance, d_{trav}, is close to $V_e\tau_s\cos\alpha_e$ since the exponential term, e^{-t_r/τ_s}, in equation (2.1) is quite small on the order of 10^{-5}.

Figure 2.1(c) shows horizontal distances of dispersed spores measured from the drop-impact point, D_{disp}. To avoid any confusion, it is worth mentioning that the travel distance, d_{trav} is measured from spore's resting position not from the drop-impact point. Hence, d_{trav} is always smaller than D_{disp}. Interestingly, we found that the dispersal distance of spores exceeds theoretical values from the above force balance. Figure 2.1(e) shows the consistent discrepancy over different drop speeds.

To rectify the discrepancy on dispersal distance, we visualized the side-view trajectory of rust spores as in figure 2.2(a). Figure 2.2(a) shows that spores ballistically move shortly after the ejection (see the inset in the upper panel) and then swirl around (see the inset in the lower panel). The overall trajectory of one spore is shown as the black line in the lower panel too. Figure 2.2(b) illustrates a detailed trajectory from an experiment and a simulated trajectory using the ballistic model above. The ballistic model shows a right-triangle path (closed symbols) known as the Tartaglia's trajectory [56], whereas the experimental trajectory presents a swirling motion with a longer travel distance (open symbols). In addition, the maximum height reached by the spore is a bit higher than the predicted height from the ballistic model. In order to explain this discrepancy, we need to understand an air flow around liberated spores upon drop impact.

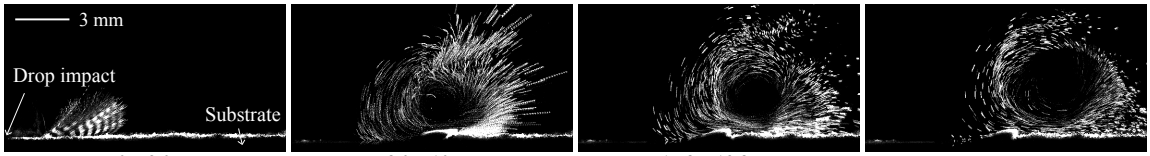

FIGURE 2.3: Visualization of the dispersal motion of glass beads (surrogates for spores) when $[R_d, U_d]$=[1.9 mm, 3.1 m/s]. Ballistic motion of the beads was observed only at the beginning stage of dispersal, but later spores exhibited a swirling motion (see Movies S3 and S4)

.

2.2.5 Trajectory comparison using artificial spores

To visualize the air flow, we used glass beads as surrogates for spores (glass sphere type-I in table 2.1 in Materials and Methods). The density and radius of particles are close to those of actual wheat spores. We observed similar dispersal behaviors of actual wheat spores. In the very beginning, ballistic trajectories were observed as shown in the first panel of figure. 2.3. Then, the glass beads were swirling around and slowly move to the right (the 2nd, 3rd, and 4th panels of figure. 2.3). Since the glass beads are light, this swirling motion can represent the pathlines of air current. To confirm this, we calculated the Stokes number St, defined as a ratio of the relaxation time of a particle τ_s $(= 2/9\rho_s r_s^2/\mu_a)$ to the characteristic flow time τ_f $(= \bar{r}_w/\bar{U}_w)$. Here $\bar{r}_w \sim 1$ mm and $\bar{U}_w \sim 0.1$ m/s are the mean radius and velocity of the swirling flows. The Stokes number is very small for artificial spore I ($St = 0.001 - 0.13$). Also, for the wheat spore, St is also 0.15, which indicates that such swirling motion is induced by surrounding air flows.

2.2.6 Effect of surrounding air flows

Bischorberger et al. [57] showed the experimental evidence of a vortex ring created by a spreading drop. Here, we also visualized the vortex ring using a smoke generator (ChauvetDJ H700), as shown in figure 2.4(a). Figure 2.4(b) shows the schematic of forming the air vortex via a spreading drop. The air flow was induced by the

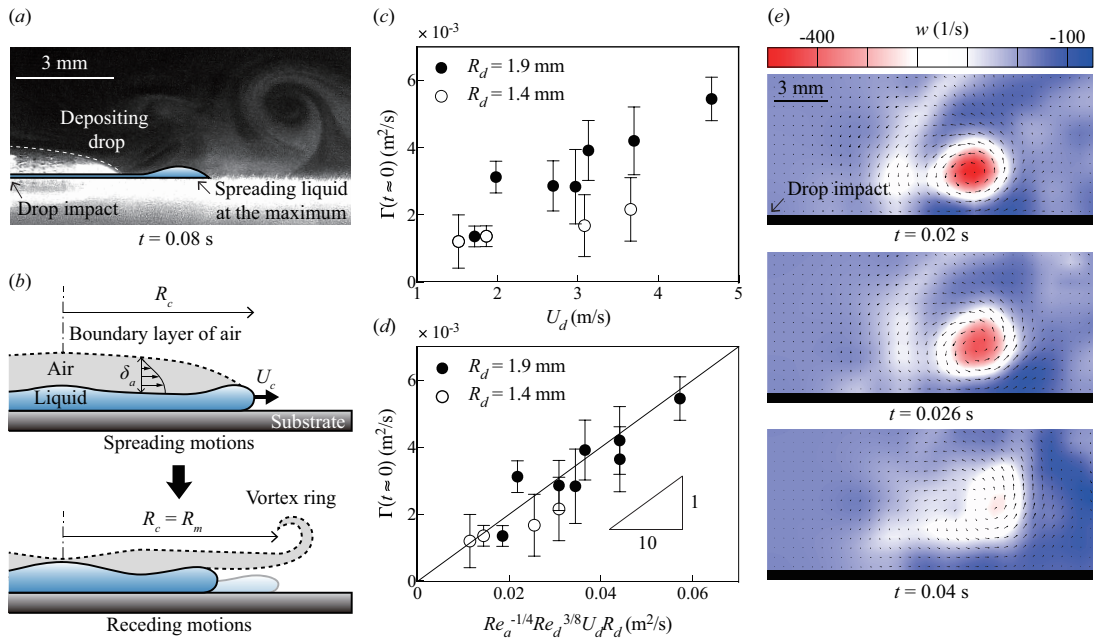

FIGURE 2.4: (a) Smoke visualization of the air vortex with [R_d, U_d]=[1.4 mm, 3.3 m/s]. The white dashed-curve represents the final shape of a drop and the solid curve indicates the intermediate shape of a spreading drop at the maximum spreading radius. (b) Schematic of the formation of an air vortex, driving spores swirl around. (c) Magnitude of a circulation Γ versus an impact velocity U_d depending on a drop radius R_d. (d) Γ is re-plotted according to our scaling law; Eq. (2.2). (e) Contour map of a vorticity obtained from PIV measurements using glass beads with [R_d, U_d]=[1.9 mm, 3.1 m/s], showing the dissipation of the air vortex with elapsed times.

spreading drop, whose speed was proportional to the inertia of the impacting drop. Then, a vortex ring was shed as a boundary layer keeps propagating laterally, after the spreading drop reaches its maximum radius. We experimentally measured the initial magnitude of circulation using particle tracking velocimetry (PTV) (Appendix A). Figure 2.4(c) shows that $\Gamma(t \approx 0)$ is proportional to U_d and R_d, which indicates that circulation $\Gamma(t \approx 0)$ is induced by the drop inertia. Also, we observed that the air vortex is dissipated over time and lasts only for a few tens of milliseconds, as shown in figure 2.4(e). Therefore, airborne spores are swirled up by an air vortex and then fall back under gravity after a few tens of milliseconds, which can explain complicated trajectories in figure 2.2.

2.2.7 Theoretical model of the magnitude of a circulation in air

We developed a scaling relation of $\Gamma(t \approx 0)$ for a better understanding of the vortex motion. The shear motion of a spreading drop drives an air flow and eventually creates an air vortex in the air. This spreading energy per unit length, E_D, is given as $\int_0^{t_m} \int_\Omega \phi \, d\Omega dt \approx \phi \Omega t_m$, where ϕ, Ω, and t_m are the viscous dissipation function per unit length, the effective area of a viscous fluid, and the time duration for a spreading drop to reach its maximum radius, respectively. The dissipation function ϕ scales as $\mu_a(\bar{U}_c/\delta_a)^2 \sim \mu_a \bar{U}_c^2/(R_d^2 Re_a^{-1})$ using the Blasius boundary thickness of air, δ_a, where $\bar{U}_c$ and Re_a are the mean speed of a liquid contact line and the Reynolds number of air, $\rho_a U_d(2R_d)/\mu_a$. The cross-sectional area of the boundary layer scales as $\Omega \sim R_m \delta_a$ and $t_m \sim R_d/U_d$. Also, the maximum spreading radius of an impacting drop, R_m scales as $R_d Re_d^{1/4}$ [55] where $Re_d = \rho_d U_d(2R_d)/\mu_d$ with the dynamic viscosity of a liquid, μ_d. We finally get the spreading energy as $E_D \sim \mu_a R_d U_d Re_a^{1/2} Re_d^{3/4}$ by substituting R_m & $\bar{U}_c$ as derived in SI Appendix E. The rotational energy of the air vortex, E_R, is given as $\rho_a \Gamma^2(t \approx 0) = \rho_a \bar{r}_w^2 (\bar{r}_w \bar{w})^2$ [58] where $\bar{r}_w$ and $\bar{w}$ are the mean radius and vorticity of the air vortex, respectively. By balancing spreading and rotational energies, we get the circulation as

$$\Gamma(t \approx 0) \sim Re_a^{-1/4} Re_d^{3/8} U_d R_d. \tag{2.2}$$

Our scaling relation shows the dependence of Re_a on the initial circulation, $\Gamma(t \approx 0)$. Figure 2.4(d) shows good agreement of our scaling argument with experimental data. Furthermore, this association explains experimental observations previously reported in [57].

2.2.8 Simulation of spore trajectories

We also simulated the trajectories of spores by solving the equation of motion considering inertial force, air drag force, and gravitational force;

$$\rho_s \left(\frac{4}{3}\pi r_s^3\right) \frac{d\vec{V}_s}{dt} = 6\pi\mu_a r_s(\vec{V}_s - \vec{U}_w) - \rho_s \left(\frac{4}{3}\pi r_s^3\right) \vec{g}. \tag{2.3}$$

Here, $\vec{g}$ is the gravitational acceleration and we neglect the Basset force because of low ρ_a and μ_a. To estimate the air flow, $\vec{U}_w$, we used potential theory and the method of images along with our estimated circulation. Thus, the corresponding complex potential W can be written as $W = -\mathrm{i}\Gamma/(2\pi)\log\left[(z-d)/(z+d)\right]$ [59] where z is a complex variable of a position and d is a distance from the wall. Here, the vortex circulation, Γ, dissipates over time after the vortex is shed from a spreading drop. The wall distance, d, increases over time as $d \sim \sqrt{\nu_a t}$ where ν_a is the kinematic viscosity of air while the vortex dissipates and diffuses away (see Appendix A). By differentiating W with respect to z, we can determine $\vec{U}_w$. Finally, we can numerically solve equation (A.3) with given ejection velocity and angle of spores. Figure 2.5 shows that computed trajectories from equation (A.3) follow experimental trajectories quite well.

The vortex generated from a spreading raindrop can blow spores farther away and also make the swirling motion of the spores, thus resulting in traveling higher and longer distances. Figure 2.5 also shows that the maximum height of liberated spores increases in the presence of the air vortex (red and orange circles and lines), and thus most liberated spores can escape beyond the boundary layer of a leaf ($\delta_L \approx 1.72\sqrt{\nu_a L/U} \approx 0.7 - 2.1$ mm; the length of leaf, $L \approx 10$ cm and a typical wind speed, $U = 1 - 10$ m/s) [60]. Thus, spores liberated by an air vortex may cross the laminar boundary layer and be exposed to the wind, with the potential to travel over long distances.

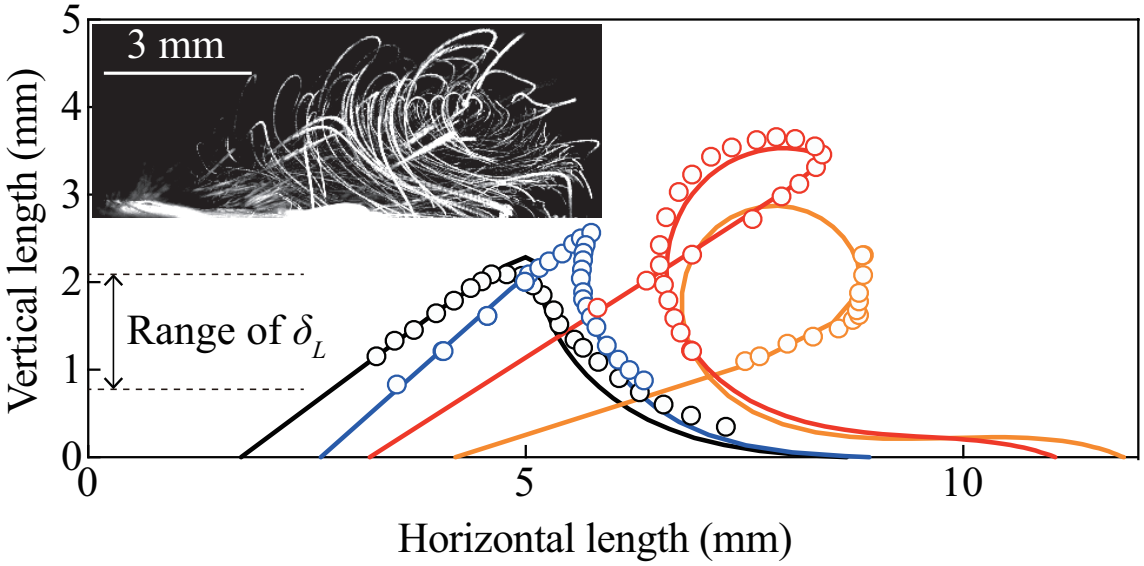

FIGURE 2.5: Experimental (circles) and theoretical footprints (solid lines) of glass beads, where $[R_d, U_d]$=[1.4 mm, 3.2 m/s]. The inset shows the actual trajectories of glass beads I, which was obtained from overlapping multiple images from $t = 0.4$ to 76 ms.

2.3 Discussion

Various spore-dispersal mechanisms have been reported previously. These include dispersal resulting from changes in temperature and relative humidity [61], in response to mechanical stimuli [62], from insect movement [63], along with dew and splash droplets [64], and due to cavitation bubbles [65]. In this article, we report a new dry-dispersal mechanism of a plant pathogen via raindrop impact. When a raindrop hits a rust-infected plant leaf, the drop initially pushes the spores to be liberated from the leaf surface. Then, the spores follow swirling trajectories aided by the air vortex ring formed by the raindrop. As a result, the spores travel longer distances and higher heights, thereby reaching outside the boundary layer to be swept by wind. Therefore, a number of pathogenic spores can escape from the region of a host plant and possibly land on other susceptible plants.

A few limitations exist to simulating the trajectory of rust spores: splash droplets

and leaf's flexibility. First, the splash droplets affect the shape and magnitude of the air vortex, which change the trajectory of spores only near the end (Appendix A). Second, a flexible leaf will vibrate due to the drop impact, which increases the number of spores. However, the response of the leaf is much longer than spreading time of the drop, which minimizes its effect on liberated spores. Nevertheless, we consistently observed that both rust spores and surrogate glass beads show the swirling trajectories (figure. 2.2) and are able to escape from the leaf boundary as d_{trav} and maximum height are larger than the width of leaf and δ_L, respectively. Our finding could be extended to crops impacted by rust diseases, such as coffee and corn, thereby making d_{trav} much longer than that without the air vortex see Appendix A).

Outside the boundary layer, air flows are turbulent. So, the Stokes number of spores in that region is much less than 1; $St_k = \tau_s/\tau_k$ where the particle relaxation timescale is $\tau_s = (2/9)\rho_s r_s^2/\mu_a \sim 10^{-3}$ s and the Kolmogorov timescale is $\tau_k = (\nu_a/\epsilon)^{1/2} = 10^{-2} - 10^{-1}$ s. The turbulent kinetic dissipation rate ϵ is expected to be $10^{-3} - 10^{-2}$ m^2/s^3 at a half height of a typical canopy [66]. Thus, many airborne spores with $St_k < 1$ can be immediately dispersed by the turbulent eddies, similar to ocean spray droplets [67]. Furthermore, plant pathogens can travel over kilometer distances via wind currents [68]. Therefore, the dry dispersal of plant pathogens via a vortex ring may be a critical component of the spread of a plant pathogen in the atmosphere over long distance.

2.3.1 Preparation of infected wheat leaves

Lines of wheat susceptible to wheat leaf rust infection were cultivated under controlled growth conditions (135 μM/m^{2}s^{-1} light for 12h/day, 35°C) for 6 weeks following seed germination. Healthy leaves were inoculated using a suspension of *Puccinia triticina* urediniospores in water with 0.001% of detergent as adjuvant. Inoculated plants were then incubated in an isothermal-isohumidity chamber at 15°C and 99%

for 24 hours, then removed back to previous controlled growth conditions. After 7 to 10 days, pustules of powdery P. triticina spores are sufficiently broken through the epidermis of wheat leaf, as illustrated in figure 2.1(a).

2.3.2 Properties of rust pustule and spore.

The shape of the pustules is assumed to be an elliptic cylinder, where the length of major and minor axes are measured to be 1.02 ± 0.17 mm and 0.30 ± 0.04 mm, respectively, and the thickness is measured to be 0.21 ± 0.01 mm. The radius of *P. triticina* spores, r_s, is measured to be 9.7 ± 0.6 μm using a scanning electron microscope. Measuring the terminal velocity of individually falling spores, the density of *P. triticina* spores, ρ_s, is calculated to be 1294 ± 84 kg/m^3 (see Appendix A), whose value is close to the density of other microspores, such as the fungus spore [69] and pollen [70].

2.3.3 Drop impact conditions

A syringe needle was used to generate water drops of radius R_d ranging from 1.4 to 1.9 mm, within the range of the typical size of raindrops [71]. Drops were released from a certain height, falling under gravity, and then striking either an anchored leaf (cantilever) or a leaf fully supported by a rigid bottom. By varying the drop-releasing height from the substrate, the impact velocity of a water drop, U_d, is changed to be between 1.5 and 4.6 m/s. Thus, the corresponding Weber $We_d = \rho_d U_d^2(2R_d)/\gamma$ and Reynolds number $Re_d = \rho_d U_d(2R_d)/\mu_d$ of an impacting drop range from 88 to 1117, and from 4200 to 17480, respectively. Here we specially focused on drop impact on a rigid infected leaf to elucidate the fundamental mechanisms of vortex-induced spore spreading. In the time-scale comparison, the spreading time of water drops, $t_m \sim R_d/U_d$, is on the order of 1 ms, which is much less than the vibration time of leaves ($\sim$ 50 ms [72]). Thus, the vibration of the leaf by drop impact is assumed to

	Particle	ρ_s (kg/m^3)	r_s (μm)
I	Hollow glass sphere	1100	$1 - 10$
II	Soda Lime Sphere	2500	$19.0 - 22.5$
III	Soda Lime Sphere	2500	$45.0 - 53.0$

Table 2.1: Properties of artificial spores.

be insignificant to the initial liberation process of disease spreading. Also, we focused on the first impact of a simulated raindrop because the number of the removed spores were observed to rapidly decrease with the number of drop impacts and get removed within a few successive drop impacts [73].

2.3.4 Properties of artificial leaf and spores

Artificial leaf and spores were used to quantify the dynamics of disease spreading. For the artificial leaf, we used a polycarbonate (PC) film. For the artificial spores, we used micron-sized glass beads listed in table 2.1. When the glass beads were disposed onto a substrate, the thickness ranges between 100 and 250 μm, which is a similar value to the thickness of pustules. Here, the Stokes numbers of artificial spores I, II, and III are measured to be $0.001 - 0.13$, $1.1 - 1.5$, and $6.1 - 8.5$, respectively.

3

Dynamics of Splashed Droplets Impacting Wheat Leaves Treated with Fungicide

The content of this chapter was previously published as a journal manuscript in [74], and reproduced here with minor modifications. In this chapter we are trying to understand how the spore laden droplet can spread the disease to neighboring wheat plant after raindrop splashing.

3.1 Introduction

Wheat is the most widely grown crop in the world [75, 76]. Wheat contributes to about one quarter of the global food supply [75–77] and is projected to be 60% of the United States' food supply by 2050 [78]. Plant disease, such as Fusarium Head Blight (caused by the fungus *Fusarium graminearum*) and wheat leaf rust (caused by the fungus *Puccinia triticina* – figure 3.1(a),(b)), threaten this staple food crop [79, 80]. Consequently, new information is needed to understand the underlying physical mechanisms for the liberation and dispersal of plant pathogens governing

the spread of disease in wheat crops.

Strong winds can dislodge pathogens from a surface and carry them to neighboring plants [45, 46, 53, 81–83]. When rainsplash occurs on a diseased plant, the ejected satellite droplets can transmit pathogens (figure 3.1(c)) [7, 43, 73, 84]. Spores forced into the air by an impacting rain drop can get dispersed by air vortices also generated from the impact [37]. More recently, it was discovered that naturally occurring dew cycles can also liberate spores from wheat leaves [85]. The mechanism is the coalescence-induced jumping of micrometric dew droplets [2], which can propel adhered spores several millimeters above the leaf surface to clear the boundary layer [85]. For all of these rainsplash and condensation mechanisms, liberated spores can be carried by many kilometers in the wind after clearing the laminar boundary layer [45, 46, 53, 82, 83].

Wheat leaves exhibit a superhydrophobic surface wettability [86] comprised of micro/nano-scale surface roughness, which heavily influences the dynamics of impacting rain drops. For example, raindrops can easily splash or bounce from a superhydrophobic wheat leaf [37] and even dew droplets can spontaneously jump from the leaf upon naturally occurring coalescence events [85]. The dynamics of droplets impacting superhydrophobic surfaces has been widely studied [1, 23, 87–97]. In contrast to conventional surfaces, where the kinetic energy from impact is lost to viscous dissipation, a droplet landing on a superhydrophobic surface is able to bounce with a large restitution coefficient, ratio of the velocity before and after impact [1]. The time scale of droplet bouncing is capillary-inertial in nature (i.e. a balance between kinetic energy and surface energy) [87], although it can be shortened by using macroscopic features to break up a droplet [94, 96]. For a droplet impact at a sufficiently high Weber number, the ratio between inertia and surface tension, satellite droplets will be generated due to splashing [90, 91, 98]. During impact, a wetting transition can occur from the suspended Cassie state, where air pockets are trapped within

the surface roughness, to the impaled Wenzel state, in which the droplet will stick to the surface instead of bouncing off [88, 89, 93, 99]. This is because the contact angle hysteresis, which is the difference between droplet's advancing and receding contact angles, is dramatically larger for water in the Wenzel state compared to the Cassie state [22]. The mechanisms for this Cassie-to-Wenzel wetting transition include touch-down of the menisci to the bottom floor of the surface structure [23, 93] or the depinning and sliding of the menisci down the structure's side walls [100–102].

Returning to the specific case of rain-drops impacting a diseased wheat leaf, it is well known that splashed satellite droplets can liberate spores from the impacted leaf. However, as these spore-laden splashed droplets proceed to impact neighboring leaves, it is unknown whether they will bounce or stick to the surface. Such information is critical to understanding the limits of pathogen spread during rainfall.

In this study, an inclined superhydrophobic substrate was used to launch satellite droplets onto an adjacent wheat leaf fixed to a horizontal surface. Droplets were observed to either bounce from or stick to the leaf surface. Wheat leaves sprayed with a fungicide were substantially more likely to cause droplets to stick than untreated leaves, particularly when the anisotropic ridges of the leaf structure were orthogonal to the droplet's motion. These findings were rationalized with a scaling model that compared the droplet's kinetic energy to the energy required to dewet the partially impaled droplet from the leaf.

3.2 Materials and Methods

*Preparation of Wheat Leaves:*Winter wheat lines known to be susceptible to stem rust (Massey, and VA-135) were provided by the Griffey lab at Virginia Tech. Plants were propagated and inoculated as described in previous publications [37, 85]. Mature leaves were detached from plants and used for experiments within 48 hr. Figure 3.1a and 3.1(b) show an infected leaf and microscopic spores, respectively. Leaves

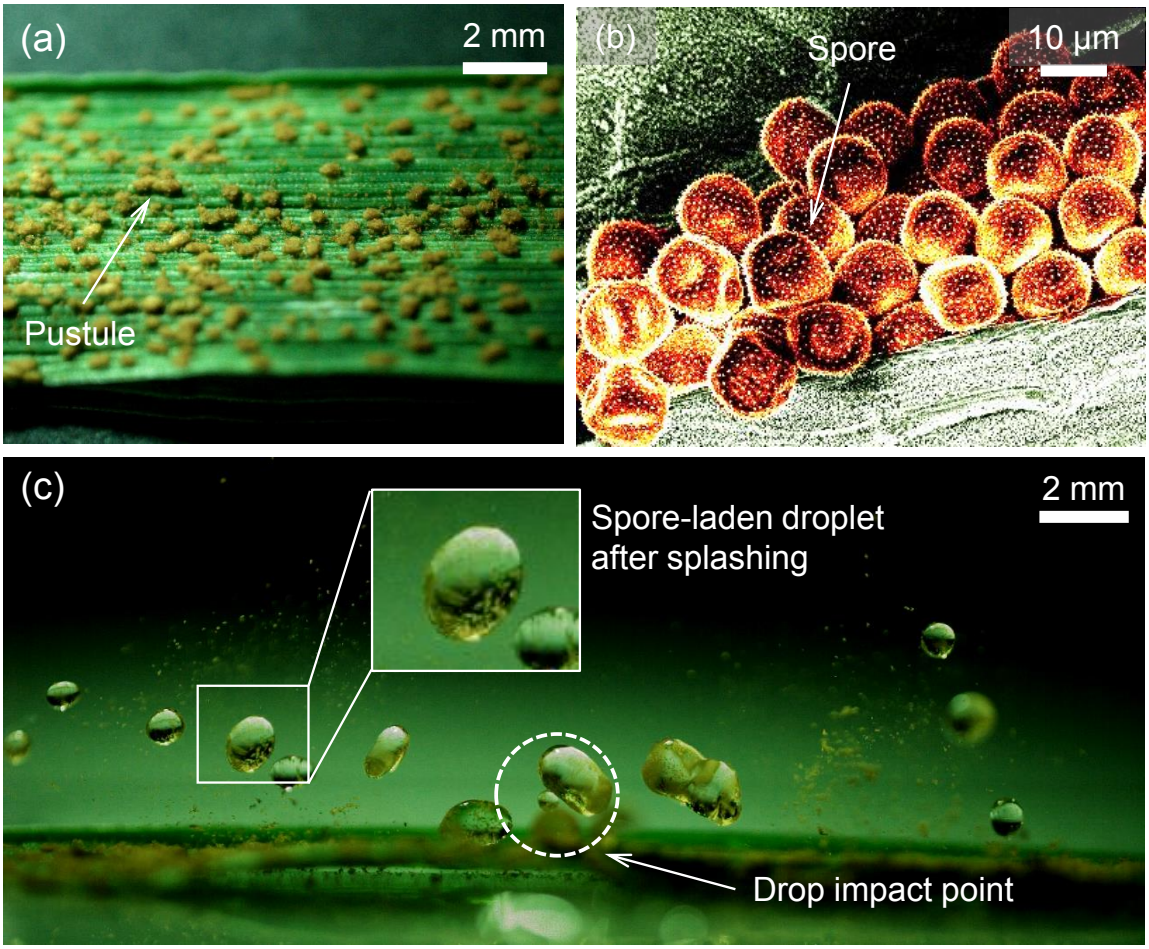

FIGURE 3.1: (a) Photograph of a wheat leaf infected with leaf rust. Rust pustules (uredinia) have emerged from the epidermis. (b) Scanning electron micrograph of a uredinium containing urediniospores. (c) Visualization of splashed satellite droplets generated by a droplet impacting a diseased wheat leaf. The initial droplet, of radius $R = 1.44\,\text{mm}$, impacted the leaf at a speed of $V = 2.4\,\text{m/s}$. Inset shows a magnified view of how the splashed satellite droplets are laden with spores.

were tested under two conditions: untreated (figure 3.2(a),(b)) and sprayed with a fungicide (figure 3.2(c)) leaves. For the leaves treated with fungicide, an 8:1:1 (by volume) solution of water, fungicide concentrate (Proline 480 SC Fungicide, Bayer CropScience), and surfactant (Top Surf, Winfield Solutions) was sprayed onto the leaves using an atomizer (Preval 267, Portable Sprayer System). Concentration (in water) for the treated leaves were 80 ppm for the fungicide (Proline 480 SC Fungicide, Bayer CropScience) and 125 ppm for the surfactant (Top Surf, Winfield Solutions).

The mixture of fungicide and surfactant was sprayed onto the leaves using an atomizer (Preval 267, Portable SprayerSystem). The fungicide concentrate contained 41% prothioconazole and 6% glycerine (by weight), while the surfactant contained alkylpolyethoxyalkylene ethers and other ethoxylated derivatives. For consistency, the atomizer was guided along the complete length of the leaf and back while actuated, with its position being approximately 5 cm away from the leaf's surface. High-speed imaging (Phantom v711, Vision Research) indicated a characteristic droplet diameter of approximately 70–100 μm diameter for the spray (see figure B1 in Appendix B). After receiving a fungicide treatment, sprayed leaves were allowed to dry for 2 hr in a fume hood prior to experiments. A small subset of experiments was done with infected leaves. Healthy 6-8-week-old leaves were inoculated with urediniospores of *P. triticina* and incubated in a dark and 100% humid environment for 24 h at 15°C to boost infection. After this incubation, the leaf moved back to the previously described growth conditions akin to recent reports [37, 85].

All of the wheat leaves exhibited an anisotropic ridge structure (figure 3.2(b)). These densely packed ridges had a characteristic width of 110 μm and a height of 6 μm. After drying, the fungicide spray did not noticeably affect the morphology of the leaf's surface structure (see , figure B3 in appendix B). This is in contrast to a separate work, where a different type of fungicide was used which deformed the wax structure of a wheat leaf [103]. Here, the effect of the fungicide on the surface of the leaf was deemed to be purely chemical in nature, resulting in an altered surface wettability.

The elasticity timescale is much longer than the spreading timescale for a raindrop impacting a leaf. The spreading timescale of water drops, t_m=R_d/U_d, is on the order of 1 ms, which is much less than the elastic response timescale (i.e. vibration timescale) of leaves ($\approx$ 10 ms) [72, 104]. The radius of curvature of a leaf is approximately 10 cm, which is much larger than the drop size (D = 500–1,000 μm).

Therefore, our experiments on a rigid flat leaf would be valid to understand how raindrops impact a leaf in nature.

Contact Angle Measurements: Two sets of advancing and receding apparent contact angles were measured: the static case of a sessile droplet and the dynamic case of an impacting droplet. The former case is useful for generally characterizing the wettability of a wheat leaf, while the latter accounts for a partial wetting transition that may occur upon dynamic impact. The contact angles were measured for all four combinations of untreated versus fungicide sprayed leaves and parallel versus perpendicular orientation of the leaf ridges with respect to the droplet motion. Static measurements were obtained using a contact angle goniometer (ramé-hart, Model 590) by the classic shrink-swell method (figure 3.3(b)). Dynamic measurements were obtained by using side-view high-speed microscopy to directly measure the advancing and receding angles during droplet impact. The dynamic advancing angle was measured as the droplet neared its maximum spreading diameter [105, 106], while the receding angle was measured in the early stages of droplet retraction [107–109]. (see figure B4 in Appendix B). For cases where the impacting droplet sticks instead of bounces, a receding angle was still observed during the partial retraction of the droplet. To promote a symmetric contact line, these dynamic contact angle measurements were performed with an orthogonal droplet impact with respect to the wheat leaf. This was achieved by directly depositing a $D \approx 1\,\text{mm}$ droplet using a pulled-glass needle, as the mesh technique for producing small droplets cannot control the angle of impact.

3.3 Results

Figure 3.3 shows the experimental results for satellite droplets impacting four different types of leaf surfaces: (I) Untreated leaf with droplet motion parallel to the leaf ridges, (II) Untreated leaf with droplet motion perpendicular to the leaf ridges,

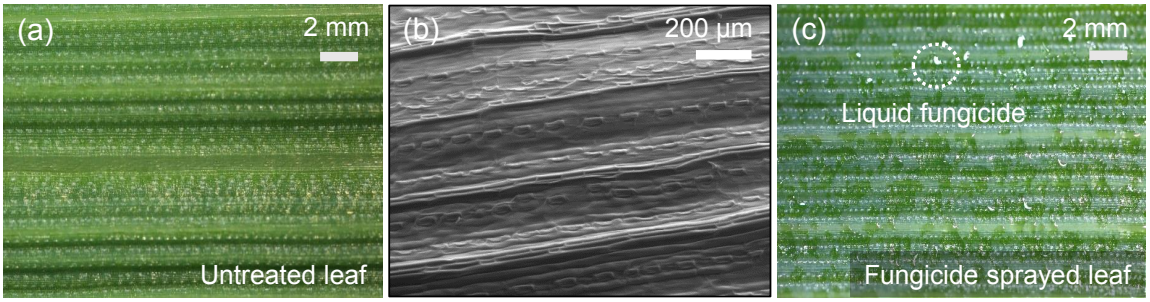

FIGURE 3.2: (a) Photograph of an untreated wheat leaf sample. (b) Scanning electron micrograph of an untreated wheat leaf, which visualizes the anisotropic micro-grooves that run along the surface. (c) Photograph of a wheat leaf after being sprayed with a fungicide solution. Prior to drying, a distribution of droplets containing the fungicide solution were visible along the surface. A white dotted circle is added to help visualize one of these droplets. The chemical constituents of the fungicide spray are provided in Materials and Methods.

(III) Fungicide sprayed leaf with droplet motion parallel to the leaf ridges, and (IV) Fungicide sprayed leaf with droplet motion perpendicular to the leaf ridges. As expected, droplets exhibited an increased contact angle hysteresis when the contact line was moving against the ridges as opposed to along. This is in agreement with previous measurements of hysteresis on micro-grooved surfaces [110, 111]. For both the untreated and fungicide sprayed leaves, the hysteresis was larger by about a factor of two for the perpendicular droplet motion compared to parallel. The effect of adding the fungicide spray was even more important than the leaf orientation, with a sprayed leaf exhibiting an order of magnitude increase in hysteresis compared to an untreated leaf with the same orientation. Therefore, surface I exhibited the lowest hysteresis ($\approx 4.3^\circ$) while surface IV exhibited the largest ($\approx 72.3^\circ$).

Figure 3.3(c) illustrates the four types of leaf surfaces (I–IV) used to test the dynamics of impacting satellite droplets. Corresponding time-lapse images are shown in figure 3.3(d), in which a high-speed camera captured the droplet trajectories from the side. For leaf I, all satellite droplets bounced off from the leaf surface several times. The bouncing motions continued until a droplet either fell off an edge of the leaf or very gradually came to a rest. For leaf II, most droplets bounced at

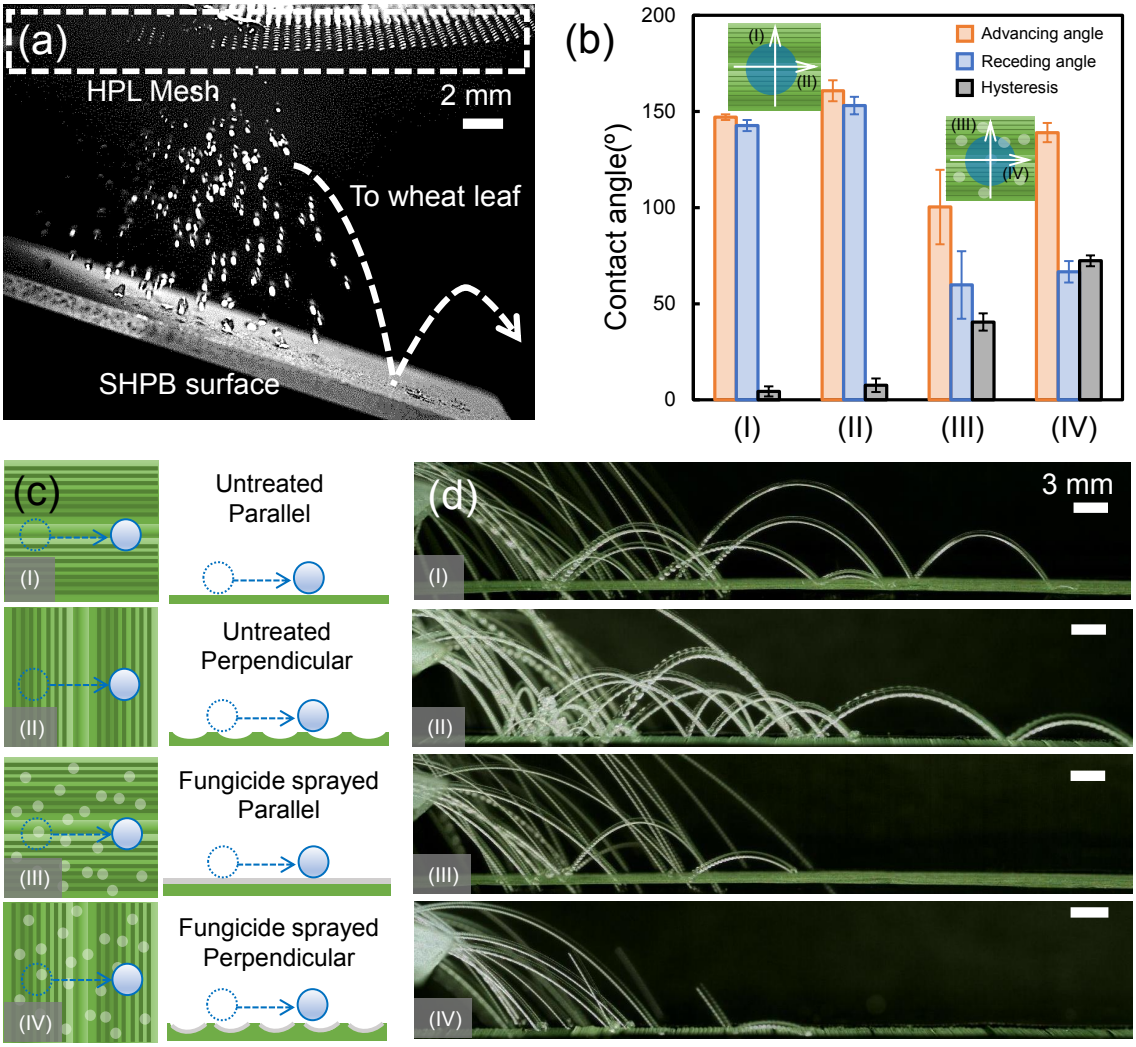

FIGURE 3.3: (a) Side-view photograph of the experimental setup used to trampoline satellite droplets from an inclined superhydrophobic surface onto an adjacent wheat leaf. (b) Apparent contact angles for sessile droplets on wheat leaves. Insets show the four different modes of wetting: untreated (I and II) or fungicide sprayed (III and IV) leaves, with the camera perspective (white arrows) measuring contact angles either parallel (I and III) or perpendicular (II and IV) to the ridges. Error bars represent a standard deviation from an average of three trials. (c) Schematic of dynamic droplet motion along the four different types of leaf surfaces (I–IV). (d) Time-lapse photography capturing the trajectories of satellite droplets bouncing or sticking as they move along the four types of wheat leaves. The duration of the time-lapse image is about 260 ms for leaves (I) and (II) and 120 ms for (III) and (IV).

least once, but not as many times as with leaf I. In some cases, droplets failed to bounce even following their first impact. The less frequent bouncing events could

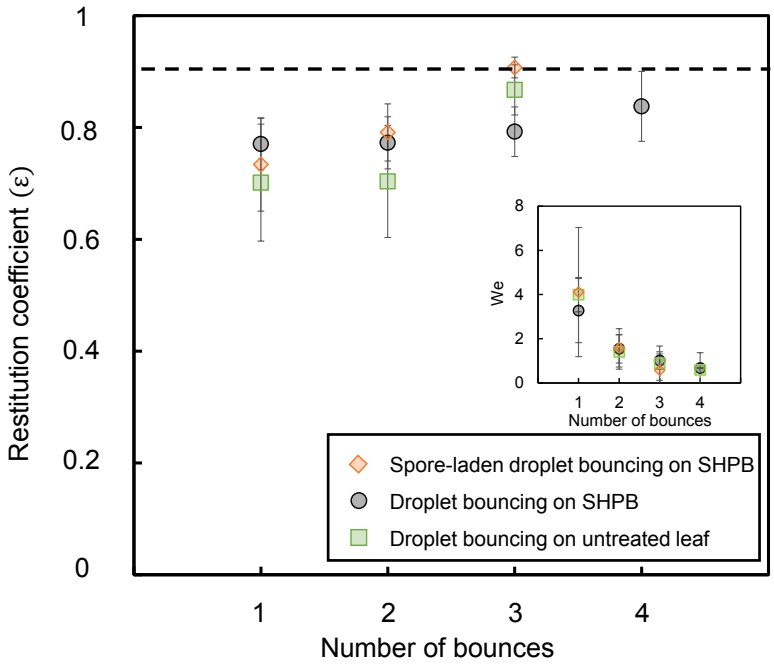

FIGURE 3.4: Restitution coefficients for three different cases: clean satellite droplets (no spores) impacting an untreated wheat leaf where the tangential component of the droplet velocity is parallel to the leaf ridges (green squares), spore-laden satellite droplets impacting a superhydrophobic surface (orange diamonds), and clean droplets impacting a superhydrophobic surface (gray circles). Restitution coefficients were calculated by comparing the normal component of velocity before and after impact. The horizontal dashed line corresponds to a restitution coefficient of $\epsilon \approx 0.9$ found from a previous report using a different type of superhydrophobic surface [1]. Inset: the slight increase in the restitution coefficient for later bounces is correlated with a decrease in the Weber number.

be attributed to the higher hysteresis of droplet motion perpendicular to the leaf ridges. It is possible for droplets to exhibit jetting or splitting during impact on superhydrophobic surfaces [98, 112, 113]. These behaviors were not observed here, due to the small Weber number of the satellite droplets. With leaf III, a few droplets were still able to bounce, but most droplets did not bounce at all, likely due to the dramatic increase in hysteresis caused by the fungicide and low receding angles less than 100° [114]. Finally, for case IV which exhibited the largest hysteresis, no bouncing events were observed. Note that for leaves II and IV, an array of leaf pieces had to be arranged side by side due to the small width ($\approx 1\,\text{cm}$) of wheat leaves. In these cases, we did not analyze a subset of trials where the droplets happened to

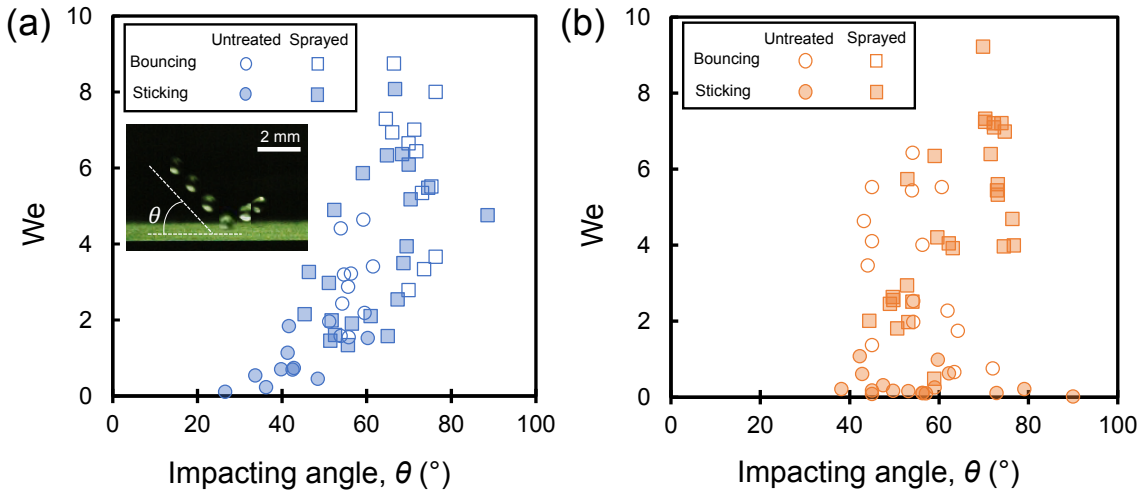

FIGURE 3.5: Weber number of satellite droplets impacting a wheat leaf versus the angle of impact with respect to the horizontal. Filled symbols indicate trials where the droplet exhibited sticking upon impact, whereas open symbols denote bouncing behavior. Circles and squares represent untreated and fungicide sprayed wheat leaves, respectively. The two plots separate leaf ridge orientations of (a) parallel (blue data points) and (b) perpendicular (orange data points) with respect to the path of droplet motion.

impact a seam between adjacent leaves.

For ease of experimentation, the above tests were performed on healthy leaves that did not have pathogenic spores on their surface. However, in order to extend our findings to the desired context of disease transmission, we performed additional experiments validating that spores do not affect the droplet dynamics. This can be seen in figure 3.4, where the restitution coefficient of bouncing droplets was the same for both clean and spore-laden droplets. The spore-laden droplets were obtained by using a diseased wheat leaf as the inclined surface, rather than the usual superhydrophobic substrate. By trampolining the satellite droplets from the diseased leaf, spore-laden droplets were directed to a flat superhydrophobic substrate to measure the restitution coefficient. To ensure that the restitution coefficient of a flat superhydrophobic surface is equivalent to a flat wheat leaf, we also measured the restitution coefficient of a clean satellite droplet bouncing onto a superhydrophobic surface. In all three cases, the restitution coefficient was $\epsilon \approx 0.78 \pm 0.03$ averaged

across the first four bounces of a droplet. This is slightly smaller than the upper value of $\epsilon \approx 0.9$ observed on an ideal superhydrophobic surface [1], as our superhydrophobic surfaces exhibited appreciable contact angle hysteresis. The restitution coefficient did increase slightly as the Weber number decreased, in agreement with previous reports [89, 113, 115, 116]. These results validate that the bouncing versus sticking behavior of our clean droplets will be functionally equivalent to when the droplets are carrying spores.

Figure 3.5 shows bouncing versus sticking events while also quantifying each droplet's Weber number (We) and impact angle (θ). The Weber number describes the ratio between inertia and surface tension, which is defined as $\mathrm{We} = \rho V^2 D/\gamma$, where ρ is the density of water, D is the diameter of impacting droplet, and V is the total velocity of the impacting droplet. For all four types of leaf surfaces, droplets became stuck when impacting at a low We. For both untreated cases (leaves I and II), the data were sorted into two different categories (i.e. bouncing and sticking) and compared to the Weber number. The p-values in each group were 0.0002 and 0.0001 respectively (< 0.01), which indicates that the statistically significant transition can happen at $\mathrm{We_c} \approx 2$. However, for the fungicide sprayed leaf (square data points), bouncing did not occur for the perpendicular case (leaf IV) and rarely was observed for the parallel case (leaf III) because of the heterogeneous nature of the spray. The statistical analysis showed that there was a statistically less significant transition for leaves III and IV with a p-value of 0.015 (> 0.01). In terms of the impact angle, a previous study showed that bouncing drops with high We numbers were observed above a critical angle ($\theta \sim 40°$) [98]. With high impact angles, the bouncing dynamics is governed by both normal and tangential components of inertia while the tangential component mostly contributes to the lateral sliding. Since our study focuses on high impact angles ($\theta \gtrsim 40°$) as in natural situations, our energy-balance model hereinafter can predict the bouncing-to-sticking transition.

It may be tempting to only use the vertical component of velocity when calculating We. However, for the untreated wheat leaves I and II, we observed that the contact angle hysteresis of an impacting droplet is appreciably larger than that measured for sessile droplets (see figure B4 in Appendix B). This indicates that a local wetting transition occurs due to the droplet impact. It is well known that droplets in a full Wenzel state are irreversibly impaled within the surface texture [89,92,108,117–119]; therefore, the ability of our impacted droplets to bounce indicates a partial wetting state. We hypothesize that the horizontal component of velocity is, counterintuitively, also useful for promoting bouncing, as it allows the droplet to slide away from the local region of partial impalement [120]. For the leaves sprayed with fungicide (III and IV), there was no appreciable difference in hysteresis for sessile versus impacting droplets (see figure B4 in Appendix B). This is because the wetting state is now dominated by the hydrophilic chemical deposits, which applies to both static and impacting droplets. Both the dried fungicide deposits and fungicide-free regions of the sprayed leaf had characteristic length scales of $\approx 1\,\mathrm{mm}$, comparable to the size of the impacting satellite droplets. Therefore, most droplet impacts would at least partially contact a high-hysteresis fungicide deposit, such that lateral motion to a fungicide-free region would be beneficial. In short: the vertical component of inertia facilitates the spreading and retraction essential for bouncing, but is simultaneously aided by the horizontal inertia reducing the hysteresis that impedes retraction.

To predict whether any given droplet will bounce or stick, we compared its kinetic energy from impact to its pinning energy due to contact angle hysteresis. The pinning energy of a droplet can be approximated by:

$$E_\mathrm{p} \approx \pi R^2 \gamma (\cos\theta_\mathrm{R} - \cos\theta_\mathrm{A}) \tag{3.1}$$

where R is the radius of a spherical satellite droplet before impact, γ is the surface tension of water, and θ_A and θ_R are the apparent advancing and receding contact

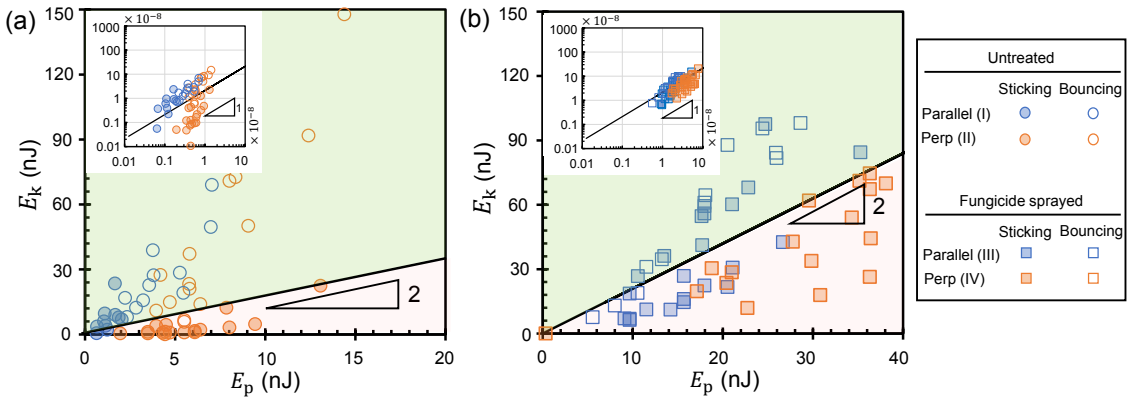

FIGURE 3.6: Regime maps demarcating bouncing (green region) versus sticking (pink region) behaviors for satellite droplets impacting (a) untreated or (b) fungicide sprayed wheat leaves. Dynamic angles were used for (a) and static angles were used for (b). The critical line separating the two regimes is given by Eq. 3.3, with the slopes representing the fitted value of $\beta \approx 2$. Small inset shows the data plotted in logarithmic scale.

angles, respectively. We note that Eq. 3.1 is a very simplistic estimation of the pinning energy, as the area of the droplet prior to impact will not be equal to the area of the solid-liquid contact area after impact. However, this approach allows us to use the equation universally, regardless of the exact angle of impact or dynamic shape of the droplets. The kinetic energy provided from impact is given by:

$$E_k = \frac{1}{2}\rho\left(\frac{4}{3}\pi R^3\right)V^2 \tag{3.2}$$

where ρ is the density of water.

Figure 3.6 demarcates bouncing versus sticking behavior by graphing the critical line where the kinetic energy matches the pinning energy:

$$E_k = \beta E_p, \tag{3.3}$$

where β is a geometrical pre-factor. Figure 3.6a shows the regime map for droplets impacting untreated leaves (I and II). When assigning a value of $\beta \approx 2$, the line plotted by Eq. 3.3 bisects the bouncing and sticking events. Bouncing droplets tended to fall above the line, where the kinetic energy can exceed the pinning energy. Sticking

droplets fell on or beneath the critical line. Similarly, figure 3.6b shows results for fungicide sprayed leaves (III and IV), with the same pre-factor of $\beta \approx 2$. For leaf IV, the contact-angle hysteresis is so large as to prevent bouncing entirely, so no bouncing data could be produced to validate the theoretical crossover line.

The small inset in figure 3.6 shows all of the data plotted in a logarithmic scale (both axes). Even though leaf I (blue circles) is not a perfect fit between the experiment and theoretical values, the other three leaf configurations (II, III, and IV) are all well-matched with the theoretical crossover line. One possible explanation of this disparity is that leaf I exhibits the smallest contact angle hysteresis, such that the critical kinetic energy to achieve bouncing is substantively smaller than with the other types of leaves. Perhaps the model's assumption that all of the kinetic energy may be used to overcome pinning begins to break down at very small Weber numbers, where it is more difficult to deform the droplet's shape upon impact to slide away from a local defect. We also note that, while leaves II–IV have a good overall agreement with the theory, the experimental crossover is of course not as sharp as the theoretical one due to the surface inhomogeneity of leaf samples. Finally, if 100 μm diameter splashed droplets were used instead of 500–1,000 μm, we would expect that sticking events would dominate, as $E_\mathrm{p} \propto D^2$ compared to $E_\mathrm{k} \propto D^3$.

In addition to the dynamic pressure caused by the kinetic energy, a droplet will also generate a water hammer pressure upon impacting a substrate [29, 121, 122]. The water hammer pressure is due to the rapid deceleration of the droplet upon contacting the surface, and is expressed as [29]:

$$E_\mathrm{WH} = \kappa_\mathrm{WH}\, \rho\, C V\, \frac{4}{3}\pi\, R^3, \tag{3.4}$$

where κ_WH is the water hammer pressure coefficient and C is the speed of sound in water. For the satellite droplets used here, $E_\mathrm{WH} \sim 10^3$ nJ, one order of magnitude larger than the kinetic energy ($E_\mathrm{k} \sim 10^2$ nJ). However, this water hammer pressure

is highly localized, with a length scale of [29]:

$$d_{\mathrm{WH}} = \frac{D_0 V}{C}, \tag{3.5}$$

where D_0 is the diameter of impacting droplet. Beyond which the shock waves reach the free surface of the droplet and dissipate. Here, $d_{\mathrm{WH}} \approx 1\,\mu$m, which is negligibly small compared to our maximal droplet spreading diameter of about 1 mm. Therefore, the water hammer pressure is only relevant in terms of initiating a localized wetting transition upon impact, especially for leaf types (I) and (II) as discussed above. In terms of the bouncing dynamics, only the kinetic energy can be harnessed due to its larger time and length scales of operation.

3.4 Conclusions

We studied the dynamics of splashed satellite droplets impacting wheat leaves in different orientations and with and without a fungicide. The final fate of a droplet: bouncing versus sticking, was governed by a competition between its kinetic energy and pinning energy. The pinning energy, caused by contact angle hysteresis, was found to depend on the orientation of the anisotropic leaf ridges with respect to the path of droplet motion. When the ridges ran parallel to the droplet motion, droplets bounced several times, while bouncing was less probable for perpendicular ridges. When spraying wheat leaves with a fungicide, the pinning energy was found to increase dramatically. For the fungicide-sprayed leaves, bouncing was observed occasionally for the parallel ridge orientation, but sticking always occurred for the perpendicular orientation even for the initial droplet impact events.

Ironically, these results indicate that wheat leaves treated with a fungicide solution (a mixture of fungicide, surfactant, and water) can actually aid in the transmission of leaf rust during rainfall. It is well known that rainsplash can carry pathogenic

material, for example by scavenging spores from the air or from the initial impact with a diseased plant [7, 43, 73, 84]. The fungicide treatment causes these spore-laden splashed droplets to stick onto secondary leaves, which can result in disease spread. In contrast, spore-laden droplets are prone to rebouncing (without depositing pathogenic spores) from untreated wheat leaves. Therefore, fungicide applications may be helping to promote the very diseases they are seeking to prevent. Consequently, wheat producers should consider the timing of fungicide applications with regards to major rainfall events. It is important to note that the findings presented here have some important limitations. First, our experiments were conducted in the laboratory under controlled environmental conditions. Wheat plants grown under field conditions could have different characteristics (e.g., be naturally-infected with different plant pathogens, contain areas of necrotic or senescing tissue, etc.). Consequently, future experiments with field-grown wheat plants harboring leaf rust are warranted. Second, our study focused on a limited number of wheat genotypes known to be susceptible to leaf rust. Future studies could include additional wheat genotypes that vary in their resistance to leaf rust. These additional studies might also include genotypes that vary in leaf morphology and architecture. Despite these limitations and the call for future work, our results shed new light on how leaf rusts are spread during rainfall on leaf surfaces treated with a fungicide application. Such work is important for the integrated management of leaf rusts and other plant diseases worldwide.

4

Using Frost to Promote Cassie Ice on Hydrophilic Pillars

The content of this chapter was previously published as journal manuscripts in [123], and reproduced here with minor modifications. In this chapter we are trying to show the new concept of Cassie ice without any nano structure and chemical coating.

4.1 Introduction

Various types of surface coatings have been developed that reduce ice adhesion strength for enhanced de-icing functionality. Micro/nano-structured surfaces impregnated with a nonvolatile lubricating oil can significantly reduce the ice adhesion strength relative to smooth surfaces [124], while also facilitating gravitational shedding during thermal defrosting [125]. Soft elastomeric coatings have been shown to greatly reduce the ice adhesion strength down to $\tau < 1\,\mathrm{kPa}$, particularly when adding uncross-linked polymeric chains at the interface to promote slippage [126]. By dispersing particles exhibiting a low shear modulus within a substrate with a

high shear modulus, stress-localized fracture and removal of ice at $\tau \sim 1\,\mathrm{kPa}$ was demonstrated [127]. Coatings exhibiting a low interfacial toughness, for example polypropylene, enable large areas of ice to be shed with a low and area-independent force [128].

The past decade has seen a flurry of efforts to leverage micro/nano-structured superhydrophobic surfaces for anti-icing or de-icing applications. Supercooled water tends to exhibit the suspended Cassie state on a superhydrophobic surface, which enables cooperative anti-icing mechanisms: a delay in heterogeneous ice nucleation [26, 27] and greatly enhanced droplet mobility [22], such that droplets can slide [28], bounce [26], or jump [2] from the surface before freezing can occur. In a humid environment, condensation frosting via inter-droplet ice bridging is inevitable [30, 129], but on a nanostructured superhydrophobic surface this frost can exhibit the Cassie state [130]. The adhesion strength of Cassie ice/frost is reduced by a factor of 15 compared to a highly smooth surface [131], while also facilitating dynamic shedding upon partial melting (i.e. dynamic defrosting) [130]. However, it is now common knowledge that neither the nanostructures nor their conformal hydrophobic coatings are durable under rugged conditions [132, 133].

Here we use frost-tipped aluminum pillars to trap impacting supercooled droplets in a Cassie state without requiring a nanostructure or hydrophobic coating. While a recent work has similarly demonstrated the ability to preferentially grow frost atop a surface structure [134], here the frost tips are not the endgame but rather the means to subsequently trap freezing droplets in a Cassie state. Our scaling model reveals that the Cassie ice is enabled by the rapid wicking of impacting water into the porous frost tips, which out-competes the time scales for impalement or freezing.

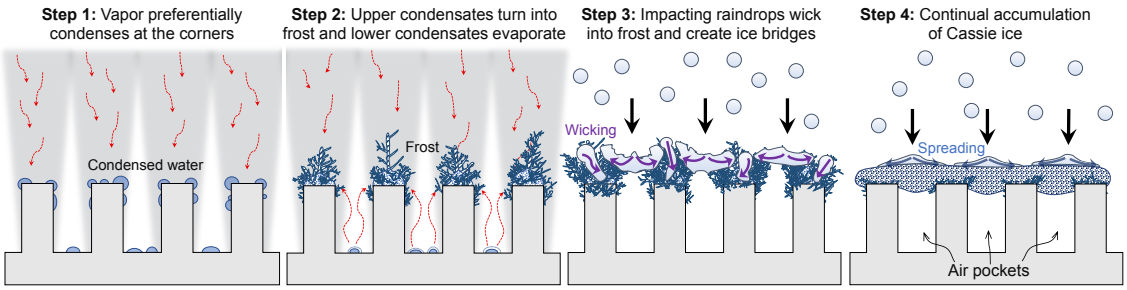

FIGURE 4.1: Conceptual overview of our non-superhydrophobic technique to trap frost and ice in the Cassie state. Supercooled condensation primarily grows on top of the pillars due to their extrusion into the concentration boundary layer (Step 1). As this upper condensate freezes, it evaporates any underlying condensate due to the hygroscopic nature of ice to result in Cassie frost (Step 2). Rain or fog droplets impacting the surface will wick inside of the Cassie frost and get arrested, preventing impalement (Step 3). As droplets continue to impact the surface, the result is a continuous layer of Cassie frost/ice suspended above air pockets (Step 4).

4.2 Results

Figure. 4.1 is a conceptual overview of our hypothesized new approach to trapping frost and ice in the Cassie state on uncoated pillars. Under chilled and supersaturated conditions, supercooled condensation should preferentially nucleate on sufficiently tall ($\sim 1\,\mathrm{mm}$) pillar tops. This is because the sharp corners enhance diffusion [33, 135] while the millimetric height allows the pillar tops to protrude beyond the concentrated barrier of non-condensable gas [136]. Freezing should therefore occur first for the larger condensate atop the pillars, which will subsequently evaporate any lower condensate due to the hygroscopic nature of frost [137, 138]. After frost is grown atop the pillars, we hypothesize that impacting supercooled droplets will freeze on top of the pillars in the Cassie state.

An array of aluminum square pillars, of width $w = 0.5\,\mathrm{mm}$, height $h = 1\,\mathrm{mm}$, and edge-to-edge pitch of $p = 1.5\,\mathrm{mm}$, were machined (see figure. C5.1 Appendix C). The micropillared surface was subjected to condensation frosting by thermally bonding it to a Peltier stage chilled to a temperature T_s in an air environment of temperature

T_∞ and relative humidity RH. Side-view time-lapse photography was employed to compare two different conditions for growing frost: $T_s = -20 \pm 1°C$, $T_\infty = 22\,°C$, and $RH = 71.5\%$, or $T_s \approx -7\,°C$, $T_\infty = 3.2\,°C$, and $RH = 73.6\%$. The former case has an extreme supersaturation of $S = 15$, whereas the latter is a more naturally realistic $S = 1.5$. Supersaturation is defined as the ratio of the partial pressure of water vapor in the ambient, $P_\infty = P_{sat}(T_\infty)RH$, compared to the saturation pressure for liquid water at the surface, $P_w = P_{sat}(T_s)$. In both cases, the frost was observed to grow predominantly atop the pillars (figure. S2) and evaporate any secondary condensation from between the pillars (figure. S3).

Figure. 4.2 shows high-speed imaging for droplets impacting the frosted pillar tops under different conditions. figure 4.2(a) shows droplet impact where the ambient was room temperature, $RH = 20\%$ and $T_\infty = 21\,°C$, while the aluminum substrate was chilled to $T_s \approx -40\,°C$. Frost was allowed to grow for about 20 min prior to droplet impact, which resulted in a frost thickness of about 2 mm extending above the pillar tops. Once frost growth reached the steady state situation in which the frost tips approach the dew point temperature for ice ($T_{frost,tip} \approx -3\,°C$) [139], a room temperature water droplet was released to elucidate its dynamics on the frosted pillars. The droplet exhibited a diameter of $D = 3.4$ mm and was room temperature prior to impacting the frost-tipped surface at a speed of $U = 0.8$ m/s. The warm droplet melted the frost within milliseconds of impact, such that it impaled the hydrophilic aluminum pillars in the Wenzel state. The frost layer was nearly continuous between pillars, indicating that even a robust frost-tipped surface cannot repel warm water.

Figure 4.2(b) shows the opposite case of a supercooled droplet impacting the frost. The frost was grown under identical conditions described above for $S = 1.5$ for about 2.5 hr. After growing the frost atop the pillars, the surface was directly moved into a walk-in freezer where $RH = 75.4\%$ and $T_\infty = T_s = -22\,°C$. Under these isothermal

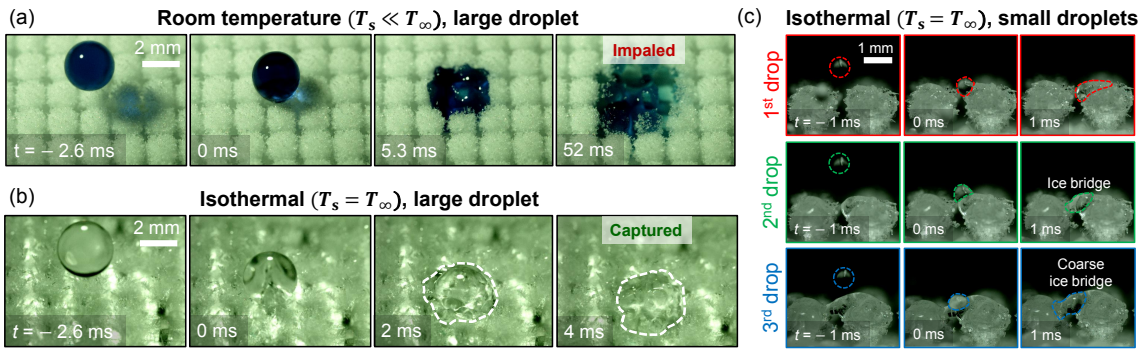

FIGURE 4.2: High-speed photography of water droplets impacting aluminum pillars exhibiting Cassie frost (see Video S3, S4 in the Supplemental material). (a) When the impacting droplet ($D = 3.4\,\text{mm}$) and ambient are room temperature ($T_\infty = 21.0\,^\circ\text{C}$), the droplet melts the frost to impale in the Wenzel state (even when the substrate is chilled to $T_s \approx -40\,^\circ\text{C}$). (b) Under near-isothermal conditions in a walk-in freezer ($T_\infty = -22\,^\circ\text{C}$), an impacting supercooled droplet ($D = 2.9\,\text{mm}$) becomes arrested by the frost tips to produce Cassie ice. (c) After three different microdroplets ($D \approx 500$–$1{,}000\,\mu\text{m}$) successively impacted the same region over time, a continuous ice bridge was formed between adjacent frost tips.

conditions, a droplet of size $D = 2.9\,\text{mm}$ impacted the frosted pillar tops at a speed of $U \approx 0.7\,\text{m/s}$. To prevent the freezing of water from within the metal syringe needle, the syringe was filled with a bath of ice water held in the docking bay to the freezer (where $T_\infty \approx 3\,^\circ\text{C}$). Nonetheless, the droplet was certainly supercooled by the time of impact, given that the syringe was in the freezer for about 1 min prior to dispensing the water Indeed, the supercooling was evidenced by the necessity of using a smaller needle to avoid freezing prior to dispensing, hence the slightly smaller droplet size of $D = 2.9\,\text{mm}$ instead of 3.4 mm. Under these conditions, the supercooled droplet froze on the overlying frost in a Cassie state, such that the aluminum pillars themselves remained dry.

For many practical systems, icing is not only caused by rain droplets but also by microscopic droplets suspended in clouds or fog. Therefore, we additionally impacted our frost-tipped pillars with supercooled microdroplets, to see if they can get similarly trapped in an arrested Cassie state. Similar to previous reports [74, 140],

the microdroplets were generated by impacting a millimetric droplet onto a steel mesh, which produced multiple $D \approx 500$–$1{,}000\,\mu\text{m}$ satellite droplets. The frost was grown for 10 min where $T_\text{s} = -20\,^\circ\text{C}$, $T_\infty = 23.8\,^\circ\text{C}$, and $RH = 63.5\%$ (resulting in a supersaturation of $S = 15$). After the frost was grown, the surface was brought into the walk-in freezer to ensure near isothermal conditions ($T_\text{s} = -12\,^\circ\text{C}$, $T_\infty = -12\,^\circ\text{C}$, and $RH = 69.80\%$). As shown in figure 4.2(c) and S4,for sufficiently coarse frost tips, at least a portion of each droplet impacted a frost tip(s) and could not penetrate between the pillars. After enough impact events, the microdroplets were able to completely bridge the gaps between adjacent frost tips. This culminated in a continuous sheet of ice/frost suspended on top of the aluminum pillars (figure S5).

The Cassie state is only possible when the impacting droplet gets arrested before its menisci can appreciably invade the gaps between the frost-tipped pillars (figure 4.3(a,b)). From figure 4.2(a), where arrest was not possible due to the warm temperature of the droplet, it was observed that the impalement speed was approximately equal to the impact speed. More quantitatively, side-view high-speed imaging indicated that water menisci invaded the gaps between pillars at a speed that was only 2% slower than the impact speed. This is due to the large (1.5 mm) edge-to-edge separation (p) between pillars, and was also observed for droplets impacting similarly-scaled hairy structures [141]. If the frost tips grow to a much larger projected diameter than the pillars, this would reduce the gap size the water penetrates through but the same approximation seems to hold in most cases. If we define a successful Cassie state as preventing the meniscus from advancing beyond the upper frost tips, it follows that the impalement time scales as:

$$t_\text{impale} \sim \frac{h_\text{f}}{U}. \tag{4.1}$$

where h_f is the height of the frost grown on the top of each micropillar. Taking a typical case of $h_\text{f} \sim 1\,\text{mm}$ and $U \sim 1\,\text{m/s}$ results in $t_\text{impale} \sim 1\,\text{ms}$.

Regarding the specific mechanism for hydrodynamic arrest, there are several possibilities. Recent studies have characterized the arrested hydrodynamics of supercooled droplets impacting a chilled surface due to freezing [142–145]. The most obvious hypothesis is that freeze fronts can propagate laterally to freeze the menisci before they can invade the pillars. For the case of a supercooled droplet, these freeze fronts would begin immediately upon contacting the frost-tipped pillars. The rate of freeze front propagation is obtained by balancing conduction through the frost and the latent heat of fusion:

$$\rho_{\mathrm{i}} L v_{\mathrm{freeze}} \sim k \frac{\Delta T}{\Delta x}. \tag{4.2}$$

where $\rho_{\mathrm{i}} = 917\,\mathrm{kg/m^3}$ is the density of ice, $L = 334 \times 10^3\,\mathrm{J/kg}$ is the latent heat of fusion, $k \sim 1\,\mathrm{W/m{\cdot}K}$ scales as the effective thermal conductivity of water/ice, and Δx is the corresponding lateral length scale across which heat is conducted. The temperature differential between the 0 °C freeze front and freezer temperature is on the order of $\Delta T \sim 10\,^{\circ}\mathrm{C}$. For larger droplets ($D \sim 1\,\mathrm{mm}$) completely spanning the gap between adjacent frost tips, $\Delta x \sim p/2$. For microdroplets which only partially

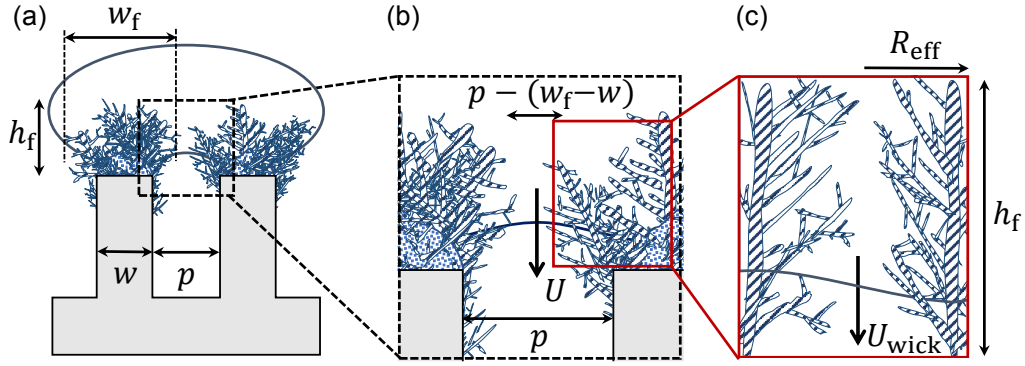

FIGURE 4.3: Model schematic for predicting whether frost-tipped pillars can trap an impacting supercooled droplet in the Cassie state. (a) When the droplet impacts the frost tips, the dynamic pressure will simultaneously: (b) Drive the water into the gaps between the frosted pillars, and (c) Wick the water into the frost tips themselves, which have an effective pore radius of $R_{\mathrm{eff}} \approx 10\,\mu\mathrm{m}$. The Cassie state will be enabled if the water can wick within the frost faster than it can fall between the frost tips.

span an air gap, $\Delta x \sim D/2$. The time required to freeze each meniscus, from freeze fronts propagating from opposing frost-tipped pillars, is then given by:

$$t_{\text{freeze}} \sim \frac{1}{2}\frac{p-(w_{\text{f}}-w)}{v_{\text{freeze}}} \sim \frac{(p-(w_{\text{f}}-w))\rho_{\text{i}} L \Delta x}{2k\Delta T}. \tag{4.3}$$

Using a representative scenario of $p-(w_{\text{f}}-w) \approx 200\,\mu\text{m}$ and droplet diameters ranging from $D \approx 0.5$–$3\,\text{mm}$, we obtain $t_{\text{freeze}} \sim 0.1$–$1\,\text{s}$. This indicates that the freezing of menisci between pillars cannot be the arrest mechanism after all, as $t_{\text{freeze}} \gg t_{\text{impale}}$.

To consider a second possible arrest mechanism, the droplet volume may be wicking inside of the porous frost tips. The ability of a liquid to wick inside of dendritic frost only recently came into appreciation [25, 146, 147]. For our case of an impacting droplet wicking inside of the surface's frost-tipped pillars, we hypothesize that the dynamic pressure replaces capillarity as the dominant driving force. The inertial force of an impacting droplet is given by $F_{\text{i}} \sim \rho D^2 U^2$. The resultant capillary force is given by $F_\gamma \sim \gamma R_{\text{eff}}(D/R_{\text{eff}})$, where $\rho \approx 1{,}000\,\text{kg/m}^3$ and $\gamma = 7.56 \times 10^{-2}\,\text{N/m}$ are the density and surface tension of water at $0\,^\circ\text{C}$, respectively, and $R_{\text{eff}} \approx 10\,\mu\text{m}$ is the effective pore radius of a typical frost sheet [25]. The D/R_{eff} ratio crudely scales as the total number of frost pores beneath an impacting droplet. For a representative scenario of $D \sim 1\,\text{mm}$ and $U \sim 1\,\text{m/s}$, this results in $F_{\text{i}} \sim 1\,\text{mN}$ being much larger than $F_\gamma \sim 100\,\mu\text{N}$, validating the hypothesis. The resisting viscous force is given by

$$F_\mu \sim \mu \frac{(h/t_{\text{wick}})}{R_{\text{eff}}}(R_{\text{eff}} h)\frac{D}{R_{\text{eff}}} \sim \frac{\mu h^2 D}{t_{\text{wick}} R_{\text{eff}}}. \tag{4.4}$$

where $\mu = 1.79 \times 10^{-3}$ Pa·s is the dynamic viscosity of water, $U_{\text{wick}} \sim h/t_{\text{wick}}$ is the effective wicking velocity, and h is the vertical extent of wicking necessary to contain the water within/between the frost tips. We used a simplified approximation of each pore tunneling straight through the frost of depth h_{f} (figure 4.3(c)). Balancing F_{i} and F_μ yields the estimated time scale for the droplet's water to fully wick inside of

the frost:

$$t_{\text{wick}} \sim \frac{\mu h^2}{R_{\text{eff}} \rho U^2 D}. \tag{4.5}$$

For the case of larger droplets ($D \approx 3\,\text{mm}$), $h \sim h_{\text{f}}$, and Eq. 4.5 results in $t_{\text{wick}} \sim 100\,\mu\text{s}$ for $U \sim 0.5\,\text{m/s}$. For smaller droplets ($D \approx 0.5\,\text{mm}$), $h \sim D$ from volume conservation, and Eq. 4.5 results in $t_{\text{wick}} \sim 100\,\mu\text{s}$ when $U \sim 1\,\text{m/s}$. In either case, this is an order of magnitude faster than $t_{\text{impale}} \sim 1\,\text{ms}$. This strongly indicates that, well before impalement between pillars can occur, the water wicks within the frost tips to become safely sequestered atop the pillars.

Of course, frost wicking is only a viable arrest mechanism if it can encompass an appreciable fraction of the impacting droplet's volume. For the largest droplet size used here, $D \approx 3\,\text{mm}$, the droplet tended to impact four frost-tipped pillars. The volume of each frost tip is estimated by $V_{\text{frost}} \approx w_{\text{f}}^2 h_{\text{f}}$, which for $w_{\text{f}} \approx 2\,\text{mm}$ and $h_{\text{f}} \approx 1\,\text{mm}$ results in $4V_{\text{frost}} \approx 16\,\text{mm}^3$. When a frost sheet is defrosted, the resulting meltwater film is approximately one fourth the height of the original frost [130]. This indicates that the void volume within a frost tip is about $V_{\text{void}} \approx 3\,\text{mm}^3$, such that $4V_{\text{void}} \approx 12\,\text{mm}^3$. This compares quite favorably to the droplet volume of $V_{\text{drop}} \approx 14\,\text{mm}^3$, especially when considering that water can be freely suspended in the air between the frost tips.

Frost wicking is only possible if the water is able to wick completely inside of the frost before it freezes over into solid ice. As shown in figure 4.3(c), consider supercooled water wicking inside of frost with an effective pore radius of $R_{\text{eff}} \approx 10\,\mu\text{m}$. This wicking would itself get arrested once a freeze front propagates by about R_{eff} from either side to seal each pore. The speed of a freeze front within a pore is given by $v_{\text{freeze,pore}} \approx (k_{\text{i}} \Delta T)/(\rho_{\text{i}} L R_{\text{eff}})$, such that:

$$t_{\text{freeze,pore}} \sim \frac{R_{\text{eff}}}{v_{\text{freeze,pore}}} \sim \frac{{R_{\text{eff}}}^2 \rho_{\text{i}} L}{k_{\text{i}} \Delta T}. \tag{4.6}$$

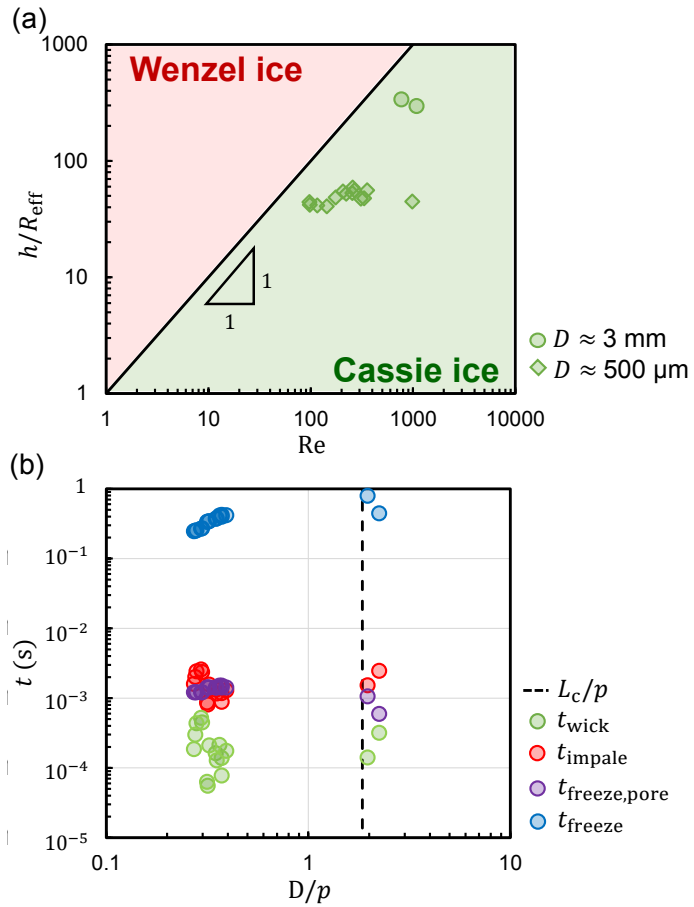

FIGURE 4.4: (a) Phase map comparing when t_{wick} is faster to produce Cassie ice (green shaded region) versus when t_{impale} is faster to enable Wenzel ice (red region). The critical phase line was constructed by equating Eqs. 4.1 and 4.5. All experimental conditions tested (green data points) fell within the Cassie regime. (b) Overview of calculated time scales corresponding to all experimental conditions tested. The vertical dotted line corresponds to when the droplet diameter equals the capillary length ($D = L_c$).

For a typical value of $\Delta T \sim 10°\text{C}$, the pore freezing time scales as $t_{\text{freeze,pore}} \sim 1\,\text{ms}$. Recalling that $t_{\text{wick}} \sim 100\,\mu\text{s}$, we can conclude that the impacting water can indeed wick completely within the frost before the pores can get sealed via freezing. Finally, it was confirmed that preferential lateral spreading along the superhydrophilic frost tips was not a competing arrest mechanism (see Section S6 in Supplemental Materials).

Figure 4.4(a) depicts a phase map comparing when frost wicking versus droplet

impalement is favorable. The critical phase line is found by equating $t_{\text{wick}} \sim t_{\text{impale}}$, resulting in $h/R_{\text{eff}} \sim \text{Re}$ where $\text{Re} = \rho U D/\mu$ is the Reynolds number of the impacting droplet. All data points (green symbols) fall well beneath this phase line, corresponding to the Cassie state (i.e. $t_{\text{wick}} < t_{\text{impale}}$) which agrees with the experimental observation. An analogous phase map was constructed to compare frost wicking versus meniscus freezing, where wicking once again won out across all data points (figure S6). figure 4.4(b) plots all theoretical time scales corresponding to every experimental trial conducted in the freezer (using exact values for ΔT). Across all trials, the calculated wicking time scale was the fastest, further demonstrating the ubiquity of wicking. See figure S7 for additional comparisons of the time scales extended to extreme in-flight conditions (i.e. $U \sim 100\,\text{m/s}$), where wicking similarly wins.

4.3 Conclusions

In summary, we have demonstrated that both frost and ice can be trapped in a suspended Cassie state without resorting to a superhydrophobic surface. Cassie frost was achieved by preferentially condensation frosting the tops of the tall aluminum pillars. Cassie ice was subsequently produced by exploiting the dynamic pressure of impacting droplets to wick the water inside of the porous frost tips. In other words, the water was able to become safely sequestered in the porous frost tips well before it could get impaled between the pillars in the Wenzel state. This wicking mechanism for arresting impacting water in the Cassie state implies that any hydrophilic pillars with porous tips should suffice for producing Cassie ice. However, the benefit of using frost itself as the porous tips is that the mass of the resulting Cassie ice is physically decoupled from the structured substrate itself. This should minimize the ice adhesion strength of the Cassie frost/ice to the underlying hydrophilic substrate to facilitate robust de-icing, which we encourage future works to investigate.

5

Coalescence-Induced Jumping Bubbles during Pool Boiling

5.1 Introduction

Phase-change heat transfer, in particular nucleating boiling, is important for applications such as steam power plants [14], HVAC systems [18], water desalination [19,20], and electronics cooling [15–17]. Many approaches have been considered to increase the maximum possible phase-change heat transfer of nuclete boiling, known as the critical heat flux. In particular, surfaces with micro- and nanostructures [148, 149], biphilic wettability patterns [150], or thermal conductivity patterns [151] have significanly enhanced the critical heat flux. The mechanisms are the enhanced wickability of the liquid phase into the vapor phase and/or limiting the nucleation density of the vapor phase via surface patterns [151–154].

In addition to wickability, it is coming into appreciation that the boiling heat flux also depends on the bubble departure frequency and diameter [155–157]. During pool boiling, surface bubbles typically detach by buoyancy at millimetric scales, such that film boiling can readily form at a moderate critical heat flux [13]. Li et al. recently

showed that a three-tier superhydrophilic surface reduced the bubble departure size to $D_{\text{depart}} \approx 500\,\mu$m, compared to millimeter-scale bubble departures on a smooth copper surface [155]. If a new mechanism could be found to achieve $D_{\text{depart}} \lesssim 100\,\mu$m without resorting to fragile nanoscale surface structures, these works suggest that the critical heat flux of boiling could be substantively increased.

The hydrodynamics of vapor bubbles are analogous to liquid droplets in many ways, particularly at the micro-scale where surface tension effects dominate over buoyancy. In 2009, it was reported that the coalescence-induced jumping of dropwise condensate from a superhydrophobic surface reduced the droplet departure size by orders of magnitude compared to gravitational removal [2]. The enabling mechanism is the release of excess surface energy upon coalescence, which manifests as out-of-plane jumping due to the low-adhesion substrate breaking the symmetry of the expanding liquid bridge [158–160]. The minimum droplet diameter where coalescence-induced jumping was possible ranged from $D_{\text{depart}} \sim 1$–$10\,\mu$m, depending on the geometry of the underlying surface structure which governed the inflation of embryos into large-angle droplets [161–164].

Analogous attempts at removing micrometric surface bubbles via coalescence have been attempted. A purely numerical study determined which range of contact angles enabled the coalescence-induced departure of bubbles from a smooth wall [157]. Two experimental reports utilized isothermal and non-aqueous systems, for example diffusively grown CO_2 bubbles [165] or bubbles of H_2O_2 generated by catalytic decomposition [166]. To date, only one report experimentally observed coalescence-induced bubble departure during aqueous pool boiling (on a micro-pillared surface) [167]; however, it found contradictory results regarding whether the departure velocity decreases or increases with increasing bubble size. They hypothesized a size-dependent Marangoni force to resolve the paradox, but this was not validated.

Here, we reveal two distinct modes of coalescence-enhanced pool boiling that

resolves the apparent paradox of the departure velocity alternately decreasing or increasing with bubble diameter. To obtain clear side-view high-speed microscopy of the hydrodynamics, a quasi-one-dimensional aluminum fin was used to prevent multiple focal planes of bubbles. By machining arrays of micro-cavities and micro-grooves onto the top face of the fin, we promoted the controlled nucleation and early coalescence of vapor bubbles. In comparison to the buoyant departure of a single surface bubble at $D_{\text{depart}} \sim 1\,\text{mm}$, coalescing vapor bubbles readily detached at $D_{\text{depart}} \sim 100\,\mu\text{m}$, an order of magnitude smaller. A scaling model validated that smaller micro-bubbles exhibited a capillary-inertial jumping velocity ($U \propto D^{-1/2}$) upon coalescence, whereas larger micro-bubbles still used coalescence to depin but subsequently departed with a buoyant-inertial velocity ($U \propto D^{+1/2}$). The bimodal hydrodynamics of coalescence-induced departure were observed even for bubbles grown quasi-statically at negligible superheats, demonstrating that Marangoni forces are not responsible.

5.2 Results

Figure. 5.1 is a visual summary of the stark contrast between the buoyancy-induced departure of a single surface bubble versus the coalescence-enhanced departure of two bubbles. The isolated surface bubbles consistently detached at millimetric length scales ($D_{\text{depart}} \sim 1\,\text{mm}$), consistent with previous works (Video S1 in the supporting information) [155]. For bubble nucleation sites sufficiently close together, coalescence-induced departure is possible at micrometric scales ($D_{\text{depart}} \sim 100\,\mu\text{m}$) (Video S1 in the supporting information).

Figure 5.2 shows the experimental setup used to practically control the nucleation and departure of the bubbles. A quasi-one-dimensional aluminum fin ($2\,\text{mm} \times 100\,\text{mm} \times 8\,\text{mm}$) was machined to facilitate the clear side-view imaging of the bubble dynamics. The side walls of the fin were covered by PEEK plastic ($2\,\text{mm} \times 100\,\text{cm} \times 8\,\text{mm}$)

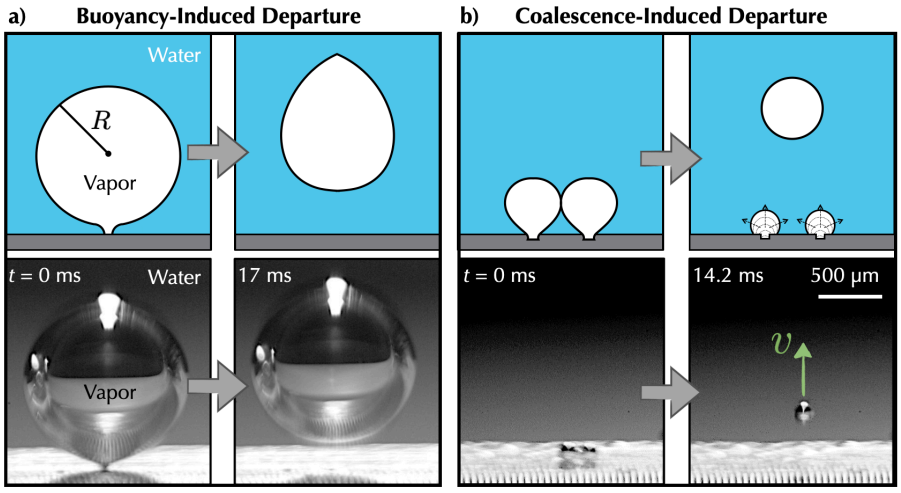

FIGURE 5.1: Two different bubble departure scenario during boiling. For (a), the bubble start to grow from the nucleation site, and after the critical size, the buoyancy is big enough to pinch off the neck between bubble and the surface. For coalescence enhanced departure, (b), two neighboring bubble can coalesce and depart the surfaces before the buoyancy can lift off the bubble which is one order of magnitude smaller size than buoyancy induced departure.

to minimize bubble generation around the fin. A pool of 20 mL of water was contained over the fin using 1.5 mm thick polycarbonate. As shown in the inset of Fig. 5.2, the

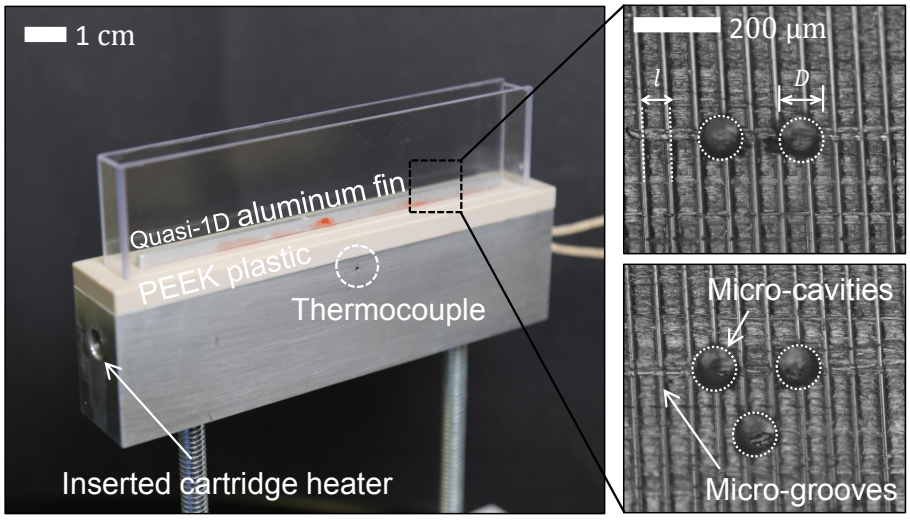

FIGURE 5.2: Experiment set up of quasi-1D boiler. The one dimensional aluminium fin is machined to facilitates clear side-view high-speed imaging of the bubble dynamics. The insets show the micro-cavities/grooves on top of the aluminium fin which is 10 μm length scale.

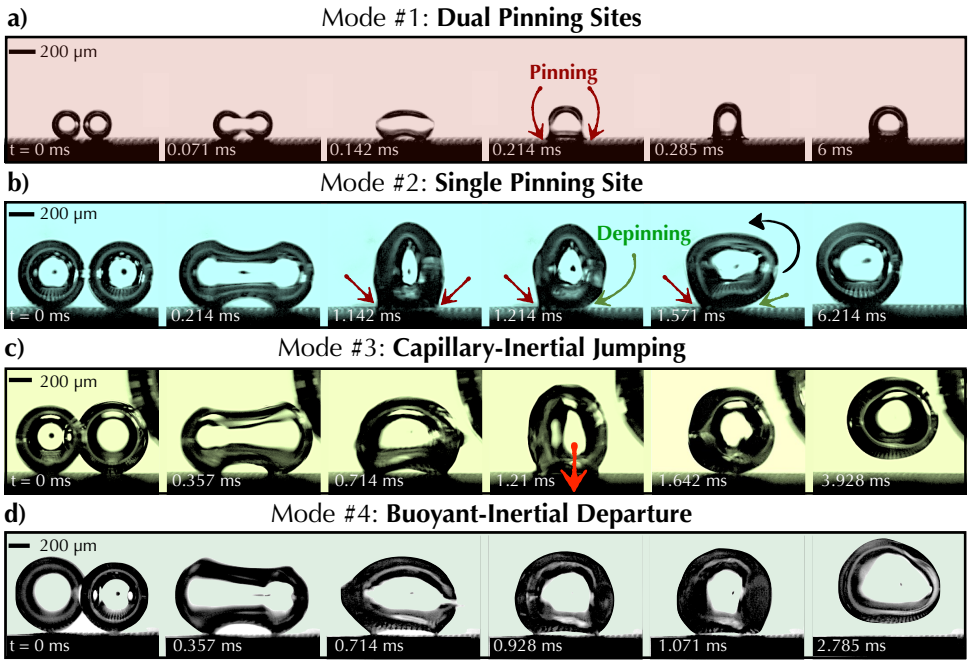

FIGURE 5.3: Four different modes of the bubble coalescence during boiling. (a) when the two bubbles are not big enough, after coalescence, the bubbles are pined on the surface even coalescence with the dual pinning sites. Similar to (a), (b) shows the single pinning site. When the bubble coalescence, just one bubble can depined and spin around toward the other bubble which is still pinned. (c) and (d) are showing the departure of the coalescence bubble. (c) shows the effect of capillarity. In this mode, during coalescence, the bubble neck during coalescence impinges the surface and this pushing can jump the bubble out of the surface. (d) shows the surface tension is only being used to depin the necks, after that the buoyancy can lift off the bubble from the surface.

top face of the aluminum fin featured arrays of close-packed micro-cavities (anything from two holes up to four holes) and lateral arrays of micro-grooves. The holes exhibited diameters of $\approx 80\,\mu$m and a depth of $\approx 25\,\mu$m, whereas the grooves were $\approx 70\,\mu$m in width with a depth of $\approx 10\,\mu$m. Cartridge heaters were embedded in the aluminum to obtain minor superheats ($T_s \approx 100$–$110\,^\circ$) that promoted the quasi-static growth of surface bubbles. The coalescence and departure of bubbles was captured with a high-speed camera (Vision Research, Phantom v711).

Figure 5.3 visualizes the four different modes of bubble coalescence observed during pool boiling on the micro-structures (Video S2 in the supporting information).

(I) Dual Pinning, where the merged bubble retains both pinning sites associated with the two bubbles prior to coalescence. This mode is typical for the smallest bubbles ($D < 100\,\mu$m), as the bubbles have not appreciably inflated relative to their pinning necks at the nucleation sites (i.e., $80\,\mu$m holes or $70\,\mu$m grooves). (II) Single Pinning, where one of the two bubbles depins during coalescence, but the merged bubble retains the other pinning site. This mode is common for mismatched bubbles, where the smaller bubble tends to depin to get pulled into the larger (still pinned) bubble. (III) Capillary-Inertial Jumping, where the substrate breaks the symmetry of the expanding vapor bridge during coalescence. This impingement of the vapor bridge (4th frame in Fig. 5.3c) results in an out-of-plane jumping (6th frame), such that the initial propulsion is powered by capillarity rather than buoyancy. While analogous to the capillary-inertial jumping of micrometric dew droplets on superhydrophobic condensers [2], to our knowledge this is the first explicit side-view imaging of capillary-inertial jumping for micrometric vapor bubbles. This mode was commonly observed for similar-sized bubbles of size $100\,\mu\text{m} < D < 500\,\mu$m (prior to coalescence). (IV) Buoyant-Inertial Departure, where coalescence is merely exploited to detach the bubbles' pinning necks, but it is buoyancy that subsequently lifts the bubble off the surface. This is typical for larger micro-bubbles ($D > 500\,\mu$m prior to coalescence), where the buoyancy is strong enough that the expanding vapor bridge does not appreciably impact the substrate (4th frame in Fig. 5.3d).

Figure. 5.4(a) shows the the bubble departure velocity contrast to the diameter of the merged bubble. If the bubble size of the bubble is too small, the excess surface energy $\Delta G = 4\pi\sigma(R_{\text{m}}^2)$ during coalescence is not big enough to overcome the work done $W_\mu \sim F_\mu R_m \sim \epsilon\mu\sqrt{\sigma/\rho}R_m^{3/2}$ of the bubble against the viscous drag during the expansion and retraction process, where $\epsilon \propto 1/\mu$ is dimensionless amplitude for the viscous damping, μ is the dynamic viscosity of water, ρ is the density of the water

and R_m is the radius of the merged bubble [166]. By equating this the excess surface energy ΔG and the work done by viscous damping W_μ we can put the left vertical line which is around $D_m \sim 0.2\,\mathrm{mm}$. This pinning regime is red shaded regime in fig. 5.4(a) which is corresponding to the the pinning mode in fig. 5.3 (a),(b).

After this critical line, capillary-inertia jumping can happen. In this regime, the capillary energy $E_\gamma \sim \gamma R^2$ is driving the kinetic energy of the merged bubble $E_k \sim \rho_v R^3 U^2$ and this can result in final bubble jumping velocity.

$$U \sim \sqrt{\frac{\gamma}{\rho_v}} R^{-1/2}. \tag{5.1}$$

The green triangle data shows the capillary inertia jumping. The vapor necks impacting the floor and this is flowing the $-1/2$ scaling which goes down the slopes which are shaded as a green color.

Especially, for the small coalescence bubble ($D_{\mathrm{depart}} \approx 200\,\mu\mathrm{m}$) as shown in fig. 5.5, the bubble still can jump of the surface with capillary-inertia jumping even this is not following $-1/2$ power law. This is because the adhesion of the bubble with the surface is too large, so these data points fall off the $-1/2$ line. We colored this regime with the purple area in fig. 5.4(a) between the pinning regime and capillary-inertia jumping regime.

After this capillary-inertia regime, the coalescence is just used to depin the bubble necks, the buoyancy drives the bubble jumping out of the surface which is called buoyancy-inertia departure regime. In this regime, buoyancy energy $E_b \sim \rho_l R^4 g$ is driving the kinetic energy of the merged bubble $E_k \sim \rho_v R^3 U^2$ and this can result in final bubble jumping velocity.

$$U \sim \sqrt{\frac{\rho_l g}{\rho_v}} R^{1/2}. \tag{5.2}$$

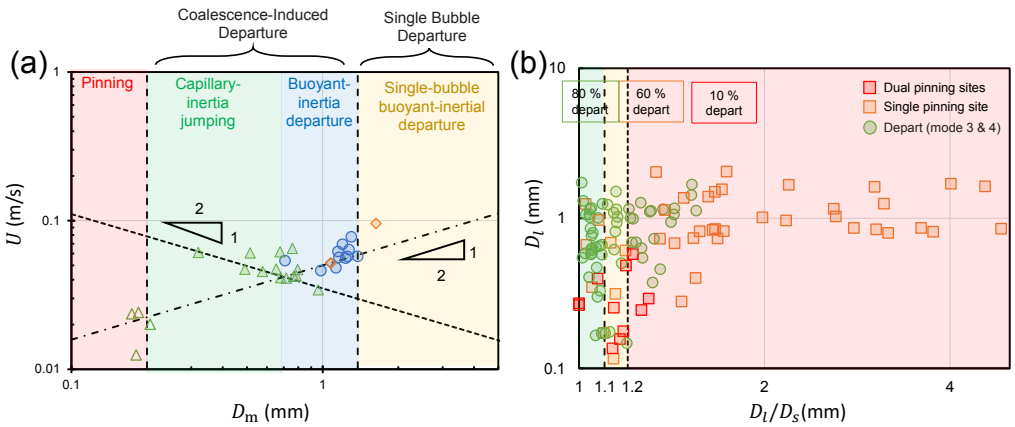

FIGURE 5.4: (a) Phase map of merged bubble size and the departing velocity of the coalescence bubble. There are four different regimes depending on the bubble coalescence. The pinnig regime is showing the pinning on the nucleation site after the coalescence. After that, at some critical diameter of the merged bubble, it shows the capillary-inertia jumping regime where the capillarity of the bubble play a key role of departing with the vapor bubble neck impinge the surface. The capillary-inertia is shifting to the buoyant-inertia departure where the buoyancy us main cause of the departure where the capillarity is just used to pinch off the bubble neck with the surface. For the last regime, the bubble is big enough, so the buoyancy can overcome the adhesion energy of the bubble with the surface where the buoyancy induced departure regime.

The blue circle data (buoyant inertia departure) is following the positive 1/2 as shown in the blue shaded regime.

For the bubble coalescence modes, if the bubble is smaller than the critical size. the bubble can stuck on the surface after the coalescence (red shaded regime). After this regime, capillary inertia jumping (green shaded regime) which is $-1/2$ power law, and then cross over at the x intersection instead of going down the track. It goes up the track on the positive 1/2 buoyant inertia departure (blue shaded regime) and finally crosses over the final line, bubbles way over than this size, it departs even without coalescence, buoyancy enhanced departure (yellow shaded regime). Because of the bubble is large, buoyancy alone is enough to detach the surface without coalescence with the Fritz radius [166] where the buoyancy force ($F_b \sim \rho_l R^3 g$) is balanced with the vertical component of bubble pinning force with the surface

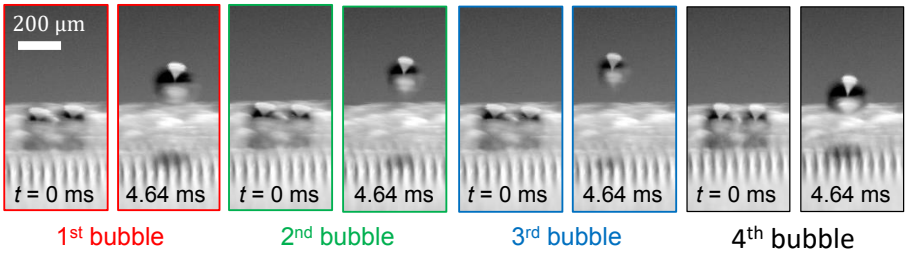

FIGURE 5.5: The multi-cycle bubbles departing from the same nucleation site. The bubble is departing after coalescence and this coalescence induced departure is keep happening at the same nucleation site. In this case, the four times of bubble coalescence departure happened at the same nucleation site.

($F_{\text{pin,verical}} \sim 2\pi R_{\text{p}} sin\theta$) where R_{p} is the radius of the pinning site and θ is the contact angle of water and the surface [166]. In this regime, the yellow diamond data points are corresponding with this buoyancy enhanced departure as shown in Figure. 5.4(a).

Figure. 5.4(b) shows the regime map of the percentage of departing or pinning after the coalescence. When there is a large size mismatch between two bubbles ($D_l/D_s > 1.6$) where D_l is the diameter of of the large bubble and D_s is the diameter of the small bubble, the coalesced bubble can pin on surface without showing any departing as shown in the red shaded are. In the intermediate regime ($1.2 < D_l/D_s < 1.6$), half of the bubble can depart and the other half can pin on the surface. However, for the two bubbles which have small size mismatch ($D_l/D_s < 1.2$), more the 80 percents of bubble can depart the surface not stick on the surface. All of that data at fig. 5.4(a) is constructed from this regime data [166].

Figure. 5.5 shows the multi-cycle bubble generation of coalescence-enhanced departure that is nucleating at the same nucleation site. Bubbles can start to nucleate in the microgroove and coalesce at the small size which leads to depart from the surface (1st bubble). After that, the new bubble keep growing at the same nucleation site and departing the surface with the coalescence (2nd, 3rd and 4th bubble). This multi-cycle bubbles shows the continuous removal of the bubble from the surface

with the coalescence at the same nucleation spot. When each bubbles are departing after coalescence, the bubbles are same size as seen in nucleating bubbles, only variation is due to focal plane during bubble rise.

5.3 Conclusion

In summary, we have shown that microstructures on the one-dimensional aluminum surfaces can promote the controlled bubble nucleation and early coalescence of bubbles departure. The coalescing vapor bubbles detach from the substrate at sizes in an order of magnitude smaller than usual bubble departure. A scaling model reveals two different modes of coalescence-induced departure: capillary-inertial jumping where surface energy can jump off the bubble before buoyancy is dominant and a buoyant-inertial departure where the capillarity is just used to depin the vapor neck, after that the buoyancy can lift off the bubble. Our finding can show a much wider enveloped of departure size of the bubble which can enhance the phase change heat transfer and prevent the onset of film boiling which is not efficient for the phase change heat transfer.

6

Conclusions and Future Work

6.1 Summary and conclusion

As outlined in Chapter 1, the goal of this dissertation is to understand the drop and bubble dynamics which is impacting and departing the surfaces. We accomplished the details of each study in Chapters 2–5. Our observations can be summarized as follows.

In Chapter 2, experimentally and theoretically, we have shown how the raindrop can transmit the disease. Previous research has investigated the disease transmission through the raindrop impact. However, they just focused on disease transmission through the splashed droplet in wet state dispersal. In this chapter, we have focused on the fact that dry spores can spread the disease with the aid of a vortex generated after a raindrop impact. The diseased wheat leaf surfaces and the artificial particles are used to find the dispersal mechanism through the raindrop impact. The result showed that the vortex generated from the drop impact plays a key role because the vortex can help the spore jump beyond the laminar boundary layer, with the potential for long-distance transport.

In Chapter 3, we investigated how the splashed raindrop, after impacting the diseased wheat leaf, can stick on the neighboring healthy plant. To simulate the impacting of the small splashed drops, we have used the hydrophillic mesh to fragmented small satellite droplets. The small fragmented droplet can bounce off the angled superhydrophobic surfaces and move onto an adjacent horizontally oriented wheat leaf. The scaling model shows that depending on the inertia of the droplet, the orientation of the anisotropic leaf surface structure compare to the droplet moving direction and whether the leaf was treated with the fungicide or not, the droplet can stick or bounce off the surface. Our result shows that fungicide treated leaves likely hold liquid droplets more than healthy leaves. Ironically, spreading fungicide could actually promote disease.

In Chapter 4, we have shown the novel technique of trapping air pockets between the frost which is growing on top of the hydrophilic pillars. First, the frost can grow on top of the hydrophobic pillar top due to the high diffusion rate of the sharp corner and non-condensable gas between the pillars. After that, Cassie ice was made with the impacting droplets suspended atop the frost-tipped micropillars before impalement could occur. We found that wicking is the main mechanism that prevents impalement. This is the first demonstration of Cassie ice which does not require any micro-nano structure and hydrophobic chemical coatings have the potential to reduce the ice adhesion.

In Chapter 5, we characterize the bubble coalescence dynamics during the pool boiling. To investigate the detailed bubble dynamics, we engineered micro-structures (micro-cavities/grooves) onto a quasi-one-dimensional metallic substrate to control the bubble nucleation and early coalescence of bubbles. Also the 1D aluminum surface (1 mm wide and 10 cm long) facilitates clear side-view high-speed imaging of the bubble dynamics. Our scaling model shows that there are two different modes of coalescence-induced departure; capillary-inertial jumping at smaller sizes where

vapor neck during coalescence can impinging the surface and help bubble jumping, and a buoyant-inertial departure at larger sizes where capillarity is just used to depin the bubble neck, after that the buoyancy can depart the bubble. Our finding can open up a much wider enveloped of departure size of the bubble which can enhance the phase change heat transfer.

To summarize, in this dissertation, we have highlighted underlying physics and fundamentals of impact of droplets and departure of bubbles which all can be listed under the umbrella of the interfacial fluid dynamics of drop and bubble on various surfaces. The studies presented here are important for not only understanding nature (especially, plant-pathogen), but also the potential industrial applications. As Albert Einstein says, "the important thing is not to stop questioning, curiosity has its own reason for existing.", I have started working on these projects from simple curiosity and it comes out with the final result. I hope the presented work can pique somebody's interest in the future for our better life.

6.2 Future Directions

6.2.1 Observe spores being scavenged by falling droplets.

After the vortex-induced dry dispersal mechanism, we are also interested in the particle scavenging by falling drop. A particle scavenging event by a raindrop involves a lot of complex particle-drop interactions. As a drop falls under gravity, the drop disturbs air flows around it. In the presence of particles (e.g., spores of plant pathogens) in the air, some particles are scavenged by the drop and some particles move around the drop. Previous studies measured the dispersal distance or collision efficiency, which is defined as the fraction of particles swept by a falling droplet. When the collision efficiency becomes one, all particles residing in the swept volume of a droplet are captured in the droplet. In general, three mechanisms of particle capture processes are proposed for the following projects; Brownian diffusion, interception, and

impact. Each mechanism of the collision efficiency strongly depends on particle size, density, wettability, raindrop size, speed, and intensity.

6.2.2 Monitor the splash dispersal of raindrops impacting wet surfaces of wheat and barley plants

Previous rain splash experiments were confined to lab tests only on spore dispersal from wheat cultivars, while the next study will be rain splash experiments include both wheat and barley, systematically vary the plant surface properties (e.g. wetness), and predict spatial distribution and travel distance of droplets/spores under different conditions of wind and relative humidity. In other words, we need to investigate if it is working for real-life conditions and this can give a better understanding of the prediction of wheat production.

6.2.3 Find the best parameter of the aluminum pillars for Cassie ice that can reduce ice adhesion

In this study, simple micro-scale hydrophilic aluminum pillars are used to make the Cassie ice. One of the benefits of trapping air pockets underneath the Cassie frost and ice is that it could minimize ice adhesion to the underlying solid surface. In order to find the best condition for low ice adhesion surface, we need to find the proper surface parameter size. The following work needs to systematically change the surface size (i.e. pitch and diameter of the pillars) which can minimize the ice adhesion. One of the main applications of the Cassie ice is the airplane. If the Cassie ice can build up on the airplane wings, the shear force by wind can easily remove the ice on the airplane wing. So, our basic idea is to measure the actual shear force required to remove the ice sheet on the airplane. Also, we need to investigate if it is working for real-life applications, for example, heat exchangers in freezers, buildings, and power plants. It might be hard to make the Cassie ice in real-life conditions because the Cassie ice really depends on the relative humidity and the air temperature. So,

finding the proper condition for the Cassie ice is another homework for this project. The follow-up work which is presented in the future work includes not only the surface parameter size but also the wind tunnel test could minimize the ice adhesion strength of the Cassie ice to facilitate robust deicing.

6.2.4 Measuring the heat flux of coalescence-induced jumping bubbles on pool boiling

We showed the detailed dynamics of bubble departure with coalescence. The follow-up work needs to measure the heat flux of the surface and check if the coalescence-induced bubble departure can actually increase the heat transfer efficiency. We are assuming the coalescence-induced bubble departure on the microstructure can increase the critical heat flux because of the higher nucleation density with increased nucleation area, but we also need to investigate whether the coalescence can delay the vapor film generation with increased superheat. Maybe the theoretical analysis could estimate the critical heat flux as a function of bubble nucleation density and average departure size is worth it to investigate

Moreover, we just used the working fluid like water, but we also need to check if the same coalescence-induced departure is happening in the other working fluid (other refrigerants). We also need to show a theoretical analysis that could estimate the critical heat flux as a function of bubble nucleation density and average departure size.

The squeezing mechanism was also observed for single bubbles growing within a micro-groove, due to their asymmetric shape and pressure as the top of the bubble protrudes from the groove. We are not sure if this mechanism can increase CHF, but it is worth it to investigate.

Appendix A

Characterizing vortex

A.1 Visualization and measurement of dispersed spores

A.1.1 Measurement of the number and the travel distance of dry spores

We quantified the number and distance of spores dispersed following a single drop impact. First, we placed a piece of an infected leaf inside a petri dish (90 mm diameter). A plastic transparent film containing a spider-web-like pattern was attached to the bottom of the petri dish. This pattern had eight radial lines and four circles in a target pattern (see fig. A.1(a)). The radial lines were split by 45 degrees, and the circles were separated by 10 mm. A single drop was released to target onto the center of the leaf. After a drop impacted the leaf, photos were taken of different regions of the petri dish with a lens of f/7.1 & a 6016×4000 pixel resolution. As shown in fig. 1(e), most of the travel distances of the spores were less than 30 mm. Consequently, our 90-mm petri dish was large enough to contain all dispersed spores after as single drop impact.

Most spores in each grid segment were visible and countable as shown in fig. A.1(b). Consequently, we counted the number and travel distance of spores using ImageJ (since we knew the averaged size of a single spore (~ 5 pixel^2)). A grid segment close to the drop-impact location contained a few hundreds of spores, whereas a far grid segment contained only a few. Due to the high speed of the drop impact, most spores spread and stayed in a single layer on the film. However, we observed a few spore agglomerates on the petri dish, which were lower in number (see fig. A.1(c)). These spore agglomerates could have spores on top, which could lead to an underestimation of the total number of spores. However, we speculate that the spores are not likely to be stacked together due to a low interparticle force (measured in Appendix B).

A.1.2 Microscope images of dispersed wet and dry spores

We observed both wet and dry spores after drop impact. Figure A.2 shows microscopic photos of wet and dry spores on a container. The wet spores were encapsulated, and stayed on the interface of a splashed drop (see the left panel). Due to a capillary force, these spores are aggregated rather than dispersed on the interface (so-called cheerio effect). On the other hand, dry spores are dispersed presumably due to high-speed collisions from an impacting drop (see the right panel).

A.2 Interparticle force of *P. triticina* spores

We estimated the interparticle (or adhesion) force among *P. triticina* spores by measuring the minimum acceleration of a leaf to liberate spores. First, we cut and clamped both ends of an infected leaf. Then, a glass sphere of 1 mm radius was released to impact the leaf sample. Its falling height varied from 3 to 9 cm so that an impact velocity changes from 0.76 to 1.32 m/s. We found that the leaf vibrated and shed rust spores when the impact velocity exceeded 0.9 m/s. Figure A.3(a) shows that airborne spores are shed from a vibrating leaf after the impact. By tracking the motion of the leaf, we were able to calculate the acceleration of the leaf. The critical acceleration for shedding rust spores was observed to be about 150 m^2/s. Then, by multiplying the spore mass, we estimated the interparticle force of spores to be approximately 7×10^{-10} N or 0.7 nN.

A.3 Ejection velocity and angle of dry spores

While an impacting drop spreads and encounters spores, some spores will be captured on a liquid-air interface (the second panel in fig. A.4(a)). Then, the captured spores collide with dry spores in front as the drop spreads further. Eventually, dry spores will be liberated due to the collision (the third panel in fig. A.4(a) and fig. A.4(b)).

To estimate the ejection velocity of dry spores, we made two assumptions; (1) both wet and dry spores have the same mass, and (2) collision between these two types of spores is purely elastic. Under these two assumptions, the ejection velocity of dry spores, V_e, will be the same as the velocity of wet spores. Also, the velocity of wet spores is the same as the velocity of the contact line, V_c because the wet spores are carried by the liquid-air contact line. Thus, V_e can be written as $V_e \approx V_c = dR_c/dt$, where R_c is the spreading radius of the contact line (fig. A.4a). Given the spreading radius $R_c = \sqrt{3U_d R_d t}$ in the early stage [**?**, **?**], we can get

$$\frac{V_e}{U_d} \approx \frac{3}{2}\frac{R_d}{R_e}, \tag{A.1}$$

where R_e is the radial position of spores when ejected ($R_e \approx R_c$). By plotting normalized V_e versus normalized R_e according to our model, we find that dispersed data in figure A.4(c) are collapsed better regardless of particle size, as shown in figure A.4(d). Our theoretical model (a solid line) explains the general trend of the scattered data. One remark is that we neglected the imbibition of water into spores, which may increase the spore size and interparticle friction too. Consequently, the overestimation of our model may be attributed to the ignorance of friction.

A.4 Circulation measurement

We illuminated a vertical plane centered on an impacting drop with a 50 mW continuous laser sheet, 500 μm thick. When particles passed through this laser plane, their trajectories and motions were captured with a high-speed camera at a frame rate of 2,000 to 10,000 Hz with a pixel resolution of 1280 $\times$ 1024. Then, both particle tracking velocimetry (PTV) and particle image velocimetry (PIV) were used to calculate the magnitude of circulation.

In the early stages of particle-dispersal, PTV is better than PIV to extract ballis-

tic trajectories of particles. For the PTV analysis, the Mosaic plugin of ImageJ was adapted to track the motion of liberated particles [**?**], where input parameters were chosen to minimize discontinuities in particle trajectories. Tracked particles over less than 50 frames ($t \leq 10$ msec) were removed to reduce noise in data. After obtaining in-plane particle motions using PTV, we estimated the magnitude of circulation as $\Gamma = (\sum_1^{n_p} V_p \, 2\pi r_p)/n_p$ where n_p and V_p are the number and velocity of particles, and r_p is the distance between a particle and the vortex center. This is an approximate form of an exact expression: $\Gamma = \oint_C U_w dl$, where C, l, and U_w are the closed curve, length, and the air velocity, respectively.

For the PIV analysis, the open-source PIVlab software was used to obtain air flow velocity fields in the early stage of particle-dispersal. The high-speed videos were analyzed with a 64×64 interrogation size at 50% overlap. Suspicious velocity vectors (likely due to background noise) were removed, when the number of erroneous vectors was below 5% among the total number of velocity vectors. Then we obtained $\Gamma(t)$ at different conditions.

A.5 Maximum spreading radius and average speed of a liquid contact line

A.5.1 Maximum spreading radius, R_m

To estimate the maximum spreading radius, R_m, of a drop on a surface with particles, we used a previous theory developed for the maximum radius on a non-particulate smooth surface. Especially, for $We_d \gg \sqrt{Re_d}$, the maximum spreading radius on a smooth surface can be expressed as [**?**],

$$R_m \approx (1/2) R_d Re_d^{1/4}, \tag{A.2}$$

where the Reynolds number is defined as $Re_d = \rho_d U_d (2R_d)/\mu_d$. Because the thickness of a particle layer is sufficiently thin, we used the above expression for our

experimental surfaces. We found that experimentally measured R_m on particulate surfaces is close to eq. (A.2), especially with thin particle layers ($\leq 100 - 250$ μm) (see figure A.5).

A.5.2 Average speed of a liquid contact line, $\bar{U}_c$

The average speed of a liquid contact line, $\bar{U}_c$, is approximated as R_m/t_m, where t_m is the time duration for a spreading drop to reach its maximum radius, R_m. The spreading time t_m scales as R_d/U_d as in [**?**]. Finally, we obtained the mean velocity as $\bar{U}_c \sim (R_m/R_d)U_d$.

A.6 Simulation of spore trajectories

We simulated the spore trajectories by solving the equation of motion considering inertial force, air drag force, and gravitational force, as mentioned in the main text;

$$\rho_s \left(\frac{4}{3}\pi r_s^3\right) \frac{d\vec{V}_s}{dt} = 6\pi\mu_a r_s(\vec{V}_s - \vec{U}_w) - \rho_s \left(\frac{4}{3}\pi r_s^3\right) \vec{g}. \tag{A.3}$$

To estimate $\vec{U}_w$, we used potential theory and the method of image force in order to mimic an air vortex ring near the wall. We placed one vortex and one image vortex across the wall, which ensured no normal velocity along the wall. The corresponding complex potential W can be written as $W = -\mathrm{i}\Gamma/(2\pi)\log\left[(z-d_1)/(z-d_2)\right]$ [**?**], where z is a complex variable of a position and d_1, d_2 are complex variables representing the central positions of the vortices. We observed that the circulation, Γ, decays over time (fig. A.6), and the central position of the vortex moves (fig. A.7).

A.6.1 Dissipation of circulation, $\Gamma(t)$

To obtain an analytical expression of $\Gamma(t)$, we include a dissipation term by assuming circulation exponentially decaying in time, $\Gamma(t) = \Gamma_0\, e^{-t/\tau_v}$. Here, Γ_0 is the

initial magnitude of circulation and $\tau_v = CR_d^2/\nu_a$ is the viscous time scale where C is an undetermined coefficient. After we obtain the detailed profile of $\Gamma(t)$ from experiments, Γ_0 and C are determined from a best fit to experimental data, as shown in figure A.6 (R-square value of the fitting curve= 0.89). Finally, we get $\Gamma_0 = 0.14 Re_a^{-1/4} Re_d^{3/8} U_d R_d$ and $C = 0.3$.

To clarify the difference between $\Gamma(t \approx 0)$ and Γ_0, $\Gamma(t \approx 0)$ (data marked with the red arrow in fig. A.6) is a measured value from PTV data, whereas Γ_0 is a fitted value based on the above exponential decay relation (marked as the red dotted circle at $t = 0$). This Γ_0 was used in simulations for particle trajectories as shown in Fig. 5.

A.6.2 Movement of a vortex

We denote a complex-variable position of the vortex as d_1 and its image vortex as d_2. Since the wall is at $x + i\,0$, d_1 and d_2 can be expressed as $R_w(t)+\mathrm{i}H_w(t)$ and $R_w(t)-\mathrm{i}H_w(t)$, respectively. Here, R_w and H_w are the radial and vertical positions of the vortex, as denoted in figure A.7(a). We visualized and measured the center position of the vortex by using a smoke generator (ChauvetDJ H700).

Figure A.7(b) shows that $R_w(t \approx 0)$ strongly depends on R_d but not on U_d. Here, $R_w(t \approx 0)$ is close to $R_m(\sim R_d^{5/4} U_d^{1/4})$, since the vortex was formed when a drop reached its maximum spreading radius. Figure A.7(b) also shows the movement of both horizontal and vertical positions of the vortex (R_w & H_w). R_w & H_w slightly increased over time at speeds of $\dot{R}_w$ & $\dot{H}_w$, respectively. The Péclet number $Pe = \dot{R}_w R_d/\nu_a$, defined as the ratio of inertia to viscous diffusion, was measured to be on the order of 0.1 except for the early stage. Also, we observed that the velocity of vortex center was independent of R_d and U_d, which indicated that the inertial effect is negligible compared to the viscous force. Hence, we can assume that an air vortex disperses due to the viscous diffusion. Thus, we anticipate that $R_w \sim$

$\sqrt{\nu_a(t-t_m)}+R_m$ and $H_w \sim \sqrt{\nu_a(t-t_m)}$ where ν_a is the kinematic viscosity of air. In general, the time for a spreading drop to reach its maximum radius, t_m (on the order of 1 ms) is much less than the typical time scale of the moving vortex (on the order of 100 ms). Therefore, $t-t_m \approx t$, which yields the following simple association:

$$R_w - R_m \sim \sqrt{\nu_a t} \text{ and } H_w \sim \sqrt{\nu_a t}. \tag{A.4}$$

Figure A.7(c) shows $R_w - R_m$ and H_w versus time to confirm our model above. The slopes of both $R_w - R_m$ and H_w in the log-log plot are close to 1/2 as our model predicted. Also, the similar slopes of both horizontal and vertical positions indicate that an air vortex moves along the 45 degree line from the edge of a spreading drop (see the dotted line and vortex core in fig. A.7(a)). It shows that the movement of the vortex is primarily caused by the diffusing viscous boundary layer of the air vortex as our model assumed.

A.6.3 Rust spore trajectories

Figure A.8 shows that both experimental and theoretical trajectories exhibit longer travel distances than those from spores without an air vortex. However, some discrepancy was observed between experiments and theoretical predictions, especially near the end of the spore trajectories. This could be due to different R_m on superhydrophobic leaf surfaces, and/or an additional air flow induced by the movement of splash droplets along the leaf surface.

A.7 Stokes number of spores of different leaf rusts infecting different commercial crops

Figure A.9 shows the Stokes number for different leaf rusts infecting different commercial crops. Since the Stokes numbers are less than 1, the spores of these rusts are likely dispersed by air vortices from raindrop impacts.

Table A.1: Contact angles of natural and artificial wheat leaves.

Substrate	θ_A	θ_E	θ_R
1. Healthy wheat leaf	124±3°	115±10°	113±4°
2. Infected wheat leaf	148±3°	145±7°	132±5°
3. PC film	93±3°	86±7°	59±2°
4. SCPC film	156±2°	154±3°	149±4°

A.8 Spore density measurement

We estimated the density, ρ_s, of *P. triticina* spores from a terminal velocity. We prepared an acrylic bath with a dimension of $20 \times 20 \times 10$ cm, where we made a narrow slit opening with 20×1 cm. Then we released a small amount of *P. triticina* spores through the slit. By measuring the terminal velocity v_t of individually falling spores, we estimated the density ρ_s using the Stokes relation as $\rho_s = 2\mu_a v_t/(2gr_s^2)$ where $\mu_a = 1.82 \times 10^{-5}$ Pa·s and $g = 9.81$ m/s^2. The calculated spore density was 1294 ± 84 kg/m^3 (based on 5 experimental trials). Our density value is close to the density of other naturally observed fungal spores [**?**] and pollen [**?**].

A.9 Contact angle of natural and artificial wheat leaves

Table A.1 shows that the advancing angle θ_A, equilibrium angle θ_E, and receding angle θ_R of healthy leaves, infected wheat leaves, and artificial leaves (polycarbonate (PC) and spray-coated polycarbonate (SCPC) films). Contact angles were measured using the sessile drop method by taking side-view photos with a single droplet on each substrate. By pumping or sucking water into or out of a drop, we were able to measure the advancing and receding angles near the triple contact point. It is worth noting that although an air vortex is formed on both PC and SCPC films, experiments with PC films were primarily used for measuring circulation & trajectories because drop-impact experiments on SCPS films create many splash droplets distorting the shape and magnitude of an air vortex.

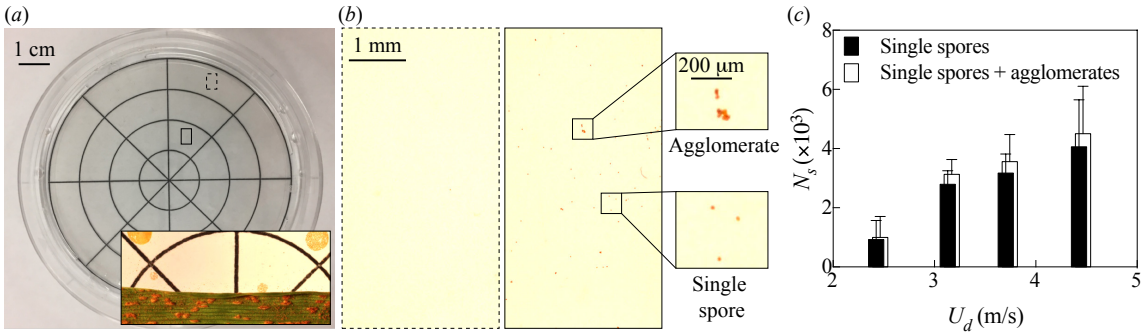

FIGURE A.1: (a) Petri dish dispersal device to measure the number and travel distance of dry-dispersed rust spores. The inset shows the actual trial after drop impact. (b) After a drop impacts the leaf with $[R_d, U_d]$=[1.8 mm, 4.4 m/s], photos of dispersed spores were taken to count the number of spores from two sample regions marked in (a). (c) Histogram of showing the numbers of individual spores and agglomerates depending on an impact velocity with $R_d = 1.8$ mm.

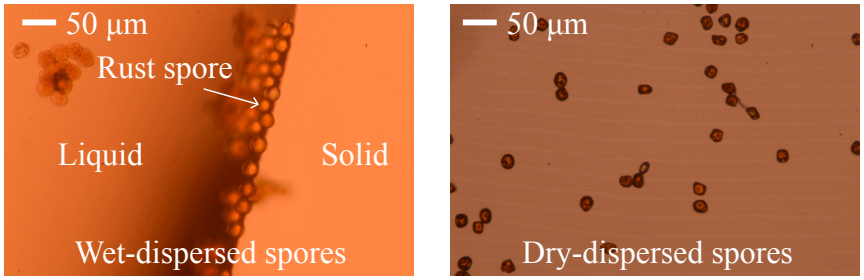

FIGURE A.2: Left and right panels show microscope images of wet-dispersed and dry-dispersed spores, respectively.

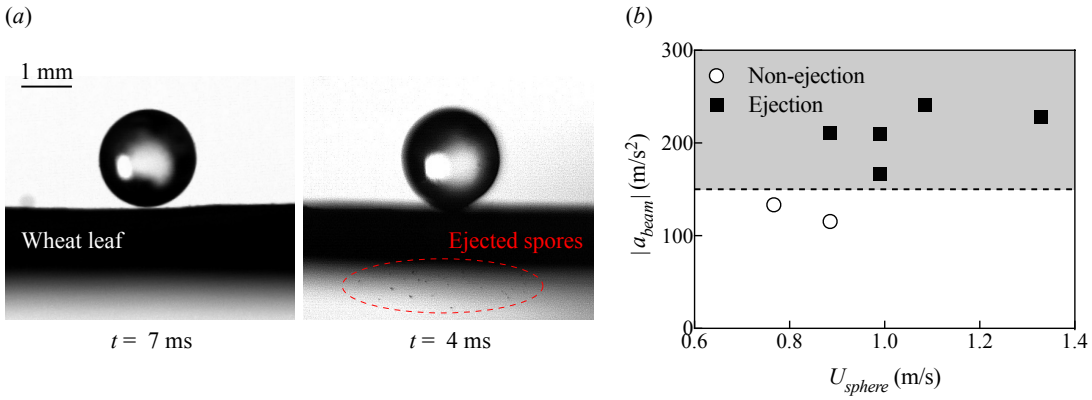

FIGURE A.3: (a) A glass sphere impacts an infected wheat leaf. Impact velocity was 0.8 m/s on the left panel and 1.1 m/s on the right panel. The red dashed circle shows a region where rust spores are liberated due to the impact. (b) Acceleration of a leaf, $|a_{beam}|$, versus impact velocity of a glass sphere, U_{sphere}, where a critical acceleration for the spore ejection was measured to be about 150 m^2/s.

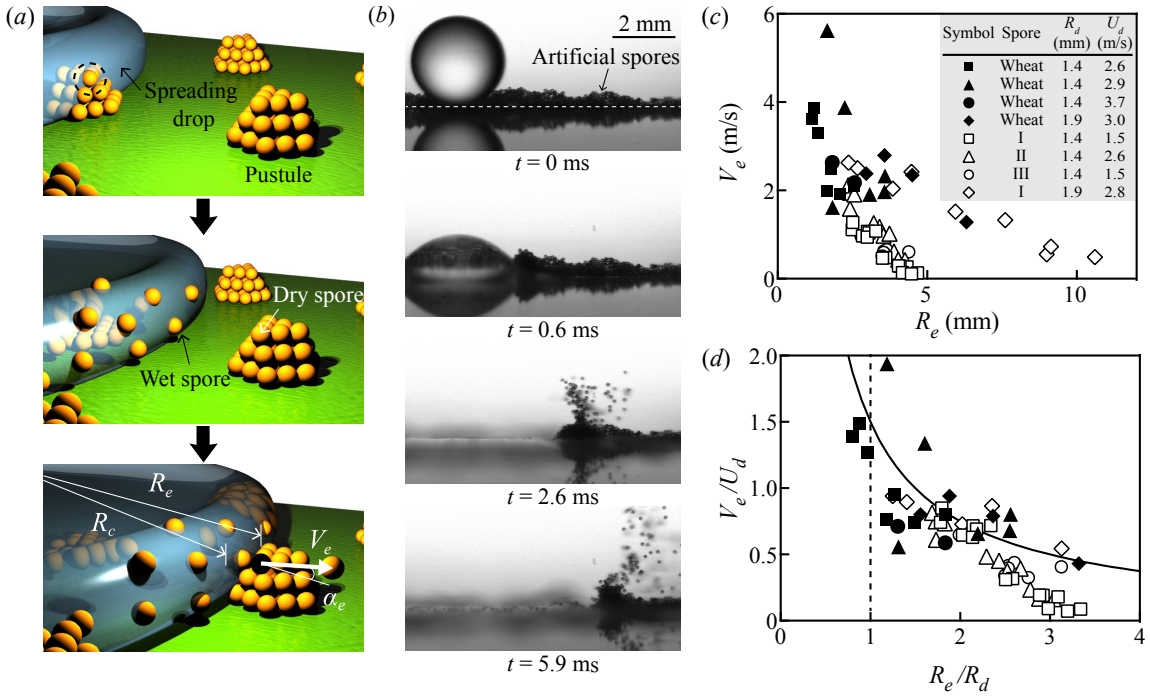

FIGURE A.4: (a) Schematics of spore-ejection mechanisms. When a drop spreads and encounters spores, the spores will be detached and captured in a liquid-air meniscus (top panel). Then, the front of the liquid containing the spores spreads and collides with additional spores (middle panel). Due to the collision, dry spores are liberated from the leaf at an ejection speed, V_e (bottom panel). (b) Image sequences of ejected glass beads III on a PC film at $[R_d, U_d]$=[1.5 mm, 3.0 m/s]. (c) Ejection velocity of spores V_e versus ejection radial position R_e. (d) Plot of dimensionless ejection velocity vs dimensionless ejection radial position. Our model of Eq. (A.1) is plotted in a solid line.

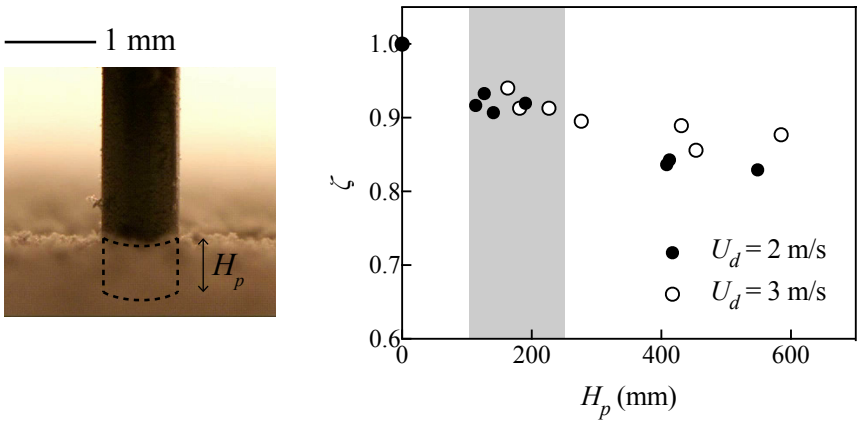

FIGURE A.5: Image of our method to measure the particle thickness H_p (left panel). A thin rod (shown as a black cylinder) was lowered using a linear stage to determine the depth of a particulate layer. The ratio of experimental R_m on a particulate surface to theoretical R_m on a smooth surface, ζ, versus the thickness of a particulate layer, H_p (right panel). The gray region corresponds to the range of H_p from wheat leaves in used in our experiments.

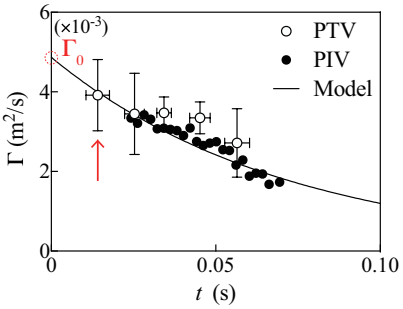

FIGURE A.6: Circulation between experiments and our model (a solid line) when $[R_d, U_d]$=[1.9 mm, 3.1 m/s].

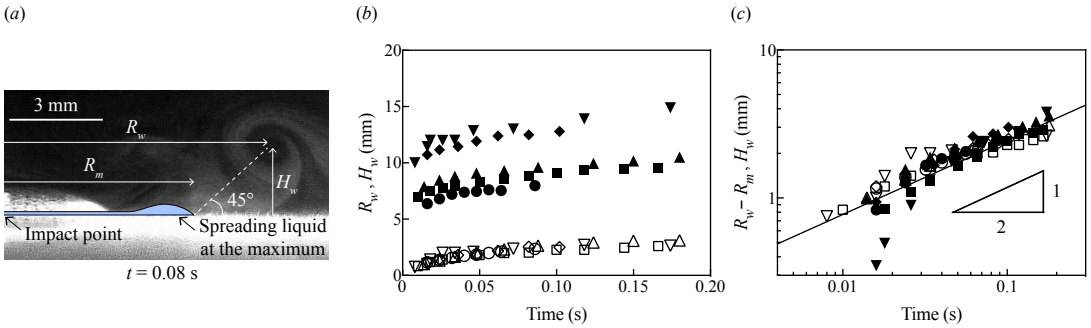

FIGURE A.7: (a) Visualization of a vortex using a smoke generator (b) Linear and (c) loglog plots of experimentally measured R_w and H_w versus time, where closed and open symbols correspond to R_w and H_w, respectively. Different symbol shapes represent different experimental conditions (∅: [R_d, U_d]=[1.4 mm, 2.2 m/s], □: [R_d, U_d]=[1.4 mm, 3.2 m/s], △: [R_d, U_d]=[1.4 mm, 3.9 m/s], ♢: [R_d, U_d]=[1.9 mm, 3.2 m/s], ▽: [R_d, U_d]=[1.9 mm, 4.0 m/s])

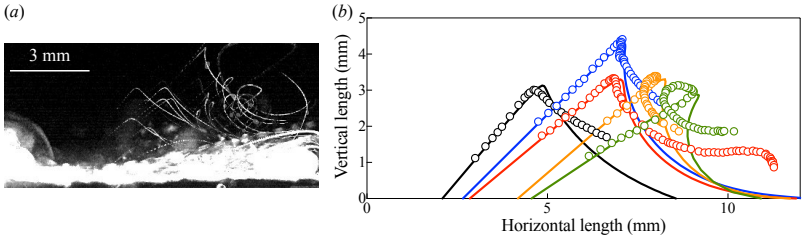

FIGURE A.8: Footprint of rust spores when [R_d, U_d]=[1.9 mm, 3.0 m/s]. (a) Overlapping image (from t = 0.8 to 100.8 ms). (b) Comparison between experiments (circles) and simulated trajectories (solid curves)

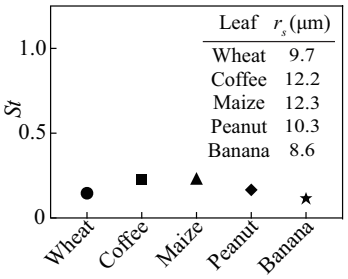

FIGURE A.9: Expected Stokes numbers for spores of different leaf rusts infecting different commercial crops. Given that the Stokes numbers are similar, it is likely that spores of many different leaf rusts have the potential to be dispersed by air vortices from raindrop impacts. The inset shows the radius of urediniospores depending on different crops, where the radii of coffee, maize, peanut, and banana leaf rusts were obtained by averaging the half-length and -width of the spores.

Appendix B

Characterizing wheatbounce

B.1 Measuring the size of sprayed fungicide droplets

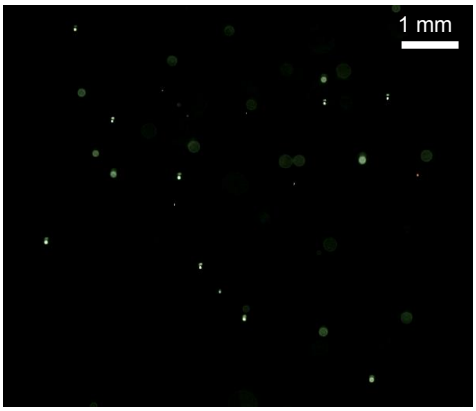

FIGURE B.1: Photograph of airborne droplets containing the fungicide solution. The characteristic droplet diameter was approximately 70–100 μm.

B.2 Measuring the size of splashed satellite droplets.

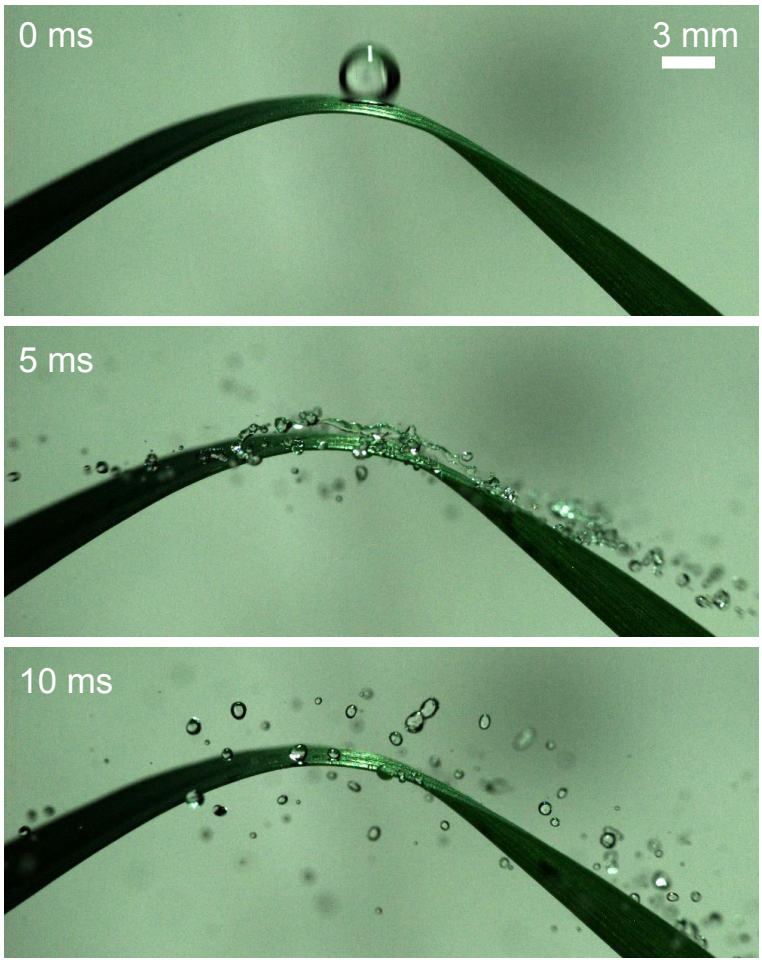

FIGURE B.2: Side-view of high-speed photography of a 2.88 mm diameter droplet impacting a wheat leaf at a speed of $U_i = 6\,\mathrm{m/s}$. This impact speed mimics that of real raindrops (4–10 m/s). The resulting splash produced satellite droplets whose diameter is in the range of $D \approx 500$–$1{,}000\,\mu\mathrm{m}$. This was used as a guideline when choosing the wire mesh used to generate satellite droplets for the results shown in the main manuscript. By using a mesh to generate satellite droplets, the mother droplet could be released much closer to the surface for more controlled experimentation.

B.3 SEM images of untreated and fungicide sprayed leaves

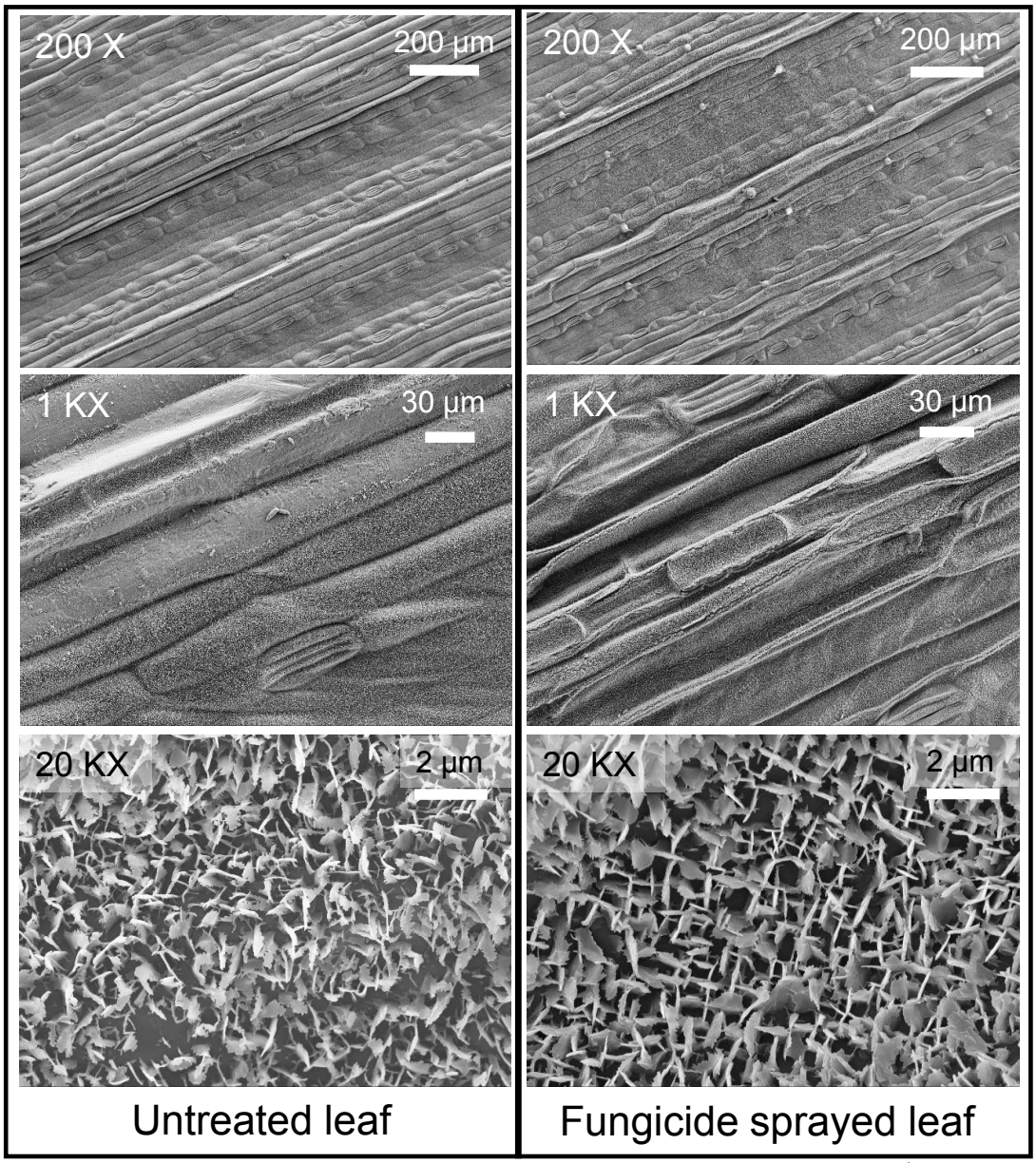

FIGURE B.3: Scanning electron micrographs of untreated wheat leaves (left images) versus leaves sprayed with fungicide (right images). Three different magnifications were used to show that the fungicide spray did not appreciably alter the leaf morphology.

B.4 Static and dynamic contact angle measurements

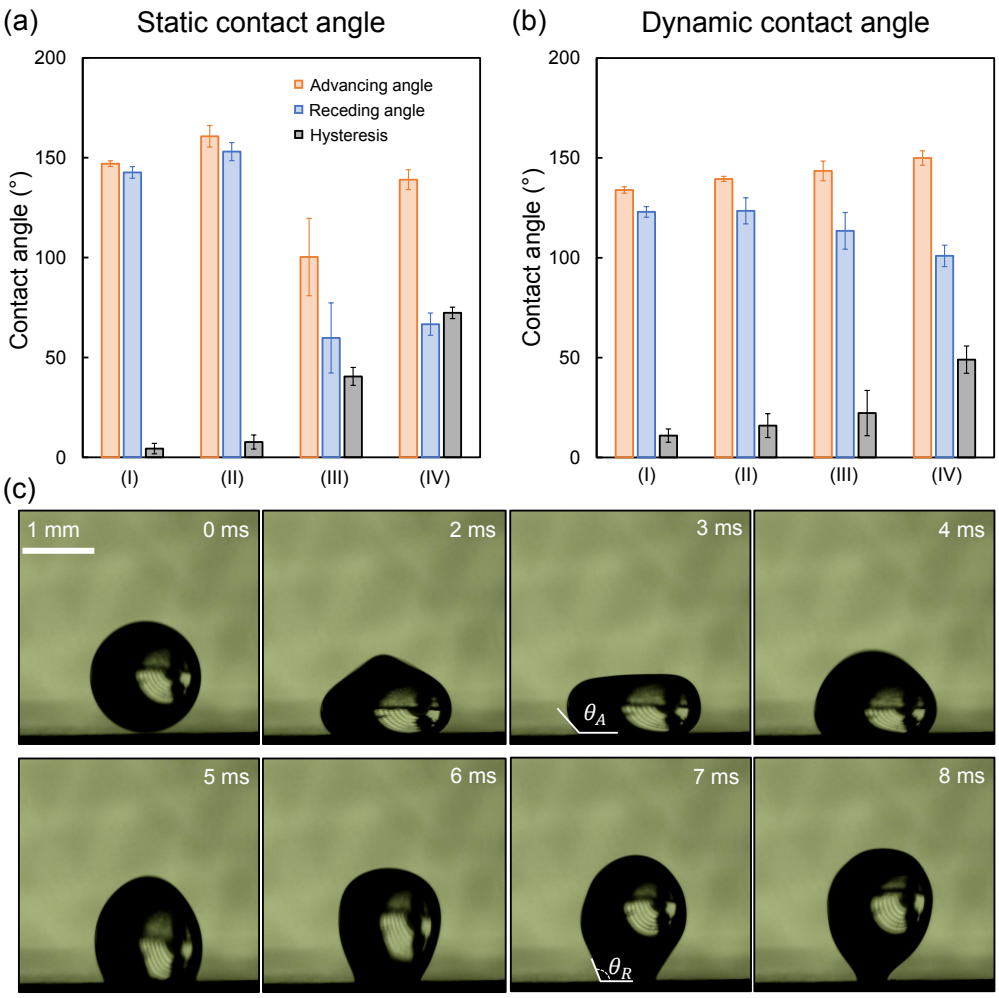

FIGURE B.4: **(a)** The same advancing and receding apparent contact angles as shown in Figure 2b, now compared to **(b)** the contact angles of dynamic droplets. The dynamic contact angles were obtained by using side-view high-speed imaging and measuring the advancing angles during droplet impact and the receding angles during droplet retraction. **(c)** Time-lapse images of a droplet impacting an untreated leaf surface. The contact angles of the dynamic droplet were measured with $[D_\mathrm{d}, U_\mathrm{d}] = [1.2\ \mathrm{mm}, 0.6\ \mathrm{m/s}]$ where D_d, U_d are the diameter and velocity of an impacting drop, respectively. The advancing contact angle was measured when the droplet almost reached the maximum spreading diameter(see 3 ms) and the receding angle was measured when the droplet started to recede (see 7 ms).

B.5 Contact angle hysteresis of static versus dynamics droplets.

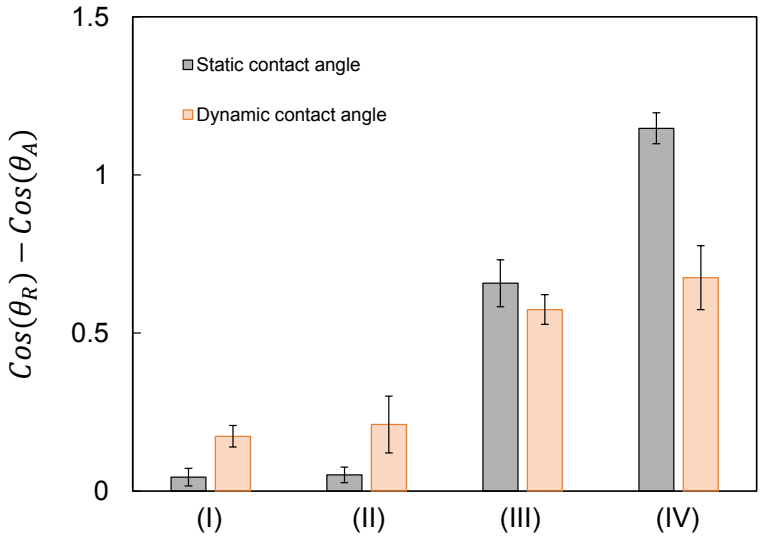

FIGURE B.5: Comparison of the contact angle hysteresis of static versus dynamics droplets. For untreated leaves (I and II), the hysteresis was markedly higher for impacting droplets, indicating a partial wetting transition. Therefore, the dynamic angles were used to estimate the pinning force for the bouncing versus sticking model. For the fungicide sprayed leaf with parallel ridges (III), the static and dynamic values were the same within uncertainty. This demonstrates that the hysteresis of the sprayed leaf is primarily due to its chemical deposits, as opposed to an impact-induced wetting transition. Therefore, the static angles were used for (III) for the model, as the swell-shrink method is a more accurate means of contact angle measurement than the dynamic method. Finally, no bouncing was observed for leaf type (IV), so the contact angles were not directly used in the model. We expect the reduction in hysteresis for the dynamic case compared to the static case is not physical. The disparity is more likely due to random variations in leaf samples and fungicide spray conditions.

Appendix C

Characterizing cassieice

C.1 Experimental Section

A 10×10 array of pillars were machined into the top face of a $2.5\,\text{cm} \times 2.5\,\text{cm} \times 3.175$ mm sheet of 6061 aluminum. Each pillar exhibited a width of $w = 0.5\,\text{mm}$, height of $h = 1\,\text{mm}$, and edge-to-edge pitch of $p = 1.5\,\text{mm}$ as shown in Fig. SC.1 a,b. The sample was then degreased by successively submerging in acetone, isopropyl alcohol, and water, followed by drying with nitrogen gas.

For the frost generation, the bottom of the micropillared substrate was thermally bonded to a Peltier stage (ráme-hart, 100-30) using a thin film of thermal grease (Thermalcote, 251G). The Peltier stage was then cooled down to a chilled temperature ranging from $T_\text{w} = -7^\circ$ to $-40\,^\circ\text{C}$. Side-view imaging of the growing frost was recorded using a DSLR camera (Canon, EOS 5D Mark IV) with $2\times$ lens (Venus Optics Laowa 60 mm f/2.8 2X UltraMacro Lens). The duration of frost growth was anywhere from 5 min to 120 min, depending on the environmental conditions and supersaturation (cf. Fig. SC.2), to achieve a millimetric thickness to the frost tips sufficient for the subsequent droplet impact experiments

After the frost was grown, the impact of falling droplets was observed using high-speed imaging (Phantom v711). The ambient conditions were either room temperature (Fig. 2a) or isothermally chilled in a walk-in freezer (Fig. 2b). The walk-in freezer was located in the Food Science Building at Virginia Tech where $T_\infty \approx$ –22 – –13,°C. The pipetter was initially filled with water in the docking room, and then brought into the walk-in freezer and released over the sample before the (now supercooled) water had sufficient time to freeze over. The impact speed was measured by the high-speed camera and ranged from $V_i = 0.8$–$1.4\,\text{m/s}$. To generate microdroplets (500–1000 µm diameters), a hydrophillic mesh (9219T874, McMaster Carr) was used. Impact events were typically captured from an isometric perspective, i.e. 45° downward angle with respect to the horizontal.

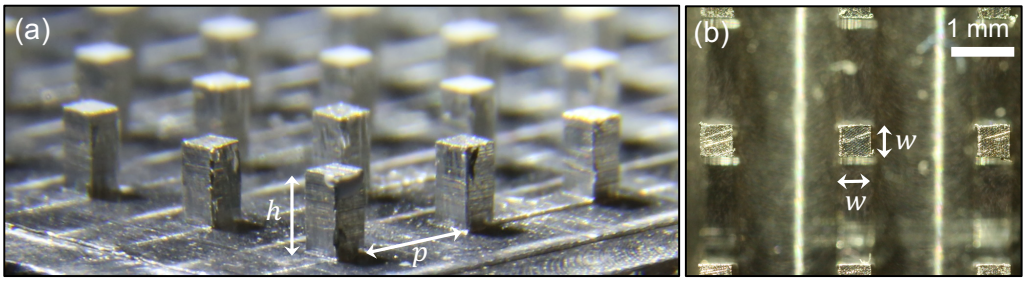

FIGURE C.1: (a,b) Photographs of the array of hydrophilic aluminum pillars, where each square pillar exhibits a width of $w = 0.5\,\text{mm}$, height $h = 1\,\text{mm}$, and edge-to-edge pitch of $p = 1.5\,\text{mm}$.

C.2 Frost Growth and Numerical Simulations

The upward frost growth from the pillar tops was radial for $S = 15$ (Fig. S2(a)) but more column-like for $S = 1.5$ (Fig. S2(b)). This disparity in frost shape was rationalized by a simple numerical simulation to calculate the concentration field for water vapor after the first formation of frost atop the pillars. The simulations were solved by imposing a boundary condition of $c_\mathrm{i} = P_\mathrm{i}/(RT_\mathrm{w})$ atop the pillars, where c_i and P_i are the saturated concentration and pressure of ice at temperature T_w, respectively, and R is the gas constant. Values for $P_\mathrm{i}(T_\mathrm{w})$ were obtained from a report by Murphy and Koop [139]. A second boundary condition of $c_\infty = P_\infty/(RT_\infty)$ was defined along the top of the concentration boundary layer, which was given an effective thickness of $\zeta \sim 1\,\mathrm{cm}$ [33, 137, 138] with respect to the floor of the micropillared substrate. The quasi-steady concentration field was then calculated by solving the Laplace equation, $\nabla^2 c = 0$. For the case corresponding to $S = 15$, only the pillar tops themselves were subsaturated with respect to liquid water, which explains the radial growth of the frost tips from the intermediate air space Fig. S2(c). Conversely, for $S = 1.5$, the gaps between frost-tipped pillars were also subsaturated, such that the vapor mostly diffused to the frost tips from above Fig. S2(d).

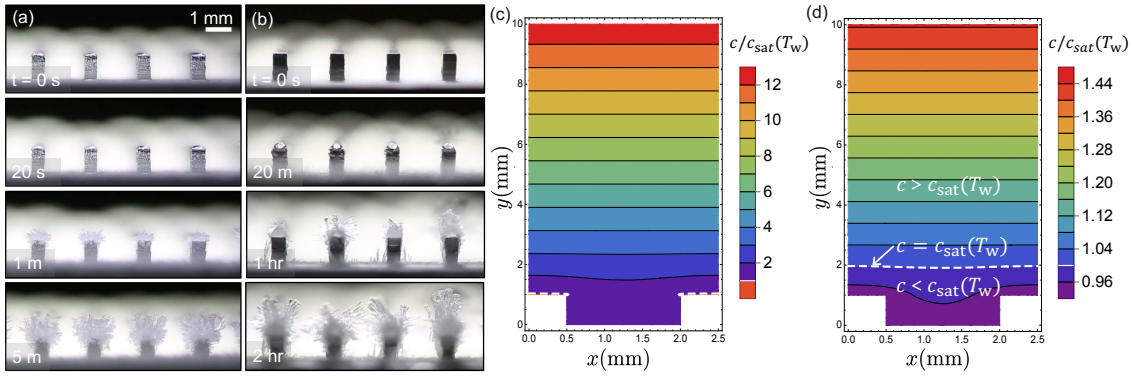

FIGURE C.2: Side-view optical microscopy of frost growth on the aluminum micropillar array. The frost was grown under two different conditions: (a) $T_w = -20\,°C$, $T_\infty = 22\,°C$, and $RH = 71.5\%$ (resulting in a supersaturation of $S = 15$) and (b) $T_w = -7\,°C$, $T_\infty = 3.2\,°C$, and $RH = 73.6\%$ ($S = 1.5$). (c,d) Numerical simulations of the quasi-steady concentration field for water vapor after the first formation of frost atop a unit cell of pillars, for (c) $S = 15$ and (d) $S = 1.5$. The color grid represents the ratio of the local concentration to the saturation concentration corresponding to the substrate temperature: $c/c_{sat}(T_w)$. Subsaturated regions, where $c/c_{sat} < 1$, are bounded by white dotted lines.

C.3 Visualizing dry zones

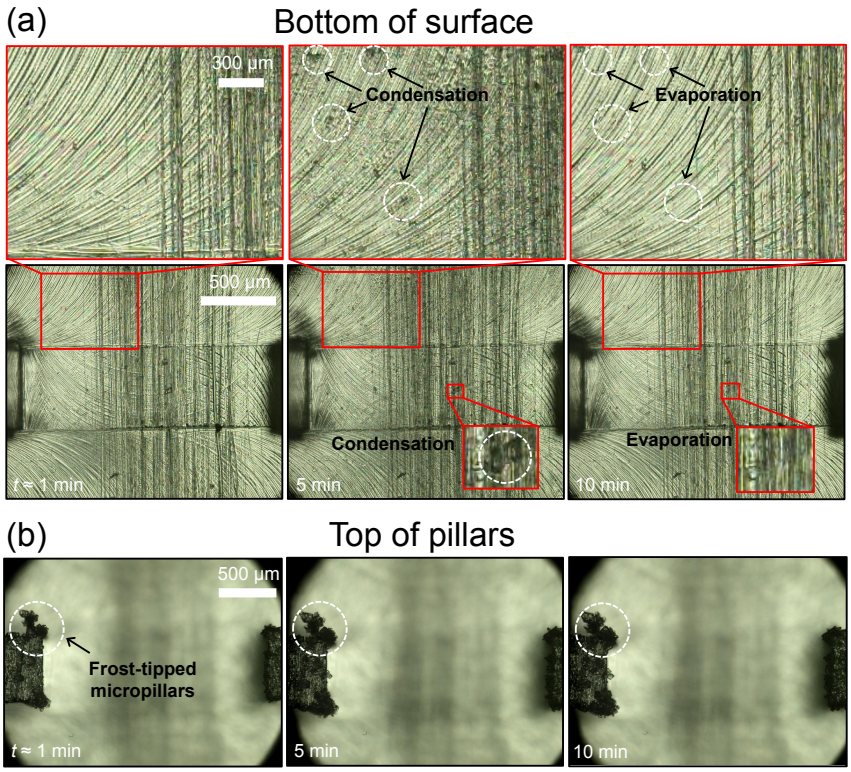

FIGURE C.3: Top-down micrographs showing the formation of a dry zone on the bottom floor between micropillars. The conditions were $T_w = -10\,°C$, $T_\infty = 18\,°C$, and RH = 17%, resulting in a supersaturation of $S = 1.2$. (a) Images with focal plane at the bottom floor between the micropillars. At $t = 0$ min, the surface has just begun to cool down toward $T_w = -10\,°C$ and is still above the dew point. At $t \approx 5$ min, the surface temperature has stabilized at $T_w \approx -10\,°C$ and condensation sparsely nucleates on the floor of the surface (white circles added to magnified insets to help visualize their locations). By $t \approx 10$ min, the hygroscopic frost that has already formed on top of the micropillars has evaporated these bottom droplets to form a dry zone. (b) Equivalent photographs with the focal plane shifted to the tops of the micropillars. By $t \approx 1$ min, condensation preferentially growing on the pillars tops had already frozen into frost (white circle added for visualization). Over the next several minutes, this frost continued to grow from harvesting the lower supercooled condensate and also from the supersaturated ambient.

C.4 Small droplet impacts

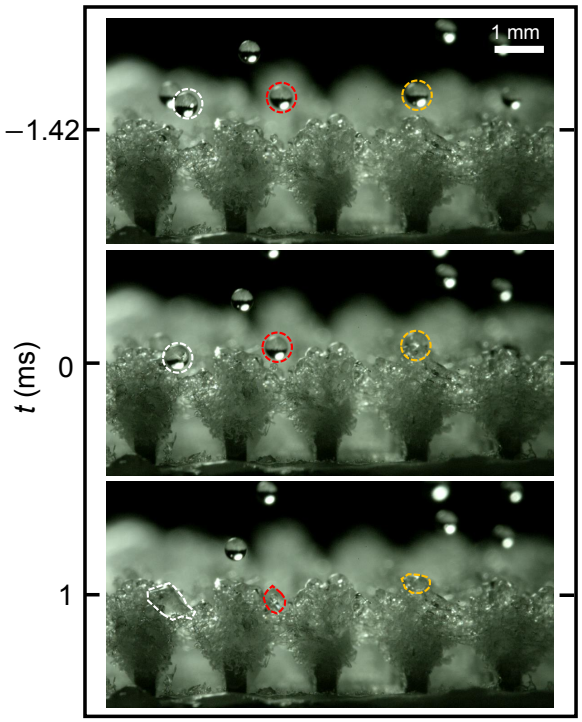

FIGURE C.4: Side-view high-speed photography of microdroplets ($D \approx 500$–$1{,}000\,\mu\text{m}$) impacting frost-tipped pillars to form Cassie ice. Three microdroplets (outlined for visibility) all impacted the frost tips at the same moment ($t = 0$ms middle frame) and became arrested in the Cassie state within $t = 1$ ms (bottom frame).

C.5 Cassie ice

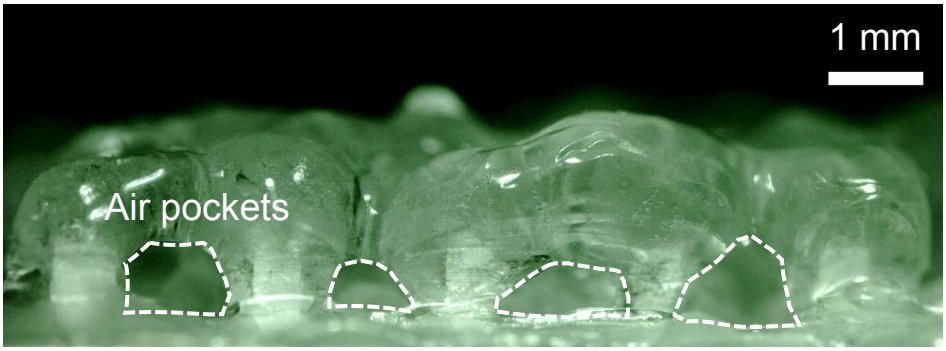

FIGURE C.5: Side-view high-speed photography of microdroplets ($D \approx 500$–$1{,}000\,\mu m$) impacting frost-tipped pillars to form Cassie ice (see Video S4 in the Supporting Information). After approximately 20 millimetric droplets were impacted into the mesh to spray the surface with microdroplets, the final result was a thick sheet of frost/ice trapped in the Cassie state (air pockets outlined for visibility)

C.6 Spreading time scale

Another possibility for the arrest mechanism is the preferential lateral spreading of the droplet along the frost tips. Assuming a capillary-inertial spreading regime, the spreading time scales as:

$$t_{\text{spread}} \sim \sqrt{\frac{\rho}{\gamma h}} R^2 \tag{C.1}$$

where $\rho \approx 1000\,\text{kg/m}^3$ and $\gamma = 7.56 \times 10^{-2}\,\text{N/m}$ are the density and surface tension of the supercooled water droplet, respectively, and $h \approx 1\,\text{mm}$ and $R \approx 2\,\text{mm}$ are the average final thickness and radius of the arrested water drop atop the frosted pillars. This results in $t_{\text{spread}} \sim 10\,\text{ms}$, an order of magnitude slower than t_{impale}. Therefore, the preferential wetting of the superhydrophilic ice is unable to account for what is preventing impalement. This is consistent with the experimental observation that droplets do not spread appreciably across the top of the frost-tipped surface prior to getting arrested in the Cassie state.

C.7 Phase map for $t_{\text{wick}} \sim t_{\text{freeze}}$

Comparing the scaling for the wicking time within the frost tips versus the time for the water menisci to freeze between frost tips yields:

$$\frac{\mu h^2}{R_{\text{eff}} \rho U^2 D} \sim \frac{1}{2} \frac{(p - (w_{\text{f}} - w)) \rho_{\text{i}} L \Delta x}{k_{\text{i}} \Delta T}. \tag{C.2}$$

Rearranging terms and introducing the non-dimensional Stefan and Reynolds numbers:

$$\text{Ste} \sim \frac{\mu C_{\text{p}} R_{\text{eff}} \Delta x}{h^2 D} \frac{(p - (w_{\text{f}} - w))}{2 k_{\text{i}}} \text{Re}^2, \tag{C.3}$$

where $\text{Ste} \sim C_{\text{p}} \Delta T / L$ and $\text{Re} \sim \rho U D / \mu$. The figure below plots the corresponding phase map, with Eq. S3 as the phase line.

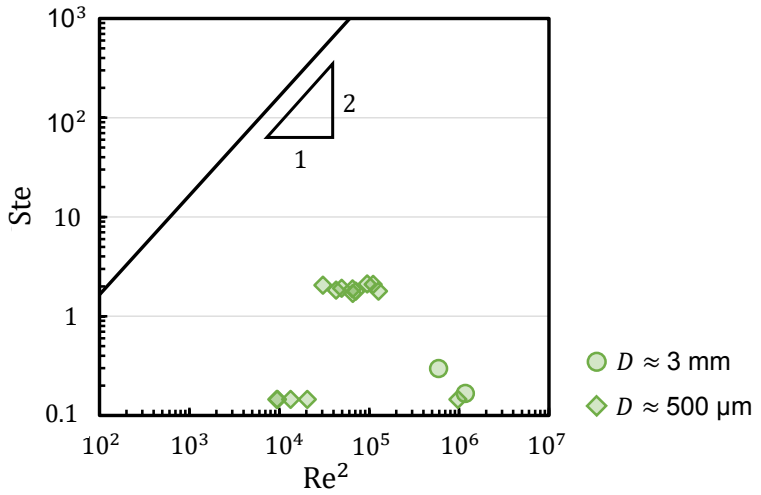

FIGURE C.6: Phase map comparing when t_{wick} is faster (below phase line) versus when t_{freeze} is faster (above phase line). For all experimental conditions tested (green data points), the wicking time scale was faster by orders of magnitude.

C.8 Theoretical time scale comparison

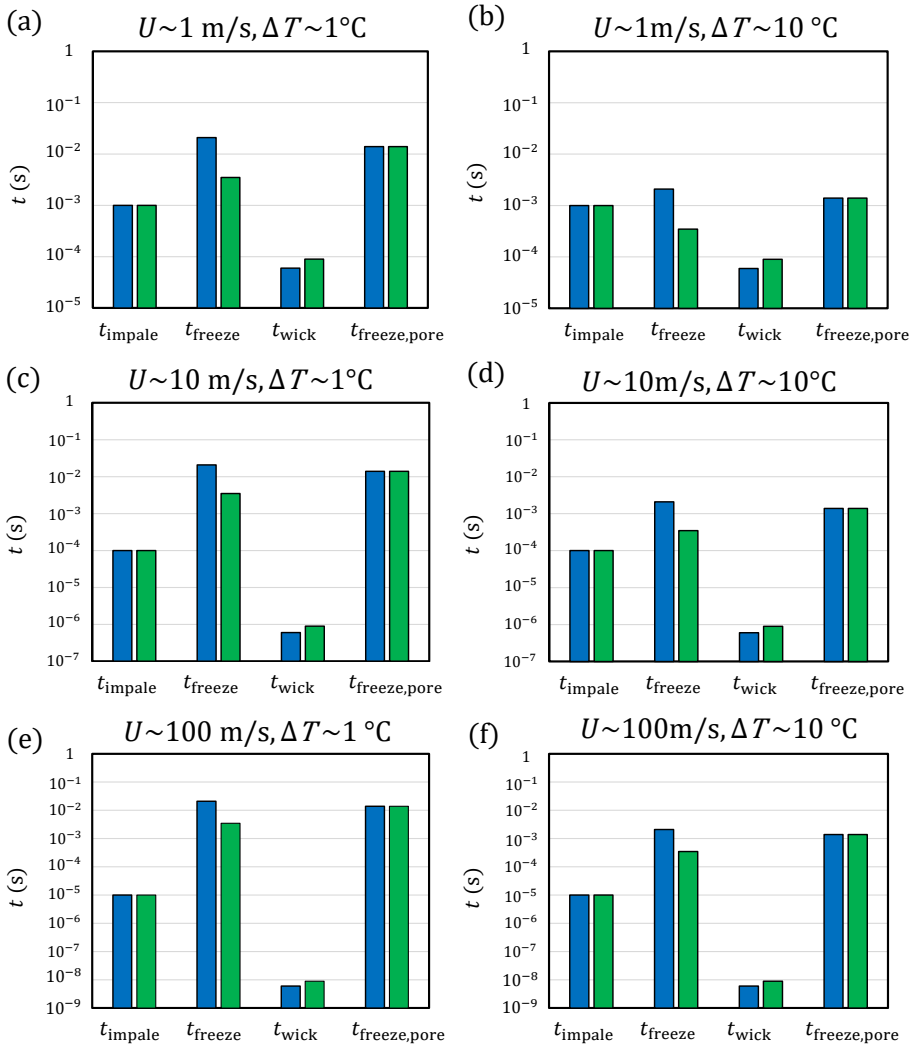

FIGURE C.7: Overview of the calculated time scales for droplet impalement, freezing between frost tips, wicking within frost tips, and freezing within the frost pores. The blue (left) bar is for a droplet size of $D = 0.5$ mm, while the green (right) bar is for $D = 3$ mm. The impact velocity was varied as $U \sim 1$ m/s, 10 m/s, and 100 m/s, to account for anything from a gentle impact to in-flight conditions. The temperature difference between the freeze front and the chilled water/frost varied as $\Delta T = -1\,^{\circ}\mathrm{C}$ or $-10\,^{\circ}\mathrm{C}$. In all cases, the wicking time scale was fastest, indicating that water droplets can wick within the frost tips is a suspended Cassie state prior to impaling or freezing.

Bibliography

[1] D. Richard and D. Quéré. Bouncing water drops. Europhys. Lett., 20:769–775, 2000.

[2] J. B. Boreyko and C. H. Chen. Self-propelled dropwise condensate on superhydrophobic surfaces. Phys. Rev. Lett., 103:184501, 2009.

[3] N. Miljkovic, R. Enright, Y. Nam, K. Lopez, N. Dou, J. Sack, and E. N. Wang. Jumping-droplet-enhanced condensation on scalable superhydrophobic nanostructured surfaces. Nano Lett., 13:179–187, 2012.

[4] E. Dehandschoewercker L. Bourouiba and J. W. M. Bush. Violent expiratory events: on coughing and sneezing. J. Fluid Mech., 853:537–563, 2014.

[5] L. Bourouiba. Turbulent gas clouds and respiratory pathogen emissions: potential implications for reducing transmission of covid-19. Jama, 323:1837–1838, 2020.

[6] T. Gilet and L. Bourouiba. Rain-induced ejection of pathogens from leaves: Revisiting the hypothesis of splash-on-film using high-speed visualization. Integr. Comp. Biol., 54:974–984, 2014.

[7] T. Gilet and L. Bourouiba. Fluid fragmentation shapes rain-induced foliar disease transmission. J. Royal Soc. Interface, 12:20141092, 2015.

[8] Y.S. Joung and C. R. Buie. Aerosol generation by raindrop impact on soil. Nat. Commun., 6:6083, 2014.

[9] K. F. Martin S. Shiri and J. C. Bird. Surface coatings including fingerprint residues can significantly alter the size and shape of bloodstains. Forensic Sci. Int., 295:189–198, 2019.

[10] G. Liang and I. Mudawar. Review of spray cooling – part 1: Single-phase and nucleate boiling regimes, and critical heat flux. Int. J. Heat Mass Transfer, 115:1174–1205, 2017.

[11] G. Liang and I. Mudawar. Review of spray cooling – part 2: High temperature boiling regimes and quenching applications. Int. J. Heat Mass Transfer, 115:1206–1222, 2017.

[12] H. Matsui J. Tsutsumi S. Haas R. Chiba R. Kumai H. Minemawari, T. Yamada and T. Hasegawa. Inkjet printing of single-crystal films. Nature, 475:364–67, 2011.

[13] H.J. Cho, D.J. Preston, Y. Zhu, and E.N. Wang. Nanoengineered materials for liquid-vapour phase-change heat transfer. 2:16092.

[14] C. Maffezzoni. Boiler-turbine dynamics in power-plant control. Control Eng. Pract., 5:301–312, 1997.

[15] R. Mahajan, C. P. Chiu, and G. Chrysler. Cooling a microprocessor chip. P. IEEE, 94:1476–1486, 2006.

[16] E. Pop. Energy dissipation and transport in nanoscale devices. Nano Res., 3:147–169, 2010.

[17] S. M. You, T. W. Simon, and A. Bar-Cohen. A technique for enhancing boiling heat transfer with application to cooling of electronic equipment. IEEE Trans. Compon. Hybrid Manuf. Technol., 15:823–831, 1992.

[18] W. Bobenhausen. Simplified Design of HVAC Systems. John Wiley & Sons, Inc., 1994.

[19] H.M. Ettouney and H.T. El-Dessouky. Fundamentals of salt water desalination. Elsevier, 2002.

[20] S. C. O'Hern B. A. Fellman M. A. Baig S. F. Hassan M. A. Atieh F. Rahman T. Laoui T. Humplik, J. Lee and R. Karnik. Nanostructured materials for water desalination. Nanotechnology, 22:292001, 2011.

[21] O. Vincent, P. Marmottant, P. A. Quinto-Su, and C. D. Ohl. Birth and growth of cavitation bubbles within water under tension confined in a simple synthetic tree. Phys. Rev. Lett., 108:184502, 2012.

[22] D. Quéré. Non-sticking drops. Rep. Prog. Phys., 68:2495–2532, 2005.

[23] M. Reyssat, J. M. Yeomans, and D. Quéré. Impalement of fakir drops. Europhys. Lett., 81:26006, 2008.

[24] D. Quéré. Wetting and roughness. Annu. Rev. Mater. Res., 38:71–99, 2008.

[25] K. E. Witt, S. F. Ahmadi, and J. B. Boreyko. Ice wicking. Phys. Rev. Fluids, 4:024002, 2019.

[26] L. Cao, A. K. Jones, V. K. Sikka, J. Wu, and D. Gao. Anti-icing superhydrophobic coatings. Langmuir, 25:12444–12448, 2009.

[27] S. Farhadi, M. Farzaneh, and S. A. Kulinich. Anti-icing performance of superhydrophobic surfaces. Appl. Surf. Sci., 257:6264–6269, 2011.

[28] P. Tourkine, M. Le Merrer, and D. Quéré. Delayed freezing on water repellent materials. Langmuir, 25:7214–7216, 2009.

[29] T. Maitra, M. K. Tiwari, C. Antonini, P. Schoch, S. Jung, P. Eberle, and D. Poulikakos. On the nanoengineering of superhydrophobic and impalement resistant surface textures below the freezing temperature. Nano Lett., 14:172–182, 2014.

[30] J. B. Boreyko and C. P. Collier. Delayed frost growth on jumping-drop superhydrophobic surfaces. ACS Nano, 7:1618–1627, 2013.

[31] C. L. Gruden, S. M. Dow, and M. T. Hernandez. Fate and toxicity of aircraft deicing fluid additives through anaerobic digestion. Water Environ. Res., 73:72–79, 2001.

[32] R. B. Jackson and E. G. Jobbagy. From icy roads to salty streams. Proc. Natl. Acad. Sci. U.S.A., 102:14487–14488, 2005.

[33] M. G. Medici, A. Mongruel, L. Royon, and D. Beysens. Edge effects on water droplet condensation. Phys. Rev. E, 90:062403, 2014.

[34] J. Guadarrama-Cetina, A. Mongruel, W. Gonzalez-Vinas, and D. Beysens. Frost formation with salt. Europhys. Lett., 110:56002, 2015.

[35] V. G. Damle, X. Sun, and K. Rykaczewski. Can metal matrix-hydrophobic nanoparticle composites enhance water condensation by promoting the dropwise mode? Adv. Mater. Interfaces, 2:1500202, 2015.

[36] X. Sun and K. Rykaczewski. Suppression of frost nucleation achieved using the nanoengineered integral humidity sink effect. ACS Nano, 11:906–917, 2016.

[37] S. Kim, H. Park, H. A. Gruszewski, D. G. Schmale III, and S. Jung. Vortex-induced dispersal of a plant pathogen by raindrop impact. Proc. Natl. Acad. Sci. U.S.A., 116:4917–4922, 2019.

[38] R. N. Strange and P. R. Scott. Plant disease: a threat to global food security. Annu. Rev. Phytopathol., 43:83–116, 2015.

[39] R. F. Park. Stem rust of wheat in australia. Aust. J. Agric. Res., 58:558–566, 2007.

[40] L. Geagea, L. Huber, and I. Sache. Removal of urediniospores of brown (puccinia recondita f.sp. tritici) and yellow (p. striiformis) rusts of wheat from infected leaves submitted to a mechanical stress. Eur. J. Plant Pathol., 103:785–793, 1997.

[41] P.A. Hobson, P.C.H. Miller, P.J. Walklate, C.R. Tuck, and Western N.M. Spray drift from hydraulic spray nozzles: the use of a computer simulation model to examine factors influencing drift. J. Agric. Eng. Res., 54:293–305, 1993.

[42] P. Miller. The measurement of spray drift. Pestic. Outlook., 14:205–209, 2003.

[43] J. M. Cevallos-Cevallos, M. D. Danyluk, G. Gu, G. E. Vallad, and A. H. C. Bruggen. Dispersal of salmonella typhimurium by rain splash onto tomato plants. J. Food Prod., 75:472–479, 2012.

[44] J.M Hirst, O.J. Stedman, and W.H Hogg. Long-distance spore transport: Methods of measurement, vertical spore profiles and the detection of immigrant spores. J. Gen. Microbiol, 48:329–335, 1967.

[45] J. K. M. Brown and M. S. Hovoller. Aerial dispersal of pathogens on the global and continental scales and its impact on plant disease. Science, 297:537–541, 2002.

[46] D. S. Aylor. Spread of plant disease on a continental scale: role of aerial dispersal of pathogens. Ecology, 84:1989–1997, 2003.

[47] E. A. Milus M. S. Hovmoller, A. H. Yahayaoui and A. F. Justtesen. Rapid global spread of two aggressive strains of a wheat rust fungus. Mol. Ecol., 17:3818–3826, 2008.

[48] S. Nagarajan and D. V. Singh. Long-distance dispersion of rust pathogens. Annu. Rev. Phytopathol., 28:139–153, 1990.

[49] J. M. Cevallos-Cevallos, M. D. Danyluk, N. S. Dufault, and A. H. C. Bruggen. Salmonella can reach tomato fruits on plants exposed to aerosols formed by rain. Int. J. Food. Microbiol., 158:140–146, 2012.

[50] J. M. Cevallos-Cevallos, M. D. Danyluk, N. S. Dufault, and A. H. C. Bruggen. High concentrations of biological aerosol particles and ice nuclei during and after rain. Atmos. Chem. Phys., 13:6151–6164, 2013.

[51] D.M. Chate and T.S. Pranesha. Field studies of scavenging of aerosols by rain events. J. Aerosol. Sci., 35:695–706, 2004.

[52] M. Mircea, S. Stefan, and S. Fuzzi. Precipitation scavenging coefficient: Influence of measured aerosol and raindrop size distributions. Atmos. Environ., 34:5169–5174, 2000.

[53] D. G. Schmale III and S. D. Ross. Highways in the sky: scales of atmospheric transport of plant pathogens. Annu. Rev. Phytopathol., 53:591–611, 2015.

[54] C. Josserand and S. T. Thoroddsen. Drop impact on a solid surface. Annu. Rev. Fluid Mech., 48:365–391, 2016.

[55] M. Pasandideh-Fard, Y. M. Qiao, S. Chandra, and J. Mostaghimi. Capillary effects during droplet impact on a solid surface. Phys. Fluids, 8:650–659, 1996.

[56] C. Ingold. La Nova Scientia. A. Forni Editore, Bologna, Italy, 1984.

[57] J. F. Morris T. Leeb I. Bischofberger, B. Ray and S. R. Nagel. Airflows generated by an impacting drop. Soft Matter, 12:3013–3020, 2016.

[58] H. Jo, D. I. Yu, H. Noh, H. S. Park, and M. H. Kim. Boiling on spatially controlled heterogeneous surfaces: wettability patterns on microstructures. Appl. Phys. Lett., 106:181602, 2015.

[59] D. J. Acheson. Elementary fluid dynamics. Oxford Applied Mathematics and Computing Science Series, 1990.

[60] J. K. Batchelor. An introduction to fluid Dynamics. Cambridge Univ Pres, 1967.

[61] P. D. Hildebrand. Dispersal of plant pathogens. Encyclopedia of Pest Management, 2002.

[62] P. H. Gregory. The operation of the puff-ball mechanism of lycoperdon perlatum by raindrops shown by ultra-high-speed schlieren cinematography. Trans. Brit. Mycol. Soc., 32:11–15, 1949.

[63] C. T. Ingold. Fungal spores: their liberation and dispersal. Clarendon Press, Oxford, 1971.

[64] J. M Hirst. Changes in atmospheric spore content: diurnal periodicity and the effects of weather. Trans. Brit. Mycol. Soc., 36:375–393, 1953.

[65] J. Westbrook C. Llorens M. Argentina X. Noblin, N. O. Rojas and J. Dumais. The fern sporangium: a unique catapult. Science, 335:1322, 2012.

[66] D. Poggi and G. G. Katul. Evaluation of the turbulent kinetic energy dissipation rate inside canopies by zero- and level-crossing density methods. Science, 136:219–233, 2010.

[67] F. Veron. Ocean spray. Annu. Rev. Fluid Mech., 47:507–538, 2015.

[68] T. Hussein T. Petaja T. Vesala V. Norros, U. Rannik and O Ovaskainen. Do small spores disperse further than large spores? Ecology, 95:507–538, 2014.

[69] M. Roper, A. Seminara, M. M. Bandi, A. Cobb, H. R. Dillard, and A. Pringle. Dispersal of fungal spores on a cooperatively generated wind. Proc. Natl. Acad. Sci. U.S.A., 107:17474–17479, 2010.

[70] J. D. Jackson. Classical electrodynamics. John Wiley & Sons, New York, 1999.

[71] J. O. Laws and D. A. Parsons. The relation of raindrop-size to intensity. Bot. Rev., 24:452–460, 1943.

[72] S. Gart, J. E. Mates, C. M. Megaridis, and S. Jung. Droplet impacting a cantilever: a leaf-raindrop system. Phys. Rev. Appl., 3:044019, 2015.

[73] L. Geagea, L. Huber, and I. Sache. Dry-dispersal and rain-splash of brown (*Puccinia recondita* f.sp. tritici) and yellow (*P. striiformis*) rust spores from infected wheat leaves exposed to simulated raindrops. Plant Pathol., 48:472–482, 1999.

[74] H. Park, S. Kim, H. A. Gruszewski, D. G. Schmale III, J. B. Boreyko, and S. Jung. Dynamics of splashed droplets impacting wheat leaves treated with a fungicide. J. Royal Soc. Interface, 17:20200337, 2020.

[75] R. Trostle. Global agricultural supply and demand: Factors contributing to the recent increase. Food Commodity Prices Outlook Report WRS-0801, ERS, USDA, Washington DC, USA, 2008.

[76] G. Bai and G. Shaner. Scab of wheat: Prospects for control. Plant Dis., 78:760–766, 1994.

[77] B. Shiferaw, M. Smale, H. J. Braun, E. Duveiller, M. Reynolds, and G. Muricho. Crops that feed the world 10. past successes and future challenges to the role played by wheat in global food security. Food Sec., 5:291–317, 2013.

[78] T. H. Thomas. The global supply and demand for agricultural land in 2050: A perfect storm in the making? Amer. J. Agr. Econ., 93:259–275, 2011.

[79] C.E. Windels. Economic and social impacts of fusarium head blight: changing farms and rural communities in the northern great plains. Phytopathology, 90:17–21, 2000.

[80] Y. Anikster, W. R. Bushnell, and A. P. Roelfs. Puccinia recondita causing leaf rust on cultivated wheats, wild wheats, and rye. Can. J. Botany, 75(12):2082–2096, 1997.

[81] D. E. Aylor. The role of intermittent wind in the dispersal of fungal pathogens. Annu. Rev. Phytopathol., 28:73–92, 1990.

[82] S.A. Isard, S.H. Gage, P. Comtois, and J.M. Russo. Principles of the atmospheric pathway for invasive species applied to soybean rust. BioScience, 55:851–861, 2005.

[83] D.G. Schmale, S.D. Ross, T.L. Fetters, P. Tallapragada, A.K. Wood-Jones, and B. Dingus. Isolates of fusarium graminearum collected 40–320 meters above ground level cause fusarium head blight in wheat and produce trichothecene mycotoxins. Aerobiologia, 28:1–11, 2012.

[84] P. A. Paul, S. M. El-Allaf, P. E. Lipps, and L. V. Madden. Rain splash dispersal of gibberella zeae within wheat canopies in ohio. Phytopathology, 94:1342–1349, 2004.

[85] S. Nath, S. F. Ahmadi, H. A. Gruszewski, S. Budhiraja, C. E. Bisbano, S. Jung, D. G. Schmale III, and J. B. Boreyko. 'sneezing' plants: pathogen transport via jumping-droplet condensation. J. Royal Soc. Interface, 16, 2019.

[86] A. K. Stosch, A. Solga, U. Steiner, E. C. Oerke, W. Barthlott, and Z. Cerman. Efficiency of self-cleaning properties in wheat (*Triticum aestivum* L.). J. appl. Bot. food Qual, 81:49–55, 2007.

[87] D. Richard, C. Clanet, and D. Quéré. Contact time of a bouncing drop. Nature, 417:811, 2002.

[88] C. Ishino, K. Okumura, and D. Quéré. Wetting transitions on rough surfaces. Europhys. Lett., 68:419–425, 2004.

[89] M. Reyssat, A. Pepin, F. Marty, Y. Chen, and D. Quéré. Bouncing transitions on microtextured materials. Europhys. Lett., 74:306–312, 2006.

[90] R. L. Vander Wal, G. M. Berger, and S. D. Mozes. The splash/non-splash boundary upon a dry surface and thin fluid film. Exp. Fluids, 40:53–59, 2006.

[91] A. L. Yarin. Drop impact dynamics: splashing, spreading, receding, bouncing... Annu. Rev. Fluid Mech., 38:159–192, 2006.

[92] D. Bartolo, F. Bouamrirene, E. Verneuil, A. Buguin, P. Silberzan, and S. Moulinet. Bouncing or sticky droplets: impalement transitions on superhydrophobic micropatterned surfaces. Europhys. Lett., 74:299–305, 2006.

[93] Y. C. Jung and B. Bhushan. Dynamic effects of bouncing water droplets on superhydrophobic surfaces. Langmuir, 24:6262–6269, 2008.

[94] J. C. Bird, R. Dhiman, H. M. Kwon, and K. K. Varanasi. Reducing the contact time of a bouncing drop. Nature, 503:385–388, 2013.

[95] Y. Liu, L. Moevius, X. Xu, T. Qian, J. M. Yeomans, and Z. Wang. Pancake bouncing on superhydrophobic surfaces. Nat. Phys., 10:515–519, 2014.

[96] A. Gauthier, S. Symon, C. Clanet, and D. Quéré. Water impacting on superhydrophobic macrotextures. Nat. Commun., 6:8001, 2015.

[97] S. Kim, Z. Wu, E. Esmailia, J. J. Dombroskie, and S. Jung. How a raindrop gets shattered on biological surfaces. Proc. Natl. Acad. Sci. U.S.A., 117:13901–13901, 2020.

[98] C. Antonini, F. Villa, and M. Marengo. Oblique impacts of water drops onto hydrophobic and superhydrophobic surfaces: outcomes, timing, and rebound maps. Exp. Fluids, 55:1713, 2014.

[99] C. Lee, Y. Nam, H. Lastakowski, J. I. Hur, S. Shin, A. L. Biance, C. Pirat, C. J. Kim, and C. Ybert. Two types of Cassie-to-Wenzel wetting transitions on superhydrophobic surfaces during drop impact. Soft Matter, 11:4592–4599, 2015.

[100] H. Kusumaatmaja, M. L. Blow, A. Dupuis, and J. M. Yeomans. The collapse transition on superhydrophobic surfaces. Europhys. Lett., 81:36003, 2008.

[101] C. Lee and C.-J. Kim. Maximizing the giant liquid slip on superhydrophobic microstructures by nanostructuring their sidewalls. Langmuir, 25(21):12812–12818, 2009.

[102] Neelesh A Patankar. Consolidation of hydrophobic transition criteria by using an approximate energy minimization approach. Langmuir, 26(11):8941–8945, 2010.

[103] P. Taylor. The wetting of leaf surfaces. Curr. Opin. Colloid Interface Sci., 16:326–334, 2011.

[104] Y. Bhosale, E. Esmaili, K. Bhar, and S. Jung. Bending, twisting and flapping leaf upon raindrop impact. Bioinspir. Biomim., 15:036007, 2020.

[105] R. L. Hoffman. A study of the advancing interface. i. interface shape in liquid—gas systems. J. Colloid Interface Sci., 50:228–241, 1975.

[106] S. J. Kim, K. Fezzaa, J. An, T. Sun, and S. Jung. Capillary spreading of contact line over a sinking sphere. Appl. Phys. Lett., 111:134102, 2017.

[107] M. Coux, P. Chantelot, L. Domino, C. Clanet, A. Eddi, and D. Quéré. Formation of vase-shaped drops. Phys. Rev. Fluids, 5:033609, 2020.

[108] J. B. Boreyko and C. P. Collier. Dewetting transitions on superhydrophobic surfaces: when are Wenzel drops reversible? J. Phys. Chem. C, 117:18084–18090, 2013.

[109] F. Wang and T. Fang. Retraction dynamics of water droplets after impacting upon solid surfaces from hydrophilic to superhydrophobic. Phys. Rev. Fluids, 5:033604, 2020.

[110] Y. Zhao, Q. Lu, M. Li, and X. Li. Anisotropic wetting characteristics on submicrometer-scale periodic grooved surface. Langmuir, 23:6212–6217, 2007.

[111] A.D. Sommers and A.M. Jacobi. Wetting phenomena on micro-grooved aluminum surfaces and modeling of the critical droplet size. J. Colloid Interface Sci., 328:402–411, 2008.

[112] D. Bartolo, C. Josserand, and D. Bonn. Singular jets and bubbles in drop impact. Phys. Rev. Lett., 96:124501, 2006.

[113] T. Gilet and J. W. M. Bush. Droplets bouncing on a wet, inclined surface. Phys. Fluids, 24:122103, 2012.

[114] C. Antonin, F. Villaand, I. Bernagozzi, A. Amirfazli, and M. Marengo. Drop rebound after impact: The role of the receding contact angle. Langmuir, 29:16045âˆ’16050, 2013.

[115] D. Richard C. Clanet, C. Beguin and D. Quéré. Maximal deformation of an impacting drop. J. Fluid Mech., 517:199–208, 2004.

[116] A. L. Biance, F. Chevy, C. Clanet, G. Lagubeau, and D. Quéré. On the elasticity of an inertial liquid shock. J. Fluid Mech., 554:47–66, 2006.

[117] A. Lafuma and D. Quéré. Superhydrophobic states. Nat. Mater., 2:457–460, 2003.

[118] T. N. Krupenkin, J. A. Taylor, T. M. Schneider, and S. Yang. From rolling ball to complete wetting: the dynamic tuning of liquids on nanostructured surfaces. Langmuir, 20:3824–3827, 2004.

[119] E. Bormashenko, R. Pogreb, G. Whyman, Y. Bormashenko, and M. Erlich. Vibration-induced Cassie-Wenzel wetting transition on rough surfaces. Appl. Phys. Lett., 90:201917, 2007.

[120] A. Gauthier, A. Bouillant, C. Clanet, and D. Quéré. Aerodynamic repellency of impacting liquids. Phys. Rev. Fluids, 3:054002, 2018.

[121] T. Deng, K. K. Varanasi, M. Hsu, N. Bhate, C. Keimel, J. Stein, and M. Blohm. Nonwetting of impinging droplets on textured surfaces. Appl. Phys. Lett., 94:133109, 2009.

[122] H. M. Kwon, A. T. Paxson, K. K. Varanasi, and N. A. Patankar. Rapid deceleration-driven wetting transition during pendant drop deposition on superhydrophobic surfaces. Phys. Rev. Lett., 106:036102, 2011.

[123] S. F. Ahmadi H. Park and J. B. Boreyko. Using frost to promote cassie ice on hydrophilic pillars. Phys. Rev. Lett., 127:044501, 2021.

[124] S. B. Subramanyam, K. Rykaczewski, and K. K. Varanasi. Ice adhesion on lubricant-impregnated textured surfaces. Langmuir, 29:13414–13418, 2013.

[125] P. Kim, T. S. Wong, J. Alvarenga, M. J. Kreder, W. E. Adorno-Martinez, and J. Aizenberg. Liquid-infused nanostructured surfaces with extreme anti-ice and anti-frost performance. ACS Nano, 6:6569–6577, 2012.

[126] K. Golovin, S.P. Kobaku, D. H. Lee, E. T. DiLoreto, J. M. Mabry, and A. Tuteja. Designing durable icephobic surfaces. Sci. Adv., 2:e1501496, 2016.

[127] P. Irajizad, M. Hasnain, N. Farokhnia, S. M. Sajadi, and H. Ghasemi. Magnetic slippery extreme icephobic surfaces. Nat. Commun., 7:13395, 2016.

[128] K. Golovin, A. Dhyani, M. D. Thouless, and A. Tuteja. Low–interfacial toughness materials for effective large-scale deicing. Science, 364:371–375, 2019.

[129] J. Guadarrama-Cetina, A. Mongruel, W. Gonzalez-Vinas, and D. Beysens. Percolation-induced frost formation. Europhys. Lett., 101:16009, 2013.

[130] J. B. Boreyko, B. R. Srijanto, T. D. Nguyen, C. Vega, M. Fuentes-Cabrera, and C. P. Collier. Dynamic defrosting on nanostructured superhydrophobic surfaces. Langmuir, 29:9516–9524, 2013.

[131] S. B. Subramanyam, V. Kondrashov, J. Rühe, and K. K. Varanasi. Low ice adhesion on nano-textured superhydrophobic surfaces under supersaturated conditions. ACS Appl. Mater. Interfaces, 8:12583–12587, 2016.

[132] T. Verho, C. Bower, P. Andrew, S. Franssila, O. Ikkala, and R. H. A. Ras. Mechanically durable superhydrophobic surfaces. Adv. Mater., 23:673–678, 2011.

[133] D. Torresin, M. K. Tiwari, D. D. Col, and D. Poulikakos. Flow condensation on copper-based nanotextured superhydrophobic surfaces. Langmuir, 29:840–848, 2013.

[134] Y. Yao, T. Y. Zhao, C. Machado, E. Feldman, N. A. Patankar, and K. C. Park. Frost-free zone on macrotextured surfaces. Proc. Natl. Acad. Sci. U.S.A., 117:6323–6329, 2020.

[135] K. C. Park, P. Kim, A. Grinthal, N. He, D. Fox, J. C. Weaver, and J. Aizenberg. Condensation on slippery asymmetric bumps. Nature, 531:78–82, 2016.

[136] Y. Zhao, D. J. Preston, Z. Lu, L. Zhang, J. Queeney, and E. N. Wang. Effects of millimetric geometric features on dropwise condensation under different vapor conditions. Int. J. Heat Mass Transfer, 119:931–938, 2018.

[137] S. Nath, C. E. Bisbano, P. Yue, and J. B. Boreyko. Duelling dry zones around hygroscopic droplets. J. Fluid Mech., 853:601–620, 2018.

[138] S. F. Ahmadi, S. Nath, G. J. Iliff, B. R. Srijanto, C. P. Collier, P. Yue, and J. B. Boreyko. Passive anti-frosting surfaces using microscopic ice patterns. ACS Appl. Mater. Interfaces, 10:32874–32884, 2018.

[139] D. M. Murphy and T. Koop. Review of the vapour pressures of ice and supercooled water for atsmopheric applications. Q. J. R. Meteorol. Soc., 131:1539–1565, 2005.

[140] D. Soto, H.-L. Girard, A. Le Helloco, T. Binder, D. Quéré, and K. K. Varanasi. Droplet fragmentation using a mesh. Phys. Rev. Fluids, 3:083602, 2018.

[141] A. Nasto, P. T. Brun, , and A. E. Hosoi. Drop impact on hairy surfaces. Phys. Rev. Fluids, 4:064004, 2019.

[142] R. de Ruiter, P. Colinet, P. Brunet, J. H. Snoeijer, and H. Gelderblom. Contact line arrest in solidying spreading drops. Phys. Rev. Fluids, 2:043602, 2017.

[143] Z. Jin, H. Zhang, and Z. Yang. Experimental investigation of the impact and freezing processes of a water droplet on an ice surface. Int. J. Heat Mass Transfer, 109:716–724, 2017.

[144] M. Schremb, I. V. Roisman, and C. Tropea. Normal impact of supercooled water drops onto a smooth ice surface: experiments and modelling. J. Fluid Mech., 835:1087–1107, 2018.

[145] V. Thiévenaz, C. Josserand, and T. Séon. Retraction and freezing of a water film on ice. Phys. Rev. Fluids, 5:041601, 2020.

[146] K. Rykaczewski, S. Anand, S. B. Subramanyam, and K. K. Varanasi. Mechanism of frost formation on lubricant-impregnated surfaces. Langmuir, 29:5230–5238, 2013.

[147] F. Chu, D. Wen, and X. Wu. Frost self-removal mechanism during defrosting on vertical superhydrophobic surfaces: Peeling off or jumping off. Langmuir, 34:14562–14569, 2018.

[148] R. Chen, M. C. Lu, V. Srinivasan, Z. Wang, H. H. Cho, and A. Majumdar. Nanowires for enhanced boiling heat transfer. Nano Lett., 9:548–553, 2009.

[149] K. H. Chu, R. Enright, and E. N. Wang. Structured surfaces for enhanced pool boiling heat transfer. Appl. Phys. Lett., 100:241603, 2012.

[150] H. Qiu A. R.l Betz, J. Xu and D. Attinger. Do surfaces with mixed hydrophilic and hydrophobic areas enhance pool boiling? Appl. Phys. Lett., 97:141909, 2010.

[151] M. M. Rahman, J. Pollack, and M. McCarthy. Increasing boiling heat transfer using low conductivity materials. Sci. Rep., 5:13145, 2015.

[152] M. M. Rahman, E. Olceroglu, and M. McCarthy. Role of wickability on the critical heat flux of structured superhydrophilic surfaces. Langmuir, 30:11225–11234, 2014.

[153] N. S. Dhillon, J. Buongiorno, and K. K. Varanasi. Critical heat flux maxima during boiling crisis on textured surfaces. Nat. Commun., 6:8247, 2015.

[154] S. Hao K. Montazeri C.-H Lin J lee M. Ali Q. N. Pham, S. Zhang and Y. Won. Boiling heat transfer with a well-ordered microporous architecture. ACS Appl. Mater. Interfaces, 12:19174–19183, 2020.

[155] J. Li, W. Fu, B. Zhang, G. Zhu, and N. Miljkovic. Ultrascalable three-tier hierarchical nanoengineered surfaces for optimized boiling. ACS Nano, 13:14080–14093, 2019.

[156] Z. Lu P. Cheng L. Zhang, S. Gong and E. N.Wang. A unified relationship between bubble departure frequency and diameter during saturated nucleate pool boiling. Int. J. Heat Mass Transfer, 165:120640, 2022.

[157] Z. Lu P. Cheng L. Zhang, S. Gong and E. N.Wang. Boiling crisis due to bubble interactions. Int. J. Heat Mass Transfer, 182:121904, 2022.

[158] J. B. Boreyko and C. H. Chen. Self-propelled jumping drops on superhydrophobic surfaces. Phys. Fluids, 22:091110, 2010.

[159] F. Liu, G. Ghigliotti, J. J. Feng, and C. H. Chen. Numerical simulations of self-propelled jumping upon drop coalescence on non-wetting surfaces. J. Fluid Mech., 752:39–65, 2014.

[160] R. Enright, N. Miljkovic, J. Sprittles, K. Nolan, R. Mitchell, and E. N. Wang. How coalescing droplets jump. ACS Nano, 8:10352–10362, 2014.

[161] R. Enright, N. Miljkovic, A. Al-Obeidi, C. V. Thompson, and E. N. Wang. Condensation on superhydrophobic surfaces: the role of local energy barriers and structure length scale. Langmuir, 28:14424–14432, 2012.

[162] K. Rykaczewski. Microdroplet growth mechanism during water condensation on superhydrophobic surfaces. Langmuir, 28:7720–7729, 2012.

[163] T. Mouterde, Gaélle Lehoucq, Stéphane Xavier, A. Checco, C. T. Black, A. Rahman, T. Midavaine, C. Clanet, and D. Quéré. Antifogging abilities of model nanotextures. Nat. Mater., 16:658–663, 2017.

[164] M. D. Mulroe, B. R. Srijanto, S. F. Ahmadi, C. P. Collier, and J. B. Boreyko. Tuning superhydrophobic nanostructures to enhance jumping-droplet condensation. ACS Nano, 1:8499—8510, 2017.

[165] A Fraters D Van Der Meer ÁM Soto, T Maddalena and D Lohse. Coalescence of diffusively growing gas bubbles. J. Fluid Mech., 846:143–165, 2018.

[166] P. Lu, P. Peñas, H. L. The, J. Eijkel, A. V. D. Berg, X. Zhang, and D. Lohse. Self-propelled detachment upon coalescence of surface bubbles. Phys. Rev. Lett., 127:235501, 2021.

[167] Y. Zhang J. Wei Y. Yang J. Zhou, B. Qi and Q Cao. Experimental and theoretical study of bubble coalescence and departure behaviors during nucleate pool boiling on uniform smooth and micro-pinfinned surfaces under different subcoolings and heat fluxes. Exp. Therm. Fluid Sci., 112:109996, 2020.